Titre: Title:	Mechanical and optical properties of plasma deposited superhard nanocomposite coatings
Auteur: Author:	Pawel Michal Jedrzejowski
Date:	2004
Type:	Mémoire ou thèse / Dissertation or Thesis
Référence: Citation:	Jedrzejowski, P. M. (2004). Mechanical and optical properties of plasma deposited superhard nanocomposite coatings [Thèse de doctorat, École Polytechnique de Montréal]. PolyPublie. https://publications.polymtl.ca/7260/

UNIVERSITÉ DE MONTRÉAL

MECHANICAL AND OPTICAL PROPERTIES OF PLASMA DEPOSITED SUPERHARD NANOCOMPOSITE COATINGS

PAWEL MICHAL JEDRZEJOWSKI
DÉPARTEMENT DE GÉNIE PHYSIQUE
ÉCOLE POLYTECHNIQUE DE MONTRÉAL

THÈSE PRÉSENTÉE EN VUE DE L'OBTENTION
DU DIPLÔME DE PHILOSOPHIÆ DOCTOR
(GÉNIE PHYSIQUE)
FÉVRIER 2004

Your file Votre référence
ISBN: 0-612-89228-X
Our file Notre référence
ISBN: 0-612-89228-X

UNIVERSITÉ DE MONTRÉAL

ÉCOLE POLYTECHNIQUE DE MONTRÉAL

Cette thèse intitulée :

MECHANICAL AND OPTICAL PROPERTIES OF PLASMA DEPOSITED SUPERHARD NANOCOMPOSITE COATINGS

Présentée par : JEDRZEJOWSKI Pawel Michal

En vue de l'obtention du diplôme de : Philosophiæ Doctor

A été dûment acceptée par le jury d'examen constitué de :

M. DESJARDINS Patrick, Ph. D., président

Mme. SAPIEHA Jolanta Ewa, Ph. D., membre et directeur de recherche

M. MARTINU Ludvik, Ph. D., membre et codirecteur de recherche

M. MITURA Stanislaw, Ph. D., membre et codirecteur de recherche

M. STANSFIELD Barry, Ph.D., membre

M. BALAZINSKI Marek, Ph. D., membre

Acknowledgements

I wish to thank my thesis supervisors Dr. Jolanta Sapieha and Professor Ludvik Martinu for giving me the opportunity to work on an exiting research project, for their guidance, support and patience throughout my studies.

I would like to thank my co-director, Professor Stanislaw Mitura of the Technical University of Lodz, Poland for his support during my earlier studies in Lodz, and for helping to establish collaboration with the École Polytechnique de Montréal.

I would furthermore like to thank Professor Patrick Desjardins, Professor Barry Stansfield, Professor Marek Balazinski, and Professor François Trochu for accepting to evaluate my Ph. D. thesis.

I sincerely thank the co-authors of my papers and everyone else who have contributed to the advancement of my project, in particular Jiri Cizek and Professor Jaroslav Vlcek (University of West Bohemia, Plzen, Czech Republic).

I also wish to thank my friends and colleagues in the Department of Engineering Physics, École Polytechnique, particularly Mr. Gilles Jalbert, without whom this work would not be possible, Mr. Jiri Cerny and Mr. Francis Turcot for their continuing help, Dr. Oleg Zabeida and Dr. Jorg Oberste-Berghaus for many valuable discussions, and all the students: Aram Amassian, Bill Baloukas, Gilles Dennler, Marie-Maude de Denus-Baillargeon, Mariusz Dudek, Jean-Michel Lamarre, Stéphane Larouche, Jean-Philippe Masse, Luiz Melo, Ani Sobral-Torres, and Richard Vernhes for their help and friendly environment.

Résumé

Les couches minces nanocomposites (nc) sont d'un intérêt considérable à cause de leur grande dureté et de leurs propriétés tribologiques, optiques et d'autres propriétés fonctionnelles intéressantes. Dans ce type de structures, des particules cristallines de l'ordre du nanomètre sont incorporées dans une matrice amorphe ou polycristalline. Le comportement tribo-mécanique particulier des matériaux nc est dû au nombre très élevé d'interfaces internes empêchant la propagation de fissures.

Au cours des travaux de recherche, nous avons étudié les couches ultradures de nc-$TiN/SiN_{1.3}$ et de nc-TiC_xN_y/SiCN. Ces matériaux ont été fabriqués par dépôt chimique en phase vapeur assistée par plasma (PECVD) dans une décharge radiofrequencielle. La croissance a été assistée par bombardement ionique. Ces couches ont été déposées à partir d'un mélange de gaz $TiCl_4/SiH_4/CH_4/N_2$. La pression totale pendant le dépôt était maintenue à 200 mTorr (26.66 Pa) et la température du substrat variait de 300 °C à 500 °C.

Afin de caractériser la composition chimique et la structure complexe des matériaux nc, une approche multitechnique a été adoptée. Cette approche a permis de cerner la relation entre la structure et les propriétés des ces matériaux. La composition chimique a été examinée par spectroscopie de photoélectrons par rayons X, par électrons Auger, spectroscopie Raman, microscopie électronique à balayage, en transmission et microscopie à force atomique. Nous avons aussi bénéficié de l'ellipsométrie spectroscopique et de la détection par recul élastique en régime de temps de vol. Les propriétés mécaniques ont été évaluées par indentation dynamique (nanoindentation), statique et mesures tribologiques. Les constantes optiques ont été déterminées par spectrophotométrie et ellipsométrie spectroscopique.

Une introduction à la résistance mécanique des matériaux est suivie des résultats principaux présentés sous forme de quatre articles. Le premier article de ce travail concerne le system de nc-TiN/$SiN_{1.3}$. Les propriétés mécaniques et la microstructure du matériau fabriqué à basse température de 300 °C ont été systématiquement comparées avec celles du matériau fabriqué à haute température (500 °C). Une attention particulière a été portée à la méthodologie des mesures mécaniques, particulièrement à la dureté.

Les valeurs de la dureté obtenues par les mesures dynamiques ont été comparées avec celles obtenues par des méthodes statiques. Dans le cas des méthodes statiques, plusieurs modèles mathématiques différents ont été utilisés afin d'éliminer l'influence du substrat et estimer l'effet de la taille d'indentation, notamment les modèles de Jonsson et Hogmark, de Burnett et Rickerby, de Chicot et Lesage, de Korsunsky et al. et de Ichimura et al. Dans ces modèles, l'approche commune est basée sur l'évaluation de la dureté des couches en fonction de la dureté composite du système couche-substrat. L'influence du substrat sur la valeur de la dureté composite est calculée par des approches qui tiennent compte des propriétés élasto-plastiques de la couche et du substrat, de l'épaisseur de la couche, de la charge appliquée, et de la géométrie d'indentation. Nous avons démontré que sous les conditions de calibration appropriées, tous les modèles donnent des résultats similaires, tout à fait comparables à ceux obtenus par les mesures dynamiques.

Ayant élaboré la méthodologie des mesures mécaniques, les matériaux nc-TiN/$SiN_{1.3}$ ont été optimisés par rapport à la dureté et au module d'Young. En ajustant la quantité de $SiN_{1.3}$ dans les couches, des conditions optimales de dépôt ont été établies. Les couches sont caractérisées par des valeurs de dureté et de module d'Young réduit élevés (jusqu'à 45 et 350 GPa, respectivement). Les contraintes mécaniques des couches nc-TiN/$SiN_{1.3}$ sont relativement faibles, entre 1,0 et 2,5 GPa en compression. Le rebondissement élastique est élevé, jusqu'à 69 %, et la valeur de la ténacité est entre 1,0 et 1,8 MPa $m^{0.5}$. Le coefficient de frottement et le taux d'usure, mesurés contre le diamant, sont d'environ

0,11 et $12*10^{-6}$ mm^3/Nm respectivement. Ce comportement a été expliqué par le modèle structural qui suppose l'inclusion de nanocristaux de TiN dans une matrice amorphe de $SiN_{1.3}$: l'augmentation de la quantité de la phase amorphe augmente la distance entre les nanocristaux tandis que leur taille, 8 nm environ, reste approximativement constante. Ce modèle a été confirmé par l'analyse structurale.

Le comportement optique de ces matériaux a été décrit par le modèle des électrons libres de Drude et celui des absorptions électroniques de Lorentz. L'augmentation de la quantité de $SiN_{1.3}$, a pour effet la diminution de l'absorption dans l'infrarouge et l'augmentation de la résistivité des couches. pour une variation de la concentration du Si de 0 à 50 % atomique. Les couleurs ont aussi changé, marquant la transition d'un caractère métallique à diélectrique.

Dans la deuxième partie de ce travail, nous avons étudié des revêtements de SiCN. Ce matériau constitue, dans les expériences subséquentes, la matrice amorphe dans la structure nanocomposite. Pour une quantité optimale d'environ 28 % atomique de C, une dureté de 33 GPa, un module d'Young réduit de 200 GPa et un rebondissement élastique de 85 % ont été obtenus. Cette dureté élevée par rapport à celle de $SiN_{1.3}$ (18 GPa) et de SiC (26 GPa) a été attribuée à la formation de liaisons du type C-N. Le matériau nouveau SiCN a été incorporé dans le système quaternaire de nc-TiC_xN_y/SiCN.

La partie finale de ce travaille porte sur des revêtements de nc-TiC_xN_y/SiCN. Pour une concentration optimale de C (environ 10 % at.), les couches de nc-TiC_xN_y/SiCN possèdent une valeur de dureté très élevée d'environ 55 GPa. Ce type de matériaux est caractérisé aussi par des propriétés élastiques élevées exprimées par le module d'Young réduit de 306 GPa et le rebondissement élastique de plus que 80 %. La résistance contre la déformation plastique, exprimée par le rapport H^3/E_r^2 était de 1,8 GPa. C'est la valeur la plus élevée par rapport aux valeurs montrées par d'autres auteurs. Les contraintes mécaniques varient entre 2,0 et 2,5 GPa en compression. Le coefficient de frottement et

le taux d'usure mesuré contre le diamant sont d'environ 0,13 et $12*10^{-6}$ mm^3 / Nm, respectivement. Cette performance mécanique est attribuée à l'effet combiné de la structure nc avec la matrice de SiCN optimisée et des liaisons chimiques fortes Ti-C dans les nanocristaux.

Abstract

Nanocomposite (nc) thin films attract considerable attention due to a possibility to obtain very high hardness, enhanced tribological performance, interesting colors and other functional properties. The nc films are formed by nanometer-size particles embedded in an amorphous or polycrystalline matrix. Their remarkable tribo-mechanical characteristics are related to the introduction of inner surfaces that hamper crack propagation.

In this work, we investigate the growth and the characteristics of nc-TiN/$SiN_{1.3}$ and nc-TiC_xN_y/SiCN superhard coatings. These materials were fabricated by plasma enhanced chemical vapor deposition (PECVD) in a radio frequency discharge using intense ion bombardment. The coatings were deposited from $TiCl_4/SiH_4/CH_4/N_2$ gas mixtures at a pressure of 200 mTorr (26.66 Pa) and with substrate temperatures ranging from 300 to 500 ^{o}C. We systematically evaluate the films' mechanical and optical properties, and we interpret them in terms of their microstructure.

In order to establish the structure-property relationship and to optimize the nc material, a multitechnique characterization approach was applied. This includes X-ray photoelectron, Auger electron and Raman spectroscopies, and scanning electron, transmission electron and atomic force microscopies. We also benefited from our expertise in spectroscopic ellipsometry and elastic recoil detection. Mechanical properties were characterized by depth sensing and static indentations, and tribological measurements. Optical constants and colors were assessed by spectrophotometry and spectroscopic ellipsometry.

After an introduction to the mechanical strength of materials, the results are presented in the form of four articles. The first part of the work describes the nc-TiN/$SiN_{1.3}$ system. The mechanical properties and microstructure of coatings deposited at a low temperature

of 300 °C are systematically compared with those deposited at 500 °C. Special attention was paid to the methodology of mechanical measurements, in particular hardness.

The values of hardness obtained from depth sensing indentations were compared to those obtained from static indentations. In the latter measurements, we applied different mathematical models that have originally been proposed to eliminate the influence of the substrate and to evaluate the indentation size effect; this includes the models of Jonsson and Hogmark, Burnett and Rickerby, Chicot and Lesage, Korsunsky et al., and Ichimura et. al. We show that all these models have a common background in which the coating's hardness is obtained from the measured composite hardness of the coating-substrate system. The influence of the substrate is then estimated by taking into account elasto-plastic properties of the coating and of the substrate, coating thickness, load applied to the indenter and the geometry of the indentation. We have shown that if appropriate calibration is performed, all these models yield similar results, fully comparable with those obtained by depth-sensing indentation.

After establishing the methodology of mechanical measurements, we optimized the nc-TiN/$SiN_{1.3}$ from the point of view of hardness and Young's modulus. By changing the amount of $SiN_{1.3}$ we identified optimum deposition conditions resulting in the highest hardness and reduced Young's modulus, up to 45 and 350 GPa, respectively. This was accompanied by low compressive stress, that varied between 1.0 and 2.5 GPa, an elastic rebound up to 69 %, low friction coefficient of 0.11 measured against diamond, a toughness that varied from 1.0 to 1.8 MPa $m^{0.5}$, and a wear rate of about $12*10^{-6}$ mm^3/Nm (against diamond). This behavior was explained by the structural model that assumes TiN nanocrystals embedded in the amorphous matrix of $SiN_{1.3}$. Increasing the amount of $SiN_{1.3}$ increases the distance between the nanocrystals while their size remains approximately constant, about 8 nm. This model was supported by the structural analysis.

Optical properties of nc-TiN/$SiN_{1.3}$ were also studied. The optical response was modeled by the free electron Drude approach combined with Lorentz interband absorptions. We found that increasing the amount of $SiN_{1.3}$ decreased the absorption in the infrared region and increased the resistivity of the coatings. The colors also changed, loosing their characteristic metallic lustre, and marking a transition from metallic to dielectric behavior.

In the second part of this work, we studied the properties of SiCN films, which were then used as a matrix in the nanocomposite. By adding an optimized amount of carbon to $SiN_{1.3}$ (~ 28 at. %), a hardness of 33 GPa, a reduced Young's modulus of 200 GPa and an elastic rebound of 85 % were obtained. Such high hardness compared to 18 GPa for $SiN_{1.3}$ and 26 GPa for SiC, is attributed to the formation of C-N bonds. The new SiCN material was incorporated in the novel, quaternary nc-TiC_xN_y/SiCN system.

The final part of this work describes quaternary nc-TiC_xN_y/SiCN coatings. At an optimum C concentration (~ 10 at. %), the nc structure is preserved and it is characterized by very high hardness (55 GPa), high reduced Young's modulus (306 GPa), and an elastic rebound of more than 80 %. High resistance to plastic deformation, expressed by a high H^3/E_r^2 ratio of up to 1.8 GPa was obtained; this is higher than reported by any other group. The mechanical stress was between 2.0 and 2.5 GPa in compression. The friction coefficient and the wear rate, measured against diamond, were found to be 0.13 and $12*10^{-6}$ mm^3/Nm, respectively. Such superior mechanical performance is attributed to a combined effect of nc structure together with enhanced properties of the SiCN matrix and strong Ti-C bonds in the nanocrystals.

Condensé en français

Les couches minces nanocomposites (nc) sont d'un intérêt considérable à cause de leur grande dureté et de leurs propriétés tribologiques, optiques et d'autres propriétés fonctionnelles intéressantes. Dans ce type de structures, des particules cristallines de l'ordre du nanomètre sont incorporées dans une matrice amorphe ou polycristalline. Le comportement tribo-mécanique particulier des matériaux nc est dû au nombre très élevé d'interfaces internes (entre les nanoparticules et la matrice) empêchant la croissance et la propagation de fissures.

Au cours de mes travaux de recherche, j'ai étudié les couches ultradures de nc-TiN/$SiN_{1.3}$ et de nc-TiC_xN_y/SiCN. Ces matériaux ont été fabriqués par dépôt chimique en phase vapeur assistée par plasma (plasma enhanced chemical vapor deposition, PECVD) excité par radiofréquence. La croissance a été assistée par bombardement ionique contrôlé par le potentiel d'autopolarisation DC du porte-substrat. Ces couches ont été déposées à partir d'un mélange de gaz $TiCl_4/SiH_4/CH_4/N_2$. Les mélanges utilisés étaient constitués d'une quantité fixe de $TiCl_4/N_2$, tandis que des quantités variables de SiH_4 et CH_4 ont été ajustées. La pression totale pendant le dépôt était maintenue à 200 mTorr (26.66 Pa) et la température du substrat variait de 300 °C à 500 °C. La majorité des couches ont été déposées sur des substrats de silicium cristallin.

Afin de caractériser la composition chimique et la structure complexe des matériaux nc, une approche multitechnique a été adoptée. Cette approche a permis de cerner la relation entre la structure et les propriétés des ces matériaux. La composition chimique a été examinée par spectroscopie de photoélectrons par rayons X (X-ray photoelectron spectroscopy, XPS), détection du recul élastique en régime de temps de vol (elastic recoil detection in time of flight regime, ERD-TOF), spectroscopie des électrons Auger (Auger electron spectroscopy, AES), spectroscopie Raman et ellipsométrie spectroscopique aux angles variables dans l'infrarouge (infrared variable angle spectroscopic ellipsometry, IR

VASE). La structure des couches a été déterminée par microscopie électronique à balayage (scanning electron microscopy, SEM) et en transmission (transmission electron microscopy, TEM), par microscopie à force atomique (atomic force microscopy, AFM) et par diffraction des rayons X (X-ray diffraction, XRD).

De nombreux tests ont été effectués afin de rendre compte du comportement mécanique. Les propriétés mécaniques comme la dureté, le module d'Young réduit et la ténacité ont été évaluées par indentation dynamique (nanoindentation) et statique. Les contraintes mécaniques ont été mesurées par la méthode de courbure des substrats. Les propriétés tribologiques comme le coefficient de frottement et le taux d'usure ont été évaluées par le test de rayure et Triboindenteur. Les propriétés optiques et la couleur ont quant à elles été étudiées par VASE et par spectrophotométrie. Toutes ces analyses ont confirmé une structure de type nc des échantillons. Les couches de nc-TiN/$SiN_{1.3}$ et nc-TiC_xN_y/SiCN dont les propriétés mécaniques ont été optimisées du point de vue de la dureté et du module d'Young, possédaient des nanoparticules cristallines de TiN et TiCN dans des matrices amorphes de $SiN_{1.3}$ et SiCN, respectivement. Dans les deux matériaux, la taille moyenne des particules a été estimée à environ 8 nm.

Cette thèse commence par une introduction à la résistance mécanique des matériaux et la description des materiaux nc. Elle est suivie des résultats principaux présentés sous forme de quatre articles. Le premier article de ce travail concerne le développement du processus de fabrication à basse température (300 °C) des couches nc-TiN/$SiN_{1.3}$ et leur optimisation du point de vue de la dureté et du module d'Young. Ces propriétés ont été comparées avec celles du matériau fabriqué à haute température (500 °C). La composition chimique a d'abord été déterminée par XPS et AES, puis confirmée par ERD-TOF. Pour le nc-TiN/$SiN_{1.3}$ qui possédait la dureté la plus élevée, ces analyses ont indiqué la présence de TiN stœchiométrique avec 5 à 10 % atomique de Si. Dans le matériau similaire fabriqué à basse température (300 °C), le TiN se montrait sous-

stœchiométrique par rapport à N. Ces phénomènes sont expliqués par la basse température de dépôt qui n'a pas favorisé les réactions chimiques entre Ti, Si et N.

À cause de leur dureté et élasticité très élevées, les couches ultradures nécessitent une approche systématique afin d'évaluer correctement leurs propriétés mécaniques. Une méthodologie de mesures, particulièrement de la dureté, a été établie. Les valeurs de la dureté obtenues par les mesures dynamiques ont été comparées avec celles obtenues par des méthodes statiques. Dans le cas des méthodes statiques, plusieurs modèles mathématiques différents ont été utilisés afin d'éliminer l'influence du substrat et estimer l'effet de la taille d'indentation, notamment les modèles de Jonsson et Hogmark, de Burnett et Rickerby, de Chicot et Lesage, de Korsunsky et al. et de Ichimura et al. Dans ces modèles, l'approche commune est basée sur l'évaluation de la dureté des couches en fonction de la dureté composite du système couche-substrat. L'influence du substrat sur la valeur de la dureté composite est calculée par des approches qui tiennent compte des propriétés élasto-plastiques de la couche et du substrat, de l'épaisseur de la couche, de la charge appliquée, et de la géométrie d'indentation. Nous avons démontré que sous les conditions de calibration appropriées, tous les modèles donnent des résultats similaires, tout à fait comparables à ceux obtenus par les mesures dynamiques.

Ayant élaboré la méthodologie des mesures mécaniques, les matériaux nc-TiN/$SiN_{1.3}$ ont été optimisés par rapport à la dureté et au module d'Young réduit. En ajustant la quantité de la phase amorphe dans les couches, des conditions optimales de dépôt ont été établies. Les couches sont caractérisées par des valeurs de dureté et de module d'Young réduit élevées (jusqu'à 45 et 350 GPa, respectivement). Les contraintes mécaniques des couches nc-TiN/$SiN_{1.3}$ sont relativement faibles, entre 1,0 et 2,5 GPa en compression. Le rebondissement élastique est élevé, jusqu'à 69 %, et la valeur de la ténacité est entre 1,0 et 1,8 MPa $m^{0.5}$. Le coefficient de frottement et le taux d'usure, mesurés contre le diamant, sont d'environ 0,11 et $12*10^{-6}$ mm^3/Nm respectivement. Ce comportement a été expliqué par le modèle structural qui suppose l'inclusion de nanocristaux de TiN dans

une matrice amorphe de $SiN_{1.3}$: l'augmentation de la quantité de la phase amorphe augmente la distance entre les nanocristaux tandis que leur taille, 8 nm environ, reste approximativement constante.

La partie suivante de ce travail concerne les propriétés optiques des couches nc-$TiN/SiN_{1.3}$ fabriquées à basse et haute températures. Le comportement optique de ces matériaux a été décrit par le modèle des électrons libres de Drude et celui des absorptions électroniques de Lorentz. Les couches de nc-$TiN/SiN_{1.3}$ contenant une concentration optimale de Si présentent des propriétés métalliques, avec un indice de réfraction relativement bas (environ 1,2) et un coefficient d'extinction élevé (environ 2,2) pour une énergie de photon incident de 2,24 eV (550 nm). L'augmentation de la proportion de la phase amorphe, révélée par la concentration de Si, a pour effet d'augmenter l'indice de réfraction et de diminuer le coefficient d'extinction, pour une variation de la concentration du Si de 0 à 50 % atomique. Cette transformation des propriétés optiques est symptomatique du changement de comportement d'un métal à un diélectrique et a été accompagnée par un changement de couleur de l'or métallique au gris mat.

La transition d'un caractère métallique à diélectrique de nc-$TiN/SiN_{1.3}$ a également été accompagnée par l'augmentation de la résistivité des couches. La résistivité mesurée directement par la sonde à quatre pointes et, indirectement, par ellipsométrie augmente d'environ 75 $\mu\Omega$cm à $7*10^4$ $\mu\Omega$cm avec l'augmentation de la quantité de la phase diélectrique. Ce comportement confirme le modèle phénoménologique du matériau nc.

Dans la deuxième partie de ce travail, une attention particulière a été apportée aux revêtements de SiCN. Ce matériau constitue, dans les expériences subséquentes, la matrice amorphe dans la structure nc-TiC_xN_y/SiCN. L'influence du carbone sur les propriétés mécaniques et optiques de la matrice a été évaluée. Pour une quantité d'environ 28 % atomique de C, la formation de forts liens chimiques C-N a été observée par IR VASE et confirmée par les analyses quantitatives par XPS. Ce type de liens forts a

amélioré la performance mécanique et tribologique du SiCN par rapport au $SiN_{1.3}$ pur. La dureté, le module d'Young réduit et le rebondissement élastique ont augmenté de 18 à 33 GPa, de 120 à 200 GPa et de 80 à 85 %, respectivement. L'incorporation du carbone dans la structure de $SiN_{1.3}$ a diminué le coefficient de frottement mesuré contre le Al_2O_3 d'environ 0,75 pour $SiN_{1.3}$ pur à 0,45 pour le SiCN caractérisé par la dureté et le module d'Young réduit les plus élevés.

Après avoir optimisé les propriétés mécaniques de la matrice amorphe du SiCN, des couches quaternaires nc-TiC_xN_y/SiCN étaient fabriquées tel que décrit plus bas. Le système nc-TiC_xN_y/SiCN est caractérisé par une dureté plus élevée que celle de nc-TiN/$SiN_{1.3}$. Ce comportement est attribué à l'effet combiné de la structure nc avec la matrice de SiCN optimisée et des liaisons chimiques fortes Ti-C dans les nanocristaux. Pour une concentration optimale de C (environ 10 % at.), les couches de nc-TiC_xN_y/SiCN possèdent une valeur de dureté très élevée d'environ 55 GPa. Ce type de matériaux est caractérisé aussi par des propriétés élastiques élevées exprimées par le module d'Young réduit de 306 GPa et le rebondissement élastique de plus que 80 %.

Les couches nc-TiC_xN_y/SiCN possèdent d'autres caractéristiques mécaniques et tribologiques intéressantes. Dû à la grande valeur de la dureté, la résistance contre la déformation plastique, exprimée par le rapport H^3/E_r^2 a augmenté d'environ 0,8 GPa pour nc-TiN/$SiN_{1.3}$ jusqu'à 1,8 GPa pour le nc-TiC_xN_y/SiCN. C'est la valeur la plus élevée par rapport aux valeurs montrées par d'autres auteurs. En comparaison, le rapport H^3/E_r^2 du diamant est d'environ 0,9 GPa. Les contraintes mécaniques qui pourraient influencer les caractéristiques tribo-mécaniques sont faibles et varient entre 2,0 et 2,5 GPa en compression. Les matériaux nc font preuve d'une ténacité d'environ 1 MPa $m^{0.5}$. Le coefficient de frottement, mesuré contre le diamant, est bas, environ 0,13, et le taux d'usure mesuré avec la pointe de diamant est d'environ $12*10^{-6}$ mm^3 / Nm.

La bonne performance mécanique des couches nc-TiC_xN_y/SiCN s'accompagne par de propriétés optiques et couleurs intéressantes du point de vue des applications décoratives. Avec l'incorporation successive du carbone, les propriétés optiques du nc-TiC_xN_y/SiCN changent d'un comportement métallique à un comportement diélectrique. L'indice de réfraction augmente d'environ 1,2 à 2,0, et le coefficient d'extinction diminue de 1,73 à 1,20 pour une énergie de photon incident de 2,24 eV (550 nm). Le changement de couleur est expliqué par la transformation de structure et de composition chimique. Un changement important a également été observé dans les mesures de résistivité électrique. Celle-ci augmente de 75 μΩcm pour le nc-TiN/$SiN_{1.3}$ à environ 300 μΩcm pour le nc-TiC_xN_y/SiCN avec 22,5 % atomique de C. Les couleurs ont été évaluées d'une façon quantitative par spectrophotométrie. Similairement par rapport aux couches nc-TiN/$SiN_{1.3}$, la couleur des couches nc-TiC_xN_y/SiCN change de celle de l'or à celle gris-brun.

Les résultats de ce travail ont contribué au développement du domaine des couches dures nc en permettant l'évaluation et la compréhension des relations s'établissant entre la structure et les propriétés. Ceci donnera lieu à des développements futurs et des applications pratiques des structures nc trés prometteuses. Les résultats originaux de cette thèse sont les suivants:

1. Fabrication d'un matériau de type nc-TiN/$SiN_{1.3}$ par PECVD à basse température (300 °C).
2. Élaboration d'une méthode d'évaluation des propriétés mécaniques des couches dures et ultradures, en particulier de la dureté, et de la relation entre la structure et les propriétés mécaniques, tribologiques, électroniques et optiques.
3. Optimisation de la matrice amorphe SiCN qui a été employée dans le nouveau type de matériaux nc.
4. Synthèse d'un nouveau type de matériau, nc-TiC_xN_y/SiCN présentant des propriétés mécaniques significativement supérieures à celles du nc-TiN/$SiN_{1.3}$.

Ce travail est le premier dans le domaine des couches nc ultradures dans notre laboratoire. Il a contribué à l'avancement de la recherche sur de matériaux plus performants du point de vue des propriétés tribo-mécaniques et de la méthodologie de caractérisation de ces matériaux. Ce travail peut servir comme point de départ pour la recherche future dans les directions suivantes :

1. L'exploration systématique des propriétés tribologiques dans le contexte des applications spécifiques tel que des revêtements des outils de coupe, forets, turbines, etc. Cette recherche serait concentrée particulièrement sur l'adhérence sur les substrats technologiques tel que les aciers, alliages d'aluminium et de titane et sur des carbures de tungstène.
2. Pour mieux comprendre la dynamique et le mécanisme de croissance des couches nc ultradures, monitoring *in situ* de procédés de dépôt par PECVD à l'aide des techniques telles que l'ellipsométrie, la spectroscopie de masse, et d'autres méthodes diagnostiques.
3. Évaluation plus en profondeur de la microstructure, spécialement de l'interface entre les particules cristallines et la matrice amorphe et la concentration des défauts dans les nanocristaux pour comprendre d'une façon plus quantitative leur comportement. Ces études peuvent être effectuées par le TEM à haute résolution (HRTEM) qui sera acquis sous peu par l'École Polytechnique.
4. La recherche de matériaux nouveaux, comme des oxydes ou matériaux covalents, qui peuvent être utilisés dans les couches nc ultradures possédant des caractéristiques tribo-mécaniques optimisées.

Contents

List of tables

List of figures

List of symbols

A_o – amplitude of an oscillator

A_{el} - materials constant

A_{in} – contact indentation area

a – distance between crystallographic planes

a_h – coefficient in hardness models

B – bulk modulus

B_{el} - materials constant

B_{in} – indenter constant

b – interatomic distance

b_f – radius of plastically deformed cavity in film

b_s – radius of plastically deformed cavity in substrate

$C_1 \ldots C_5$ – polynomial constants

C_{11} – elastic constant

C_{12} – elastic constant

$[\overline{C}]$ - elasticity matrix

C – geometrical constant

$[C_{bulk}]$ – carbon concentration in bulk

C_f – load frame compliance

C_s – sample's compliance

C_t – load frame compliance

c – size of a notch or crack

D – electric displacement

d_{200} – interplanar distance in <200> direction

d – grain size

E_0 – position of an oscillator

E – Young's modulus

E_f – Young's modulus of film

E_i – Young's modulus of an indenter

E_{photon} – photon energy

E_{plasma} – plasma energy

E_r – reduced Young's modulus

E_s – Young's modulus of substrate

ΔE_g – Gibb's free energy

e – electron charge

$F(r)$ – electrostatic force between atoms

F_{CH4} – CH_4 gas flow

F_c – cohesive electrostatic force between the atoms

F_i^p – incident electromagnetic wave amplitude in p polarization

F_i^s – incident electromagnetic wave amplitude in s polarization

F_r^p – reflected electromagnetic wave amplitude in p polarization

F_r^s - reflected electromagnetic wave amplitude in s polarization

f – material constant

G – shear modulus

g – material constant

H – hardness

H_a – hardness of phase a

H_{ab} – hardness of a mixture of a and b phases

H_b – hardness of phase b

H_c – composite hardness

H_f – film hardness

H_s – substrate hardness

HV – Vicker's hardness

h – indentation depth

h_c – corrected indentation depth

h_f – depth of permanent indentation

h_{max} – maximum indentation depth

h_s – depression of surface around indentation

$\hbar$ - Planck's constant

K – toughness

K_{wear} – wear rate

k – extinction coefficient

k_{in} - indentation material dependent constant

L – load

L_{max} – maximum load

$L^*a^*b^*$ - color space

l – radius at the head of a notch or a crack

M – Meyer's index

m – materials constant

m_e – electron mass

m^* - effective mass of an electron

N – complex refractive index

N_c – average coordination number

N_{el} – electron density

n – index of refraction

n_e – free electron density, plasma density

p – pressure

q – constant H at unit indentation size

R – curvature radius

R_a – arithmetic mean surface roughness

R_{el} – elastic rebound

R_s – specular reflectance

r_0 - equilibrium distance between atoms

r - distance between atoms

r_{in} – indentation constant

S_c – stress concentration factor

S_{in} – indentation stiffness

s – indentation diagonal

s_t – travelled distance

$s(E_{photon})$ – relative power distribution

T_m – melting temperature

T_s – substrate temperature

t_f – film thickness

t_s – substrate thickness

$U(r)$ – potential energy between atoms

$U_a(r)$ – attractive component of potential energy

$U_r(r)$ – repulsive component of potential energy

V – volume

V_a – volume of phase a

V_B – self bias of an electrode

V_b – volume of phase b

V_f – volume of film's plastic deformation

V_s – volume of substrate's plastic deformation

ΔV – volume of indentation

W_e – elastic energy

W_p – energy of plastic deformation

W_s – strain energy density

W_r – wear rate

W_{tot} – total work of indentation

XYZ - color tristimulus

$X_nY_nZ_n$ – tristimulus values of reference white

xyY – color space

xyz – color coordinates

$\bar{x}(E_{photon})\bar{y}(E_{photon})\bar{z}(E_{photon})$ - color matching functions

α - absorption coefficient

α_{in} – relative indentation volume

β - relative indentation size

Δ - ellipsometric angle (phase difference)

Δ_{in} – volume dilatation

$\{\bar{\varepsilon}\}$ – strain vector

$\bar{\varepsilon}$ – complex dielectric constant

ε_0 – dielectric constant of vacuum

ε_1 – real part of dielectric constant

ε_2 – imaginary part of dielectric constant

ε - strain

ε_p – plastic deformation

ε_{xx} – principal strain in x direction

ε_{yy} – principal strain in y direction

ε_{zz} – principal strain in z direction

ε_∞ - constant

$\bar{\phi}$ - ratio of electric field amplitude

Γ - broadening of an oscillator

γ_s – surface energy

γ_{xy} – shear strain in xy plane

γ_{zx} – shear strain in xz plane

γ_{yz} – shear strain in yz plane

Λ - superlattice bilayer period

λ - wavelength

λ_i - ionicity

μ - friction coefficient

θ - diffraction angle

θ_{in} – indenter's angle

$\Delta\theta$ - FWMH of X-ray diffraction peak

ρ - resistivity

$\{\bar{\sigma}\}$ – stress vector

σ_0 – constant

σ - stress

σ_{in} – intrinsic stress

σ_{max} – maximum stress

σ_{prop} – proportionality limit

σ_{th} – thermal stress

σ_{tot} – total mechanical stress

σ_u – ultimate stress

σ_{xx} – normal stress in x direction

σ_{xy} – shear stress in xy plane

σ_{xz} – shear stress in xz plane

σ_{xy}^{max} – maximum shear stress

σ_y – yield stress

σ_y^A – yield point of material A

σ_y^B – yield point of material B

σ_y^{max} – maximum cleavage stress

σ_{yy} – normal stress in y direction

σ_{yz} – shear stress in yz plane

σ_{zz} - normal stress in z direction

τ - scattering time

υ - Poisson's ratio

υ_i – Poisson's ration of indenter

υ_s – substrate Poisson's ratio

Ω - rotation angle of xy coordination system with respect to XY system

ω - angular frequency of electromagnetic wave

ω_0 – position of an oscillator

ω_p – plasma frequency

ξ - indenter semiangle

Ψ - ellipsometric angle

List of abbreviations

2D – two dimensional

3D – three dimensional

AES – Auger emission spectroscopy

AFM – atomic force microscopy

BE – binding energy

B-R – Burnett and Rickerby model

c – crystalline

CIE - Commission Internationale d'Eclairage

C-L – Chicot and Lesage model

CTE – coefficient of thermal expansion

CVD – chemical vapor deposition

D - diamond

DC – direct current

DLC – diamond like carbon

DSI – depth sensing indentation

EEDF – electron energy distribution function

ERD – elastic recoil detection

FIB – focused ion beam

FTIR – Furrier transform infrared spectroscopy

FWHM – full width at half maximum

HFCVD – hot filament chemical vapor deposition

HRTEM – high resolution transmission electron microscopy

ICH – Ichimura et al. model

IR – infrared

ISE – indentation size effect

J-H – Jonsson and Hogmark model

KOR – Korsunsky et al. model

LA – longitudinal acoustic

LECVD – laser enhanced chemical vapor deposition

LPCVD – low pressure chemical vapor deposition

MEMS – micro electromechanical systems

MW - microwave

nc - nanocrystalline

NIR – near infrared

O-P – Oliver and Pharr model

PECVD – plasma enhanced chemical vapor deposition

PET - polyethyleneterephthalate

PVD – physical vapor deposition

RF – radio frequency

SAW – surface acoustic wave

sccm – standard cubic centimeter per minute

SEM – scanning electron microscopy

SI – static indentation

SZM – structure zone model

TA – transverse acoustic

TEM – transmission electron microscopy

TO – transverse optical

TOF – time of flight

UV – ultraviolet

WI – work of indentation model

VASE – variable angle spectroscopic ellipsometry

VIS – visible light

VUV – vacuum ultraviolet

XPS – X-ray photoelectron spectroscopy

XRD – X-ray diffraction

Chapter 1. Introduction

1.1. Need for hard and protective coatings

Many areas of modern technology require materials with enhanced surface characteristics [1]. On the one hand, surface engineering allows one to tailor the surface properties of components and devices in order to make them compatible with their working environment. On the other hand, it provides new specific functions that range from enhanced durability to completely new applications. With recent advances in science and engineering, the interest in nano- and micromechanical properties [2] of thin film structures has been stimulated by the growing demand for high performance, multifunctional films and coatings. Thin film systems have to simultaneously satisfy various requirements related to their mechanical (hardness, Young's modulus, stress) [3], tribological (wear resistance, friction, adhesion) [4], and optical characteristics [5], and high stability in the environment of application. Many of these requirements are defined by the need in different sectors of industry. Good examples are the following:

a) The aerospace industry requires high performance, thermal barrier coatings on jet engine components, especially on turbine blades, stators and gas seals. In the harsh working environment of jet engines they have to operate in a large temperature range between 100 K and several thousands of K. Moreover, in order to provide high level of security and long service, the coatings must be wear- and abrasion resistant. They have to withstand the presence of abrasive particles (dust, sand or even small objects that may accidentally penetrate). At the present time, the most commonly used materials are plasma sprayed metal oxides, such as ZrO_2 stabilized with CaO, MgO and Y_2O_3 [6-7].
b) The automotive industry requires that new types of engines meet the increased environmental restrictions. To lower fuel consumption and pollution levels and to achieve the required high performance, modern combustion engines have to operate

at high pressures. Therefore, hard and protective coatings, such as diamond-like carbon (DLC), are successfully used on piston rings [8] or other engine parts [9]. In addition, many coated parts include interior and exterior components that frequently provide the required corrosion resistance and aesthetic appearance.

c) The machining industry applies hard coatings on cutting tools to increase their durability and machining speed, the latter being directly related to precision and surface finish. Moreover, in various processes, excellent performance of hard coatings eliminates the need for cooling liquids, making machining cheaper and environmentally friendly. The most popular materials for these applications are oxides and transition metal carbides and nitrides [10-11].

d) Microelectronics and MEMS devices often apply the same materials as those used as hard and protective coatings. Materials, such as TiN are used as diffusion barriers or electrical contacts; $SiN_{1.3}$ is used in MEMS for cantilevers, gears or other miniaturized devices [12]. The low friction coefficient and high wear resistance of DLC and CN_x makes them materials of choice for protective coatings on magnetic data storage media (e.g. computer hard disks) [13-14].

e) Biomedical applications range from medical instruments (e.g. diagnostic probes) to temporary or permanent implants. The presence of electrolytic liquids in the human body makes this environment very aggressive, even for traditionally applied medical stainless steel or titanium alloys. Therefore, there is a need for coatings that provide suitable mechanical properties combined with high chemical inertness. Typical examples are orthopedic or teeth implants, such as the DLC-coated hip replacements or artificial heart valves [15].

f) In other technological areas, such as optical coatings [16], the films must fulfill minimum mechanical and tribological requirements. They must possess sufficient adhesion, scratch resistance and hardness in order to allow easy handling and long term functionality. Due to their electronic properties, some hard films possess attractive gold, silver or black colors, and they are used as decorative coatings.

Consumer products, such as watches, faucets or kitchen appliances are frequently coated with films that combine durability and appeal.

The main driving forces in further development of hard and protective coatings can be summarized as follows [3]:

a) Increased performance of coated surfaces that cannot be achieved by materials in their bulk form.
b) Various aspects related to a direct (new products) or indirect (enhanced durability, lower energy consumption, less machine downtime) economic impact, or to value added products (i.e. increased performance of already existing components).
c) Environmental aspects (e.g., lower amounts or elimination of cooling liquids from machining processes and less waste due to a longer life time of components).
d) Aesthetic aspects (market investigations revealed that customers prefer attractively looking coated tools, even if their mechanical or tribological performance is comparable to the uncoated ones).

1.2. Surface engineering techniques

Surface engineering has a long tradition. Some of the oldest examples are the axe from 900 BC, that was carburized on the cutting edge to increase its hardness, and a chisel from 700 BC treated in a similar way [17]. However, only relatively recently have processes such as heat treatment, carburizing or nitriding of metallic surfaces become better understood on a scientific basis. The technologies of hard and protective coatings effectively took off in early 1970's. We can distinguish two approaches aiming at the improvement of surface properties: (i) surface modification, and (ii) deposition of coatings.

Traditional surface modification techniques applied to metallic surfaces include [18]:

a) **Heat treatment**, a process in which the machine part is heated to an elevated temperature and then rapidly quenched in water or oil.
b) **Mechanical hardening** (hammering, rolling), a process aiming at introducing a controlled number of dislocations in the surface layer of a metal or an alloy in order to increase its strength.
c) **Diffusion-controlled processes**, such as nitriding and carburizing that are performed in carbon- or nitrogen containing gases, such as methane or ammonia. At elevated temperatures, carbon or nitrogen atoms diffuse into the bulk and react, creating a hard layer. Recently, heat treatments were also successfully applied to induce phase transformation of coatings, for example, leading to the formation of composite TaC structures [19].

There exists a large number of film deposition processes for hard protective coatings, each of them possessing specific characteristics. The most popular ones are wet chemical techniques, spraying, and vapor deposition methods [1, 3, 20-21].

a) **Wet chemical techniques**, such as electroplating and electroless plating, are popular for the fabrication of decorative coatings and, to a smaller extent, of wear- or corrosion resistant coatings. They are used to deposit alloys and metals. Electroplating is based on the deposition induced by an electric current from a liquid electrolyte. The most common example is electrodeposition of Cr. Electroless plating is a non-electrical, autocatalytic process. The choice of materials is reduced with respect to electroplating. However, electroless plating can be used to deposit hard compound materials such as NiB or CoP. Generally, wet coating techniques are polluting and they progressively lose their popularity due to environmental restrictions [22-23].

b) In **spraying**, the deposited material, in the form of a powder, is totally or partially melted in a high temperature gas torch. Its particles or droplets are subsequently

deposited on the substrate, forming a coating. The thermal and kinetic energy of the impact deforms the particles that spread on the surface and intermix with the previously deposited material. Due to high cooling rates the substrate temperature is kept low and the spray process may be applied even to plastic or wood surfaces. Spraying is characterized by a high deposition rate. It is, therefore, applied for relatively thick coatings, ranging from 10 to several hundreds of μm. These types of coatings are frequently used as thermal barriers, wear- and abrasion resistant coatings on turbine blades, valves, and moving machine components [3, 6].

c) **Vapor deposition techniques** are used to prepare various types of relatively thin (up to several μm) coatings. High controllability makes these processes very attractive. Some materials can be synthesized only in this way; examples are nitrides and carbides of transition metals, some oxides and borides [24] and diamond films. Vapor deposition is compatible with different substrates; this includes metals and metal alloys (steel, titanium, aluminium), cemented carbides, ceramics and plastics. It is generally flexible enough to provide a good control of the process and, therefore, of the film structure and composition. It is also characterized by a low level of contaminants, and it is environmentally friendly.

Vapor deposition techniques can be divided in two categories: (i) PVD (physical vapor deposition) and (ii) CVD (chemical vapor deposition). PVD involves formation of vapors from a solid source using thermal energy (evaporation) or momentum transfer (sputtering). It is usually performed at low pressures to allow directional transport of gaseous species from the source to the substrate. An interesting exception is flash evaporation at atmospheric pressure, employed by Faraday in 1857 to fabricate mirrors. PVD may be used for the deposition of pure materials or compounds. Compounds are frequently deposited by reactive processes. Introducing ion bombardment to PVD allows for a better control of the growth at low temperature. In this context, additional energy brought to the growing surface by impinging ions can lead to film densification and

structural transformation similar to that induced by temperature. These aspects are well described by the structure zone models (SZM) [25-28].

The SZM was first introduced by Movchan and Demchishin based on evaporated films. In this model, the structure and morphology of films are a function of adatom mobility, or energy, expressed as a universal T_s/T_m ratio, where T_s is the substrate temperature during deposition, and T_m is the melting temperature of the evaporated material. Thornton extended this model for sputtering processes by including a second parameter, namely the gas pressure. Further development of the SZM model by Messier et al. accounted for ion bombardment that controls adatom mobility. Recently, the SZM was further extended by Kelly and Arnell who distinguished between the contributions of energy and flux of ions bombarding the growing film.

Thermal CVD is based on material transfer from the gas phase to the substrate surface, where the precursor molecules are dissociated by heat, and their chemical reactions lead to the formation of a coating. The popularity of CVD is due to a possibility to fabricate a wide variety of materials, such as metals or semiconductors in pure or compound state. Contrary to PVD, CVD processes are not limited by the line-of-sight geometry. It allows for uniform coatings, independently of substrate geometry, as long as the surface is exposed to the gas flow and is uniformly heated. This particular aspect has a big advantage in coating a large number of small, three dimensional objects. Control of the deposition process parameters allows for the variation of stoichiometry and control of the growth processes over a wide range. CVD is frequently encountered in microelectronics and optoelectronics for the growth of semiconductor epitaxial films, and for the fabrication of hard and protective coatings. However, in the latter case, these processes generally require high substrate temperatures, in the range of 450-750 ^{o}C, or even more.

Other variations of the CVD technique have been introduced; this includes low pressure CVD (LPCVD), laser enhanced CVD (LECVD), hot filament CVD (HFCVD), and

plasma enhanced CVD (PECVD). In the present work, we apply the PECVD method. In this technique, the energy for initiation of the chemical reactions is delivered by an electric discharge in a reactive gas mixture. Gas molecules are dissociated by inelastic collisions with energetic electrons (~ 1 - 20 eV), forming free radicals, ions and vacuum ultraviolet (VUV) irradiation. Therefore, the deposition temperature can be much lower than in the case of traditional CVD. This contributes to lower thermal stresses and a wider choice of substrates. Particular advantages of PECVD are a "chemically rich" environment, leading to reactions in the gas phase, and controlled ion bombardment of the substrate that densifies the growing film and controls its structure.

PECVD in glow discharges is usually performed at low pressures, in the range from 10^{-4} Torr to several Torr ($1.33*10^{-2}$ to about 500 Pa). Under these conditions, the density of electrons (or ions, plasma density, n_e) is typically between $1*10^{9}$ and $1*10^{11}$ cm^{-3}. In such weakly ionized plasmas the degree of ionization is low ~ $1*10^{-4}$. During the last two decades, there has been a lot effort to develop new plasma reactors that allow one to better control the electron energy distribution function (EEDF) and hence the discharge efficiency [29].

Modern vacuum deposition technologies require appropriate control of the energy and flux of the bombarding ions. In this respect our laboratory has developed new high frequency plasma deposition approaches, in particular the dual-mode microwave/radiofrequency (MW/RF) technique suitable for the fabrication of dielectric, optical and hard functional coatings [30-33]. In this method, the MW discharge component represents a rich source of ions due to a high population of electrons in the tail of the EEDF [34]. This generally leads to a high ion flux. Applying the RF power to the substrate holder in a capacitively coupled discharge leads to the formation of a self-induced DC negative bias voltage, V_B. The value of V_B allows one to control the energy of the bombarding ions proportional to the difference between the plasma potential and

V_B. Ion energy distribution functions in the continuous and pulsed MW/RF, MW and RF discharges represented the subject of the Ph.D. thesis of Dr. Oleg Zabeida [35-36].

In the context of hard coatings, the MW/RF, MW and RF approaches were applied to the fabrication of DLC [32] and polycrystalline diamond films [37], and to bias-enhanced nucleation of diamond [32].

1.3. Characteristics of hard and protective coatings

In order to increase their performance, hard coating systems usually consist of several functional layers as illustrated in Fig. 1.1. From the substrate upward, we can distinguish an adhesive layer, thermal barrier, hard coating and surface lubricating layer. Such structure has to provide optimal performance under specific working conditions. Each functional layer should be carefully designed, since the behavior of the complete system depends on the characteristics of individual constituents. Usually, the main problem is that several requirements have to be satisfied simultaneously. Therefore, the coating properties must be optimized, frequently resulting in a compromise between individual properties such as hardness, toughness, adhesion, friction, corrosion, thermal conductivity and wear resistance [4, 38-39].

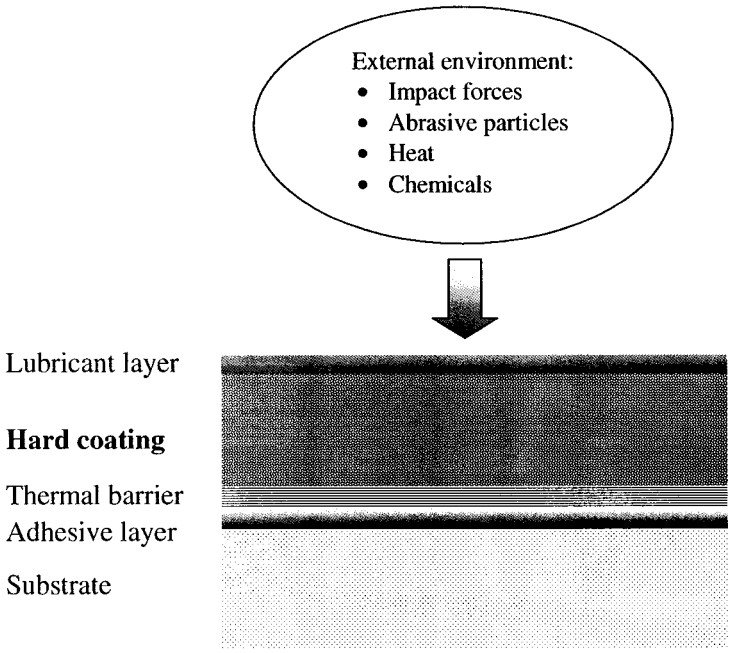

Figure 1.1. *Schematic illustration of the structure of a hard coating such as in a system applied for cutting tools.*

Recent progress in the area of new vacuum-based film fabrication and surface treatment techniques, in particular PVD, CVD and PECVD [1, 3, 20-21], stimulated further development of new materials and thin film systems. A general classification of hard coatings is presented in Fig. 1.2. Many hard films are based on nitrides and carbides of transition metals. Their interesting properties are due to a possibility to mix covalent and metallic bonds. The most popular examples that have already proven their excellent mechanical properties are TiN [40-48], VN [49], ZrN [50] and TiC [24, 51-58]. In an attempt to further benefit from the specific advantages of such coatings, ternary and quaternary structures were fabricated. Typically, the alloying elements are chosen from the groups V (B) and VI (C) of the periodic table, but they may also include Al, Si, Cu, Pd, Cr, Y etc. There are numerous examples such as (Ti,Al)N [59-61], (Ti,Al,Cr,Y)N [62], and (Ti,Al,Cr)N [63] that form crystalline solid solutions. Additional alloying elements may increase hardness, adhesion or chemical stability at high temperatures. Introducing chalcogenides, that are known as solid lubricants (e.g. Mo), leads to a

decrease of the friction coefficient. A popular example is MoS_2 applied as a dry lubricant on top of TiN for coatings used for dry cutting and milling [64].

An important category of hard coatings are covalently bonded carbon and boron compounds. This includes polycrystalline or "nanocrystalline" diamond, DLC [65-66], CN_x [67-68], BN [3] or some ternary compounds, such as B-N-C [69] or Si-C-N [70]. Their popularity is due to their excellent mechanical, thermal, optical and electronic behavior. They are applied as hard and wear resistant coatings, as electrical insulators possessing high thermal conductivity in electronic applications, or in optics. However, their unique properties are accompanied by a relatively narrow window of deposition process parameters, often poor adhesion to various substrates, and limited thermal stability, as in the case of amorphous hydrogenated carbon.

Another group of hard coatings are ionic ceramic oxides [1, 3-4]. They can be fabricated by different deposition techniques and are characterized by good tribological properties and low thermal conductivity. Examples include CVD Al_2O_3 coatings on cemented carbide cutting tools and plasma sprayed ZrO_2 thermal barriers. Other, less extensively studied materials are titanium, cadmium and chromium oxides.

The traditionally used binary, ternary or quaternary systems described above frequently possess a limited hardness and toughness due to the formation and propagation of dislocations and cracks [1-3]. More recently, research has focused on the design and development of thin film systems with a microstructure controlled on the nanometer scale. Two approaches should be mentioned in this particular context: superlattices (2D structures) [71-72] and nanocomposites (3D structures) [73-76].

Superlattices are stacks of very thin layers with a lattice period ranging from 5 to 50 nm. Nanocomposites are formed by nanocrystals that can be embedded in the matrix of an amorphous or crystalline material. In both cases, the concept of enhanced hardness is

based on multiple boundaries between layers (superlattices), and grains (nanocomposites). Important parameters in these structure-controlled materials are the lattice period, grain size, intergranular distance, and the type of interface. Recent advances in this field allow one to control these parameters thanks to a better understanding of the deposition and characterization techniques. Novel nanocomposite materials offer unique properties, such as "superhardness" (> 40 GPa), high toughness, and high thermal stability. Each of these structures may be applied in more complex coatings possessing a multilayer design. Basic concepts of nanostructured materials are described in Chapter 2, and they form the basis of this Ph.D. thesis.

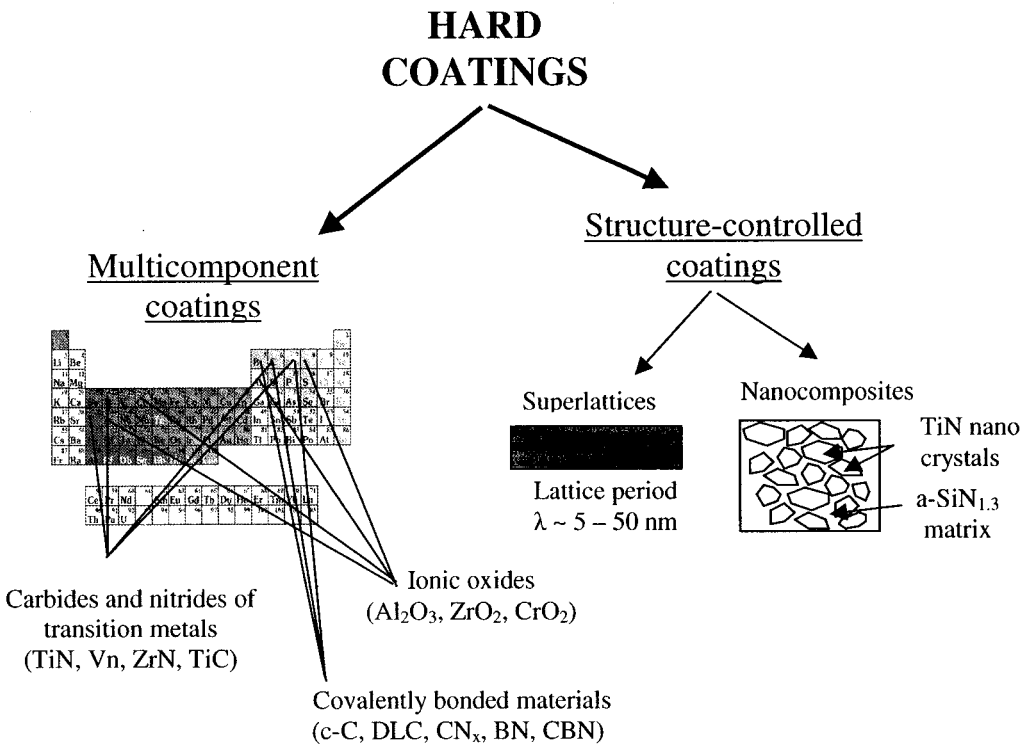

Figure 1.2. *Classification of hard coatings.*

1.4. Objectives of the thesis

There has been considerable progress in the area of hard and superhard coatings, especially during the last several years, when nanocomposites have been introduced.

However, there are still numerous open questions related to the understanding of the film synthesis, to the structure-property relationships and to the interpretation of the materials characterization tests (metrology).

In the past, our laboratory has developed an expertise in the fabrication and characterization of hard coatings such as crystalline diamond (c-D) [77], DLC [78], surface treatments, such as hardening of metals by carburizing [19], and plasma surface treatment and coating of polymers [79]. The subject of this thesis extends this work to novel approaches, such as the fabrication of new nanostructured superhard materials. The following aspects are important for advancement in the field of superhard coatings and they represent the objectives of this work:

- To develop a low temperature PECVD process suitable for the fabrication of novel, superhard nanocomposite coatings with enhanced functional characteristics.
- To optimize the model nanocomposite materials and to compare their performance with other hard coating systems.
- To develop a methodology of testing the films' elasto-plastic and tribological properties.
- To determine the relation between the films' microstructure and the elasto-plastic, tribological and optical properties.

1.5. Organization of the thesis

This thesis is divided into 8 chapters. Chapter 2 gives a theoretical background to the materials science of hard coatings, especially the concept of failure mechanism and nanostructured materials. Chapter 3 describes the methodology of film fabrication, of the mechanical and optical testing and of the assessment of the film microstructure. The principal results of this thesis are presented in the form of four articles (Chapters 4 – 7). The first article (Chapter 4: "Relationship Between the Mechanical Properties and the

Microstructure of Nanocomposite $TiN/SiN_{1.3}$ Coatings Prepared by Low Temperature Plasma Enhanced Chemical Vapor Deposition") describes the development and optimization of the low temperature PECVD process for the synthesis of nanocomposite $TiN/SiN_{1.3}$ coatings. Special attention is paid to the methodology of the measurement of mechanical properties using static and dynamic indentations. The second article (Chapter 5: "Optical Characteristics and Color of $TiN/SiN_{1.3}$ Nanocomposite Coatings") extends the work on hard $TiN/SiN_{1.3}$ films to their optical properties and color effects that were quantitatively evaluated.

The third article (Chapter 6: "Mechanical and Optical Properties of Hard SiCN Coatings Prepared by Low Temperature PECVD") describes the microstructure and the mechanical and optical properties of SiCN films obtained by incorporating carbon into $SiN_{1.3}$. This material then forms a matrix of a new nanocomposite described in the subsequent chapters. The fourth article (Chapter 7: "Quaternary Hard Nanocomposite $TiC_xN_y/SiCN$ Coatings Prepared by PECVD") reports our work on a multicomponent nc-$TiC_xN_y/SiCN$ coating that exhibits a further increase of hardness and enhanced tribological properties. The mechanical and optical properties of these films are evaluated, interpreted in terms of the structure-property relations, and compared with other hard protective functional coatings. Finally, Chapter 8 summarizes the work accomplished in this thesis and outlines new avenues of ultrahard materials.

The results generated during this thesis project led to 4 articles in refereed journals (Chapters 4 - 7), 2 articles in the proceedings of international conferences, and 6 oral and poster conference presentations.

Chapter 2. Theoretical background to the materials science of hard coatings

This Chapter introduces the basic concepts of materials strength and fracture mechanics. The theory of materials resistance to elastic and plastic (permanent) deformation is presented in sections 2.1 and 2.2. We particularly discuss the discrepancy between the theoretically predicted values of materials strength, expressed as yield stress, and the real ones measured in laboratory or observed in practice. This difference is explained in section 2.3 that introduces the Griffith theory of stress concentration and the principles of plastic deformation. Using theoretical considerations described earlier, section 2.4 explains the concept of nanostructured materials, such as superlattices and, in particular, nanocomposites.

2.1. Elastic properties and Hooke's law

Hooke's law describes the elastic behavior of a solid body in a linear approximation. The general form of the Hooke's law for a 3 dimensional anisotropic body can be written in the matrix form [80-81]:

$$\{\bar{\sigma}\} = [\bar{C}]\{\bar{\varepsilon}\}, \tag{2.1}$$

where $\{\bar{\sigma}\} = [\sigma_{xx}\ \sigma_{yy}\ \sigma_{zz}\ \sigma_{yz}\ \sigma_{zx}\ \sigma_{xy}]^T$ is a stress vector, as shown in Fig. 2.1, $\{\bar{\varepsilon}\} = [\varepsilon_{xx}\ \varepsilon_{yy}\ \varepsilon_{zz}\ \gamma_{yz}\ \gamma_{zx}\ \gamma_{xy}]^T$ is the corresponding strain vector, and $[\bar{C}]$ is the stiffness or elasticity matrix. $[\bar{C}]$ contains 21 elastic constants that are necessary to characterize the elastic behavior of an anisotropic material.

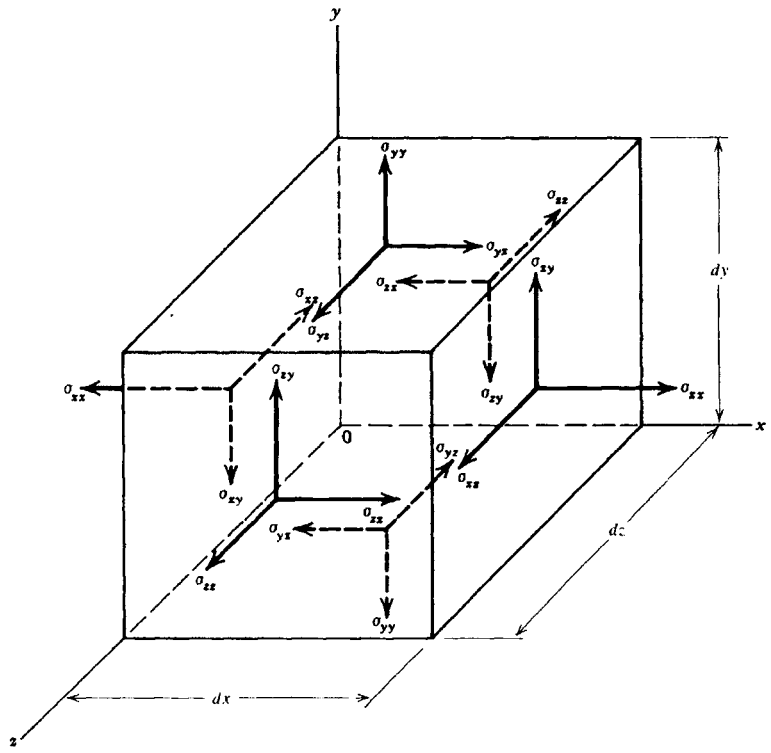

Figure 2.1. *Stress components in the Cartesian coordinate system* [81].

Most engineering materials possess elastic symmetries that define the directions along which the elastic properties are the same. This allows one to simplify the $[\overline{C}]$ matrix and to reduce the number of elastic constants. For example, orthotropic materials such as fiber-reinforced composites or PET (polyethyleneterephthalate) possess three principal material directions and can be described by nine elastic constants. No material is fully isotropic, but for many of them an isotropic approximation may be applied. For example, metals, due to a random orientation of grains on the macroscopic scale, may be considered isotropic.

For isotropic materials the elastic properties do not depend on the direction and, therefore, the number of elastic constants can be reduced. Eq. 2.1 may then be expressed by a $[\overline{C}]$ matrix possessing only two independent elastic constants:

$$\begin{Bmatrix} \sigma_{xx} \\ \sigma_{yy} \\ \sigma_{zz} \\ \sigma_{yz} \\ \sigma_{zx} \\ \sigma_{xy} \end{Bmatrix} = \begin{bmatrix} C_{11} & C_{12} & C_{12} & 0 & 0 & 0 \\ C_{12} & C_{11} & C_{12} & 0 & 0 & 0 \\ C_{12} & C_{12} & C_{11} & 0 & 0 & 0 \\ 0 & 0 & 0 & \frac{C_{11}-C_{12}}{2} & 0 & 0 \\ 0 & 0 & 0 & 0 & \frac{C_{11}-C_{12}}{2} & 0 \\ 0 & 0 & 0 & 0 & 0 & \frac{C_{11}-C_{12}}{2} \end{bmatrix} \begin{Bmatrix} \varepsilon_{xx} \\ \varepsilon_{yy} \\ \varepsilon_{zz} \\ \gamma_{yz} \\ \gamma_{zx} \\ \gamma_{xy} \end{Bmatrix}, \quad (2.2)$$

where $C_{11} = \frac{E(1-\upsilon)}{(1+\upsilon)(1-2\upsilon)}$, and $C_{12} = \frac{E\upsilon}{(1+\upsilon)(1-2\upsilon)}$. The term $\frac{C_{11}-C_{12}}{2} = G$ is defined as shear modulus, E is the Young's modulus and υ is the Poisson's ratio.

An important elastic property of an isotropic material is the bulk modulus, B, that expresses the change of volume, Δ_{dil}, under the hydrostatic stress state defined as $\sigma_{xx} = \sigma_{yy} = \sigma_{zz} = -p$ and $\sigma_{yz} = \sigma_{zx} = \sigma_{xy} = 0$. Substituting for the stress values in Eq. 2.2 and adding the equations we obtain:

$$p = -\frac{C_{11}+2C_{12}}{3}(\varepsilon_{xx}+\varepsilon_{yy}+\varepsilon_{zz}) = -B\Delta_{dil} \quad (2.3)$$

Inverting the $[\overline{C}]$ matrix and substituting for C_{11} and C_{22} one can obtain the total strain $\{\overline{\varepsilon}\}$ as a function of the stress vector $\{\overline{\sigma}\}$:

$$\begin{aligned} \varepsilon_{xx} &= \frac{1}{E}[\sigma_{xx} - \upsilon(\sigma_{yy}+\sigma_{zz})] \\ \varepsilon_{yy} &= \frac{1}{E}[\sigma_{yy} - \upsilon(\sigma_{xx}+\sigma_{zz})] \\ \varepsilon_{zz} &= \frac{1}{E}[\sigma_{zz} - \upsilon(\sigma_{xx}+\sigma_{yy})] \\ \gamma_{yz} &= \frac{1}{G}\sigma_{yz} \\ \gamma_{zx} &= \frac{1}{G}\sigma_{zx} \\ \gamma_{xy} &= \frac{1}{G}\sigma_{xy} \end{aligned} \quad (2.4)$$

The strength of bulk materials can be empirically measured using a tensile test. In such a test, the specimen is subjected to uniaxial tension, σ_{xx}. Other stress components from Eq. 2.4 become zero, leading to $\sigma_{xx} = E\varepsilon_{xx}$. The $\sigma(\varepsilon)$ dependence provides information about the elasto-plastic behavior of a given material [81-82]. An example of a tensile test for brittle and ductile materials is shown in Fig. 2.2.

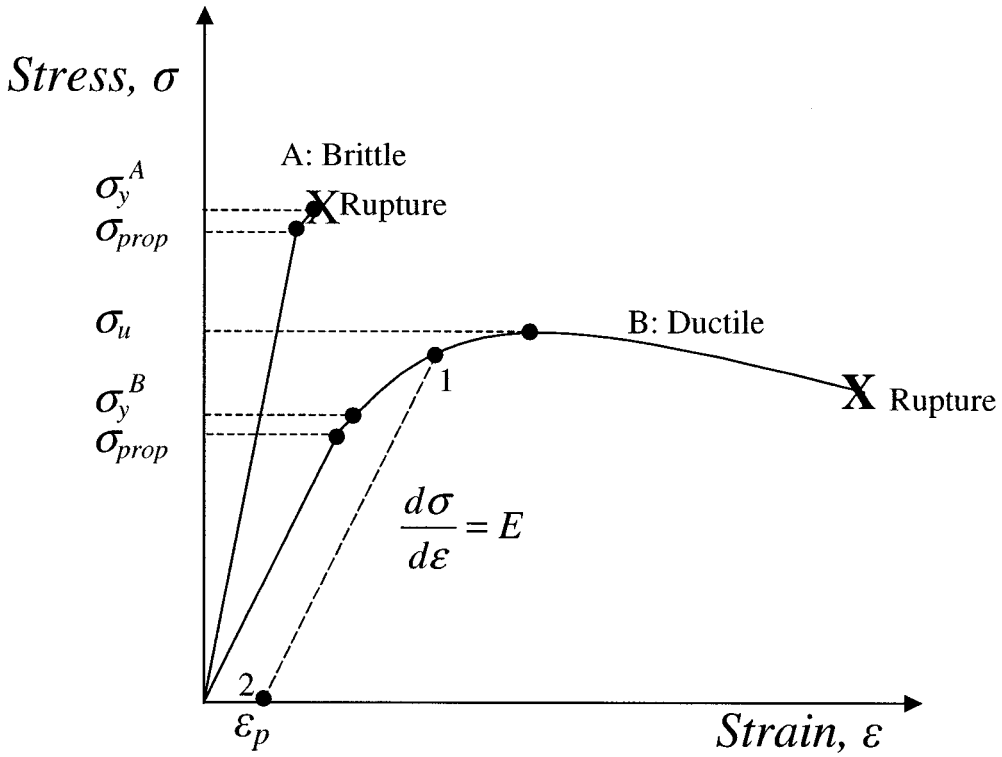

Figure 2.2. *Schematic presentation of the stress-strain relation for brittle (A) and ductile (B) materials.*

Hooke's law describes the linear part of the $\sigma(\varepsilon)$ dependence up to the so-called proportionality limit σ_{prop}. It expresses the resistance to elastic deformation. The elastic limit, or yield point, σ_y, up to which the deformation of a solid body is reversible, is slightly higher than the proportionality limit. In practice, the difference between them is negligible and they can be considered equal. σ_y defines the strength of the material. For

brittle materials, rupture occurs beyond $\sigma_y = \sigma_y^A$. Ductile materials deform plastically when the stress exceeds $\sigma_y = \sigma_y^B$.

In the examples presented in Fig. 2.2, material A is strong (high value of σ_y^A), and it possesses high E represented by the steep slope of $\sigma(\varepsilon)$. However, at the same time it is brittle and it ruptures when the applied stress exceeds σ_y^A. Material B is less strong, but it is ductile. If loaded beyond σ_y^B up to point 1 and then unloaded, the $\sigma(\varepsilon)$ dependence is linear till the final point 2. As a consequence, permanent plastic deformation occurs, represented by the final elongation ε_p. By subsequent loading the $\sigma(\varepsilon)$ dependence follows the 2-1 line in the elastic regime, up to the new, higher value of σ_y^B, in point 1. This phenomenon is called the strain hardening and is explained in section 2.3. Strain hardening may continue up to an ultimate stress value, σ_u. Beyond σ_u the material cannot support σ and fails by a drastic deformation and subsequent rupture. Therefore, σ_u is the limit of practical applications for ductile materials.

2.2 Theoretical strength of materials

This section provides a background to estimate the limit of elastic deformation σ_y that, in fact, defines the strength of materials. The notion of the theoretical strength applies to homogeneous materials that do not contain any imperfections in the form of cracks, inclusions, crystal defects or dislocations. The cohesive strength of a solid body is assured by the electronic interactions between the atoms. A solid body is stable due to the fact that the total energy of bonded atoms is lower than if they are considered separately [18]. The difference between these two energies defines the cohesive energy.

Any macroscopic deformation of a solid starts on an atomic level when the atomic bonds are stretched or compressed and the potential energy between atoms, $U(r)$, changes. Function $U(r)$ is the generalized characteristics common for all types of solids,

independently from the type of bonding and structure. It can be expressed as the sum of attractive, $U_a(r)$, and repulsive, $U_r(r)$, components [83]:

$$U(r) = U_a(r) + U_r(r). \tag{2.5}$$

Generally, $U_a(r)$ and $U_r(r)$ are expressed as as:

$$U_a(r) = -\frac{A_{el}}{r}, \tag{2.6}$$

$$U_r(r) = \frac{B_{el}}{r^m}, \tag{2.7}$$

where A_{el} and B_{el} are materials constants depending on the number of protons and electrons, r is the interatomic distance, and m is a constant that depends on the type of the chemical bond. It varies between 6 and 9 for metallic bonds, and between 9 and 11 for ionic and covalent bonds [84]. Relation between $U(r)$, $U_a(r)$, and $U_r(r)$ is illustrated in Fig. 2.3.

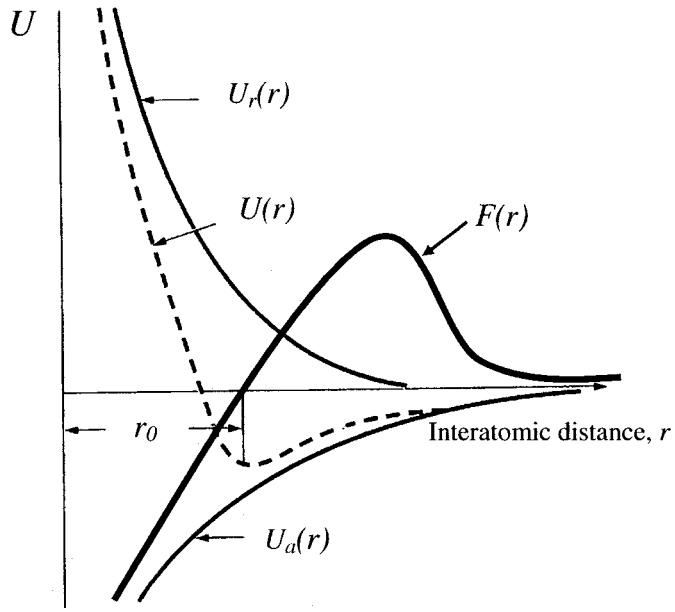

Figure. 2.3. *Potential energy, U(r), between two atoms and the resulting interatomic force, F(r)* [18].

It follows from Fig. 2.3 that the attractive component dominates when r is large, i.e. exceeding two or three times the diameter of the atom. When atoms get closer the repulsive component increases due to the interactions between the core electrons as predicted by Pauli's exclusion principle. At a certain optimal interatomic distance, r_0, $U(r)$ exhibits a minimum, $U(r_0)$ that corresponds to a cohesive energy (or sublimation enthalpy) between two atoms. This energy must be delivered to the system to transform it from solid phase to gas phase.

The force $F(r)$ acting on an atom, within the electrostatic field is obtained as the first derivative of $U(r)$:

$$F(r) = \frac{dU(r)}{dr}. \tag{2.8}$$

The energy minimum, $U(r_0)$, that corresponds to $F(r_0) = 0$, represents a stable equilibrium position. A theoretical cleavage stress, necessary to break this equilibrium, was first estimated by Orowan [85]. He assumed that the work of fracture must be at least equal to the surface energy, γ_s, of two new surfaces created during fracture. Therefore, integration of the area under the $F(r)$ curve from equilibrium position at $r = r_0$ gives the theoretical strength, in terms of the so called maximum cleavage stress, σ_y^{max}:

$$\sigma_y^{\max} = \sqrt{\frac{2E\gamma_s}{r_0}}, \tag{2.9}$$

One can observe from Eq. 2.9 that strong solids possess high atomic density, i.e. small r_0. Small value of r_0 implies deep energetical minima of $U(r)$, high curvature of $U(r_0)$ and consequently high slope of $F(r_0)$, that corresponds to high values of E.

For common solid state engineering materials, Eq. 2.9 gives an estimation of $\sigma_y^{max} = E/10$. However, the experimental values of σ_y are between $E/100$ and $E/1000$, i.e. up to two orders of magnitude smaller than the value predicted theoretically [84]. More exact calculations for covalently bonded and ionic solids were performed by Zwicky [86], Borr and Furth [87], and Tyson [88]. Their calculations were based on estimations of $U(r)$ for

specific materials. They resulted in estimations for σ_y^{max} lower than the one predicted by Orowan (Eq. 2.9), but still within the same order of magnitude.

Ductile materials fail by plastic deformation rather than fracture when σ_y is exceeded, as shown in Fig. 2.2. Therefore, the theoretical strength can also be expressed in terms of the maximum value of the shear stress σ_{xy}, beyond which the atomic planes in crystalline materials slide with respect to each other. Such active sliding planes are characterized by a high atomic density, accompanied by smaller interatomic distances. Thus the energy threshold to move two atomic planes with respect to each other is also smaller [18, 84]. Fig. 2.4 presents the stress components in a two dimensional square object, subjected to an external stress vector [σ_{XX}, σ_{YY}, σ_{XY}]. Here, the plane stress is defined by $\sigma_{XZ} = \sigma_{YZ} = \sigma_{ZZ} = 0$.

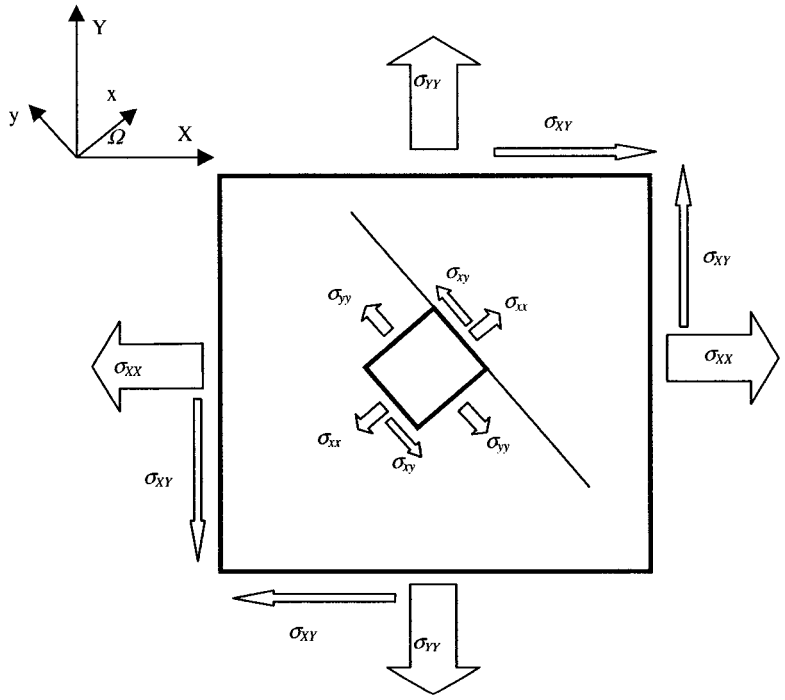

Figure 2.4. *Stress components in two dimensions.*

In order to mathematically describe the relationship between the externally applied stress vector and the resulting stress on the microscopic scale, let us consider an infinitely small

object situated within a square and rotated by an arbitrary angle Ω with respect to the XY coordinate system. Using appropriate geometrical relations and the force and momentum equilibrium rules, the stress vector components in the local xy coordinate system can be expressed as [81-82]:

$$\begin{aligned}
\sigma_{xx} &= \frac{1}{2}(\sigma_{XX} + \sigma_{YY}) + \frac{1}{2}(\sigma_{XX} - \sigma_{YY})\cos 2\Omega + \sigma_{XY}\sin 2\Omega \\
\sigma_{yy} &= \frac{1}{2}(\sigma_{XX} + \sigma_{YY}) - \frac{1}{2}(\sigma_{XX} - \sigma_{YY})\cos 2\Omega - \sigma_{XY}\sin 2\Omega, \\
\sigma_{xy} &= -\frac{1}{2}(\sigma_{XX} - \sigma_{YY})\sin 2\Omega + \sigma_{XY}\cos 2\Omega
\end{aligned} \tag{2.10}$$

where the capital subscripts refer to XY and the low case subscripts to the xy coordinate system. For uniaxial conditions, as in pure tension, i.e. $\sigma_{XX} = 0$ and $\sigma_{XY} = 0$, the maximum value of shear, σ_{xy}, is obtained for $\Omega = 45^{\circ}$. In such case:

$$\sigma_{xy}^{\max} = \frac{1}{2}\sigma_{YY}. \tag{2.11}$$

In polycrystalline materials certain crystals are oriented in directions such that $\sigma_{xy}^{\max}$ coincides with the planes of maximum atomic density. Such planes represent the weakest points of the material, and, therefore, they define the maximum value of σ_{xy}. Eq. 2.11 is the so called Tresca yield criterion [80-81] and it expresses a minimum shear value representing the elastic limit:

$$\sigma_y = 2\sigma_{xy}^{\max}. \tag{2.12}$$

The calculation of σ_{xy}^{max} in crystals was done by Frenkel [89]. He considered two atomic planes with an interatomic distance b, and situated at a distance a from each other. Assuming that the crystal planes remain undistorted, he arrived at the following estimation of the maximum value of shear stress:

$$\sigma_{xy}^{\max} = \frac{G}{2\pi}\frac{b}{a}. \tag{2.13}$$

Eq. 2.13 confirms our previous assumption, namely that yielding starts along the planes with the highest atomic density that possess a small b/a ratio. From equation 2.12 the theoretical elastic limit above which plastic deformation occurs in ductile materials is:

$$\sigma_y = 2\sigma_{xy}^{max} = \frac{G}{\pi}\frac{b}{a} \approx \frac{E}{8}\frac{b}{a}. \qquad (2.14)$$

To approximate σ_y, we can assume that $a = b$, as for a material possessing a cubic lattice. This condition leads to a surprisingly high value of $\sigma_y = E/8$. Again, as in the case of brittle materials, the theoretical elastic limit is much higher than the one measured experimentally during the tensile tests. Similar results were obtained by other approaches and estimations based on the Morse function (Eq. 2.5) by Mackenzie [90], and Tyson [91].

Based on the above considerations, we may conclude that ideal strong solids, also characterized by a high value of hardness, H, and E, should possess a high value of both σ_{xy}^{max} and σ_y^{max}. The relation between H and σ_y is explained in Chapter 3. H is further related to the strength of interatomic bonds, that implies high cohesive energy and short bond length [1] as illustrated in Fig. 2.5. One can conclude that hard (or strong) materials are covalently bonded. Ionic bonds are less strong and they result in lower hardness.

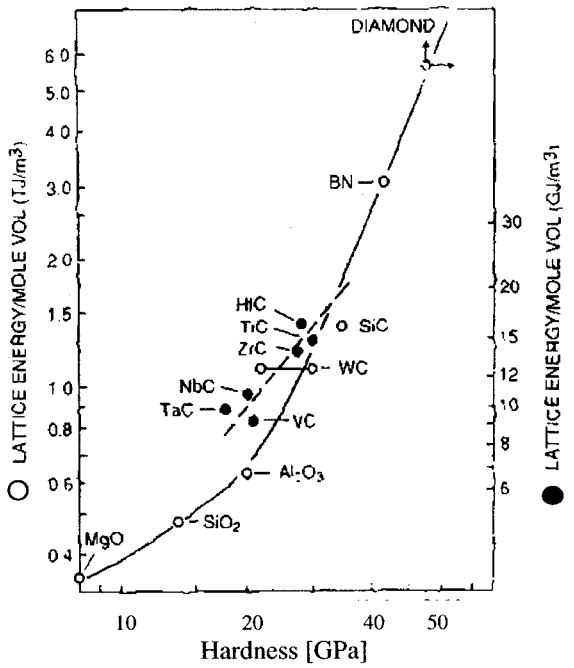

Figure 2.5. *Relation between cohesive energy per molar volume and hardness* [1].

Above conditions for high hardness are satisfied by light elements, such as: beryllium, boron, carbon, nitrogen, oxygen, aluminium, and silicon. Examples of such materials applied in engineering are diamond (H = 100 GPa, E = 1050 GPa), boron (H = 35 GPa, E = 470 GPa), boron nitride (H = 48 GPa, E = 440 GPa), and sapphire (H = 30 GPa, E = 441 GPa). Materials frequently employed for hard coatings are nitrides and carbides of transition metals. Examples are TiN (H = 21 GPa, E = 350 GPa), TiC (H = 30 GPa, E = 460 GPa), and CrN (H = 11 GPa, E = 400 GPa) [1, 3].

In 1985 Cohen performed a theoretical design of a strong solid. He developed an empirical formula for calculating the bulk modulus, B, of tetrahedral covalent solids [92-94]:

$$B = \frac{N_c}{4}\frac{(19.71 - 2.20\lambda_i)}{r_0^{3.5}}, \tag{2.15}$$

where N_c is the average coordination number and λ_i is the ionicity, an empirical parameter ranging from 0 to 2 depending on the polarizability of the atoms. λ_i = 0 for group IV, λ_i = 1 for groups III and V, and λ_i = 2 for group II and IV materials. From Eqs. 2.2 and 2.3, we can see that a high value of E for strong solids is related to a high value of B:

$$B = \frac{E}{3(1 - 2\upsilon)} \tag{2.16}$$

Using Eq. 2.15 Liu and Cohen predicted a hypothetical form of carbon nitride, β - C_3N_4, that possesses B = 427 GPa, close to that of diamond (443 GPa). For comparison, Table 2.1 shows the calculated and measured B values for some strong covalently bonded solids and corresponding H values.

Table 2.1. *Calculated and measured bulk modulus values for some strong covalently bonded solids* [95].

Material	r [Å]	λ_i	B [GPa] (calculated)	B [GPa] (measured)	H [GPa] (measured)
Diamond	1.54	0	435	443	100
c-BN	1.56	1	369	367	45
β - Si_3N_4	1.74	0.5	265	256	17
β - C_3N_4	1.47	0.5	427	---	---

As can be seen in Table 2.1, the calculated B values agree well with the measured ones for a number of materials, suggesting that β-C_3N_4 may indeed have a strength comparable to that of diamond. The total cohesive energy per a C_3N_4 molecule was found to be 40.7 eV, corresponding to an average energy of 5.8 eV per atom. This suggests that highly energetic conditions should be used to synthesize this material.

Prediction of the β-C_3N_4 phase stimulated an extensive effort to synthesize this material using all available PVD- and CVD-based deposition techniques [96]. It appeared clear at an early stage that crystalline stoichiometric β-C_3N_4 films are not readily achievable. An important limitation was the amount of N that could be incorporated in the structure. Furthermore, most efforts resulted in predominantly amorphous microstructures. The hardest CN_x "fullerene-like" films reached H of 40 – 60 GPa [67]. However, these very high measured values of H may be influenced by high values of elastic rebound, R_{el} that reaches up to 90 % [68].

2.3. Real strength of materials

Usually, for a given material σ_y^{max} is higher than σ_{xy}^{max} since the latter value describes a situation when atomic planes slide along the slip planes and no new surfaces are generated [83]. Ductile materials, for which the dislocation movement is not restricted and plastic deformation is possible, are characterized by a small $\sigma_{xy}^{max}/\sigma_y^{max}$ ratio. Therefore, the theoretical strength of ductile materials, such as metals, is limited by σ_{xy}^{max}

and they fail by plastic deformation. In brittle solids with covalent or strongly polarized ionic bonds dislocation movement is limited. Consequently, these materials possess high values of the $\sigma_{xy}^{max} / \sigma_y^{max}$ ratio; their theoretical strength is limited by σ_y^{max} and they fail by brittle fracture.

A comparison of the E, σ_y and H values for standard ductile and brittle engineering materials is given in Table 2.2 [84]. One can see a large difference between the theoretical value of $\sigma_y \sim E/10$, and the experimental one for brittle materials, such as glass or Al_2O_3, and for the ductile ones, such as aluminium alloys. Carbon fibers are characterized by excellent mechanical properties in terms of E and σ_y, however, only in the direction of the fibers. Their anisotropic properties are the result of preferential orientation of carbon crystallites. In the case of steel we observe that by proper alloying and hardening processes, a remarkable improvement of σ_y may be achieved. However, even in the case of high speed steel, $\sigma_y = E / 70$.

Table 2.2. *Comparison of E, σ_y and H values of selected "engineering" materials* [84].

Material	E *[GPa]*	σ_y [MPa]	*H* [GPa]
Aluminium alloys	70	90 – 150	0.4 – 0.7
Steel	210	180 – 500	4
High Speed Steel	210	1000 – 3000	9
Glass	71	30 – 90	3 - 6
Alumina	380	200 – 300	21
Fused Silica	150	69 - 250	10 - 11
Carbon Fibers (in axial direction)	400	1500 – 2500	----

The discrepancy between the theoretical and the real strength of brittle materials can be explained by the theory of stress concentration. Important experimental work that led to the development of this theory was performed by Griffith [83]. Generally, stress concentration in materials subjected to an external load is due to internal imperfections and discontinuities in the structure, such as cracks, crystal dislocations, inclusions or voids. Stress concentrations may be also due to the nonuniform loading points where

external forces are applied. In practical situations the failure of material is due to crack propagation or crack formation because of high stress gradients. Stress fields in the vicinity of imperfections appear in three dimensional forms, and therefore, are relatively difficult to express analytically.

If we consider a simple homogeneous bar subjected to a tensile stress, the internal stress is uniformly distributed over the cross section, provided that the applied forces are sufficiently distant. Nonuniformity, for example, in the form of a notch, leads to a stress concentration in its vicinity. The maximum value of stress, σ_{max}, may be considerably larger than the mean applied stress. The stress trajectories can be visualized as continuous lines running in the direction of the applied forces. In order to assure continuity, as required by mechanical equilibrium, stress trajectories concentrate in the vicinity of imperfections, such as the notch illustrated in Fig. 2.6.

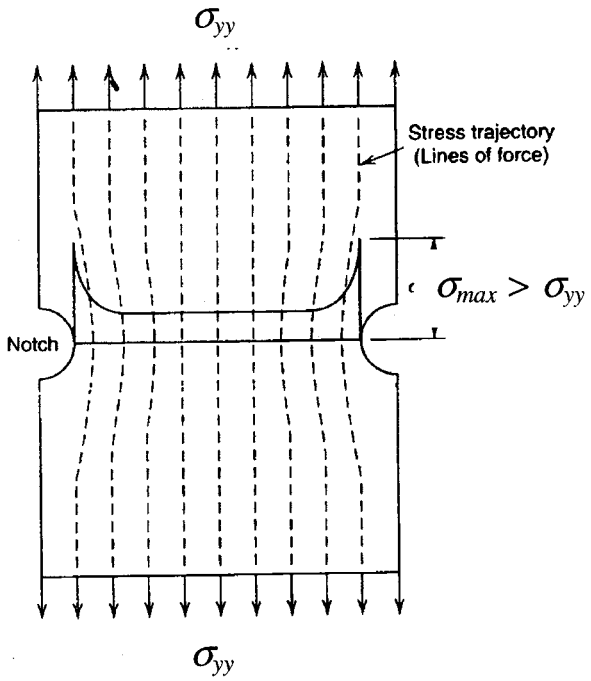

Figure 2.6. *Stress concentration in the vicinity of a notch* [81].

Theoretical calculations lead to the following stress value at the head of the notch [81]:

$$\sigma_{\max} = \left(1 + 2\sqrt{\frac{c}{l}}\right)\sigma_{yy} = S_c \sigma_{yy}, \tag{2.17}$$

where c is the length of the notch (or crack, in general), l is the radius at the head of the notch, and S_c is the so-called stress concentration factor. For a sufficiently narrow notch, S_c reaches values of the order of 10^2 to 10^3. According to Griffith the stress may exceed σ_y due to high S_c even if globally the material is subjected to a tension lower than its theoretical strength.

As mentioned before, brittle and ductile materials have different modes of failure. In brittle materials, once σ_y^{max} is exceeded, the cracks propagate at high speed, causing catastrophic damage. Stress increase is proportional to $\sqrt{c}$. Therefore, as the crack grows, S_c increases, causing further damage. The speed of crack propagation is comparable to the speed of sound.

Failure of ductile materials has a different nature. As seen in Fig. 2.2 ductile materials exhibit a relatively large plastic deformation. If the external stress exceeds σ_y but remains lower than σ_u, the material will deform permanently by ε_p. The real value of σ_y is much lower than the one predicted theoretically, because of the presence of dislocations. The type, size and crystalline orientation of a dislocation is characterized by the Burgers vector. The stress necessary to move the dislocations is low with respect to the theoretical one that is necessary to slide perfect crystalline planes with respect to each other.

The origin of strain hardening lies in the dislocation interactions in the plastic regime. The total estimated dislocation length for high quality crystals is in the order of 10^2 to 10^3 cm per cm^3. In general, nondeformed crystals possess 10^6 to 10^7 cm of dislocations per 1 cm^3 [18, 84]. Such a high length significantly influences the behavior of the crystalline material. For a plastic deformation to occur, sufficient energy must be delivered to overcome the internal resistance of dislocations and cause their movement. This energy is

a function of G, of the Burgers vector, of the type of chemical bonds and of the crystal structure [18]. The material becomes strain-hardened when additional stress must be applied.

Strain hardening cannot continue indefinitely. If the stress is higher than σ_u (see Fig. 2.2) internal voids and cracks appear in the structure, local stress increases due to S_c, and the material fails. Therefore, it is beneficial from the point of view of the material's strength to introduce a controlled number of dislocations into crystalline ductile material. Dislocation density may be increased by plastic deformation, by introducing internal interfaces (inclusions), or by decreasing the grain size.

Grain boundaries may be considered as dislocations themselves, thus decreasing grain size increases the dislocation density per unit volume of the material. This effect leads to the so called Hall - Petch behavior [97-98], that describes σ_y as a function of grain size, d:

$$\sigma_y = \sigma_0 + fd^{-1/2} \tag{2.18}$$

where σ_0 is the limit stress level, below which dislocations will not move in the material in the absence of grain boundaries, and f is a material constant. As the grain size decreases, σ_y increases.

This behavior can be explained in more detail by Cottrell's theory [99]. He assumed that the dislocation pile-ups at the grain boundaries are of the same order of magnitude as the grain size. When the stress resulting from the pile-up activates the dislocation sources in adjacent grains, yielding spreads across the grain boundaries. As grains become smaller, dislocation pile-ups are smaller, and higher σ_y is necessary to activate dislocation sources. The Hall - Petch relation is valid for d down to about 20 nm. Below this limit, grains become sufficiently small and the importance of boundary sliding increases, decreasing σ_y (inverse Hall – Petch behavior) [3].

2.4. Nanostructured materials

Nanostructured materials can be defined as those possessing at least one dimension that is smaller than 50 nm [75]. In many cases these structures result in very different properties with respect to the traditional microstructured materials. The control of the material's structure on the nanometer scale can enhance their various mechanical, tribological or optical properties.

Theoretical considerations of creating superhard heterostructures (i.e. materials possessing $H > 40$ GPa and at least two phases) were advanced by Koehler in the early 1970's [71]. The first synthesized heterostructures were based on multilayers of very thin metal films having different elastic constants and a lattice period in the order of several nm [72]. The theoretical strength (and hardness) of such structures is higher than that resulting from the law of mixture [72]. This law states that the hardness of a mixture, H_{ab}, is proportional to the volume fraction of the two materials:

$$H_{ab} = \frac{V_a H_a + V_b H_b}{V_a + V_b} \tag{2.19}$$

where V_a, H_a, V_b and H_b are the volume and hardness values of phases a and b, respectively. Koehler's original ideas were followed by many research groups in the quest for new superhard materials. It resulted in the fabrication and industrial application of superlattices, and later, nanocomposites.

2.4.1. Superlattices

Superlattices are stacks of very thin layers with a well controlled lattice (bilayer) period, Λ, typically in the range from 5 to 50 nm [100-103]. They possess a high interface area density, even up to 10^6 mm^2/mm^3 [72]. Therefore, their structure and properties are governed by the interfacial effects. Fabrication of superlattice structures is a complex procedure. Under equilibrium or near-equilibrium growth conditions, such as thermal

CVD, a layer-by-layer growth mode must be achieved. This implies that the γ_s of materials constituting the superlattice structure should be similar. In this respect, non-equilibrium deposition processes using low temperatures and introducing intense ion bombardment became very attractive, and they allow for a broad choice of materials. They maintain sharp interfaces between the layers that would normally result in island growth and partial mixing of phases.

Control of the superlattice system is achieved by a proper choice of materials, their structure and Λ [72]. The high hardness, exceeding the value predicted by the rule of mixture (see Eq. 2.19), is due to several factors. The most important one, as described by Koehler [71], is the difference of G at the interfaces between the individual layers. Under external stress conditions, dislocation flow across the interfaces is inhibited due to the different dislocation line energies that are related to the difference in G. Another strengthening mechanism is the structure mismatch and lattice mismatch. They result in the coherency strains in the individual layers that produce stress fields inhibiting the dislocation movement [3]. This led to the concept of structural multilayers that consist of the same material, but whose structure is varied by changing the deposition parameters [104]. The layers must be thin (but possessing distinct interfaces) to avoid movement of the dislocations. For larger bilayer periods, usually exceeding 10 nm, the dislocations can operate in individual layers and the standard Hall-Petch relation is obeyed. In such cases, the grain size d in Eq. 2.18 can be replaced by $\Lambda / 2$.

There are several interesting examples of superlattices in which large interfacial strains may stabilize the metastable forms. These include the cubic phase of AlN in AlN / TiN [72] or bcc Cu in Cu / Nb polycrystalline structures [105]. Other examples are: TiN / TiC produced by PECVD [106], TiN / VN by reactive magnetron sputtering [100], Ti / TiN [107-108], and AlN / ZrN and AlN / TiN by tri - cathode magnetron sputtering [109]. Superlattices were successfully applied to the engineering substrates such as cemented carbides [110].

The superlattice structure suffers from a serious disadvantage: for a given system, Λ has a very narrow window of tolerance, of the order of 1 nm, where the maximum hardness occurs. Therefore, superlattices are very sensitive to thickness inhomogeneities, a fact that limits their practical applications. This problem can be overcome by introducing more isotropic systems, such as nanocomposites, that represent the main subject of the present work.

2.4.2. Nanocomposite systems

Nanocomposites are heterogeneous structures that can exhibit superhardness due to the presence of nanometer-size particles embedded in an amorphous or polycrystalline matrix. This can be achieved by a proper choice of materials and an appropriate control of deposition parameters. According to the Hall - Petch relation (Eq. 2.18) superhardness can achieved in hard polycrystalline materials when the grain boundary sliding is inhibited by introducing strong interfaces. This is possible by creating a structure consisting of nanocrystals (nc) that can be embedded in the matrix of another material [111-113].

As a general rule, to synthesize a nc material the two phases must be immiscible. Therefore, the mixed phase, denoted as A_xB_{1-x}, should be thermodynamically unstable and its formation unfavorable from the energetic point of view. This condition can be expressed in terms of the Gibbs free energy, ΔE_g, of mixed phase formation that should yield [111]:

$$\frac{\delta^2 \Delta E_g (A_x B_{1-x})}{\delta x^2} < 0 . \qquad (2.20)$$

This means that any energy fluctuation would lead to spontaneous segregation of phases A and B. The size of the nanocrystals depends on the balance between the decrease of system energy upon separation, the surface energy of interfaces and the nucleation rate

[75]. If the interface energy is small enough, such a system should be stable against Ostwald ripening during nucleation. Ostwald ripening [1] is the diffusion process in which atoms of small clusters diffuse to the bigger ones in order to minimize the cluster's surface energy. The structure of the nanocomposite should be stable up to a temperature that limits the condition expressed by Eq. 2.20.

In his review article, Musil cites numerous examples of hard nanocomposite coating systems [114]:

- metal nitrides in an amorphous nitride matrix; example, TiN, WN, VN in $SiN_{1.3}$ or TiN and Ti_2S in $SiN_{1.3}$.
- metal nitrides and other nitrides; example, TiN and BN;
- metal nitrides in metal matrix; example, ZrN in Cu, AlN in TiAl, CrN in Cu;
- metal nitrides or metal carbides in an amorphous boron matrix; example, Ti-B-C;
- metal carbides in amorphous carbon; example, TiC and WC with in DLC;
- metal carbides in amorphous carbon with amorphous nitride; example, Mo_2C in amorphous C with amorphous Mo_2N.

The choice of the second phase is critical, but not obvious; its properties may change with the volume fraction. Moreover, the second phase may be very difficult to characterize and optimize due to its small amount. Therefore, the nanocomposite behavior and synthesis processes are not yet fully understood and controlled.

The nc-TiN/$SiN_{1.3}$ system was first synthesized by Shizhi et al. [73]. In this case phase segregation led to the creation of TiN nanocrystals embedded in the matrix of amorphous $SiN_{1.3}$ (nc-TiN/$SiN_{1.3}$). More detailed investigations of this material were done by Veprek et al. [74, 111-113] who also reported an extremely high value of H (> 100 GPa) [115]. Although some research groups questioned the numerical value of hardness [116] cited by Veprek, this material possesses very interesting mechanical and tribological properties [117] and a high thermal stability up to about 1000 K [118].

2.4.3. Origin of superhardness in nanocomposites

According to the Cottrell's model of Hall-Petch behavior, the strength of the nanometer size grains, such as TiN, should approach the theoretical value, expressed by Eq. 2.18. This is due to the fact that the dislocations cannot operate in the nanometer size grains because of their small sizes [99]. Therefore, the nanocomposite material can undergo deformation only due to crack formation and growth in the matrix. In the theoretical model proposed by Veprek [112-113] the phenomenon of crack formation and growth is scaled down from the classical fracture mechanics. Fig. 2.7 presents an idealized structure of a nanocomposite subjected to uniaxial stress condition with intergranular crack formation.

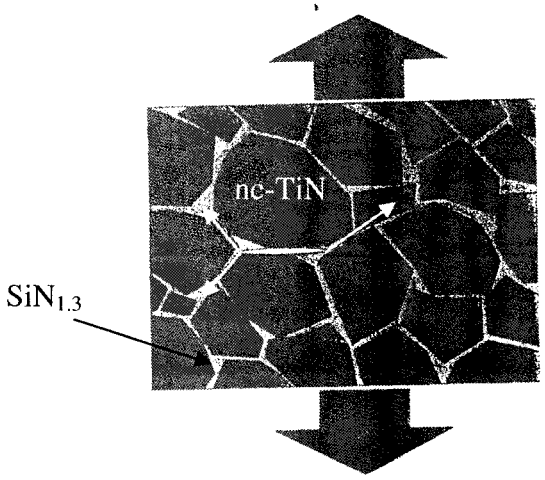

Figure 2.7. *Nanocomposite structure under stress. Crack formation is indicated* [112].

According to Eq. 2.17 S_c is proportional to the crack length, c. Limiting its value would increase σ_y and, therefore, increase the strength of the material. In the nanocomposite structure c is limited by the grain boundaries, i.e. to the size of the grains ~ 10 nm. Assuming the smallest possible l = 0.3 nm, comparable to the interatomic distance, we obtain S_c of about 12. This is a substantial improvement with respect to traditional materials, in which S_c can reach values in the range from 10^2 to 10^3. Moreover, in order

to propagate within the thin amorphous matrix between the nanocrystals, any crack must undergo bending and branching. This decreases the stress component perpendicular to the crack that contributes to its opening. This model of crack propagation underlines the importance of the matrix in nanocomposite materials.

Nanocomposite materials exhibit very pronounced elastic properties. Estimations conducted by Veprek and Argon [112-113] revealed a high value of strain energy density, W_s, representing the energy per unit volume necessary to elastically deform a given system under isothermal conditions. W_s was obtained by measuring the elastic energy and estimating the volume of elastic deformation during depth sensing indentation (DSI) measurements. For nc-TiN/$SiN_{1.3}$, W_s was found to be about $3*10^8$ J/m^3.

For linear elastic isotropic materials W_s depends only on the principal strain values (ε_{xx}, ε_{yy}, and ε_{zz}) and it can be expressed as [81]:

$$W_s = \frac{1}{2} C_{12} (\varepsilon_{xx} + \varepsilon_{yy} + \varepsilon_{zz})^2 + \frac{C_{11} - C_{12}}{2} (\varepsilon_{xx}^2 + \varepsilon_{yy}^2 + \varepsilon_{zz}^2), \qquad (2.21)$$

where the constants C_{11} and C_{12} depend on E and υ (see Eq. 2.2). For comparison, values of W_s for standard engineering materials, such as aluminium (ductile), quartz (brittle), tungsten carbide and diamond (both very hard and relatively brittle) are shown in Table 2.3. These calculations were based on an assumption of hydrostatic stress state ($\sigma_{xx} = \sigma_{yy} = \sigma_{zz}$) and a volumetric strain of 1 %.

Table 2.3. *Elastic strain energy for aluminium, quartz, tungsten carbide and diamond.*

Material	E [GPa]	υ	W_s [10^8 J/m^3]
Aluminium	69	0.345	0.037
Quartz	72	0.170	0.030
Tungsten carbide	527	0.220	0.167
Diamond	1140	0.07	0.333

Given the high values of W_s for the nc-TiN/$SiN_{1.3}$ system, the authors conclude that nanocomposite structures are able to sustain a very high elastic strain of the order of several %. For comparison, the maximum elastic strain for typical hard materials is about 1 % [80-82]. They explain such a high value in terms of the nanocomposite structure: the length of the crack that is formed in the amorphous matrix between the nanoparticles has dimensions in the order of a nanometer. This is only one order of magnitude higher than the length of atomic bonds that can sustain large strains up to 20 % [83]. Therefore, the atomic bonds in the crack head can sustain large elastic strains leading to a high value of W_s.

Both the grain size as well as the intergranular distance must be controlled and optimized to reach superhardness. Various research groups working with different types of materials obtained similar grain size values for optimum mechanical performance. For nc-TiN/$SiN_{1.3}$ Veprek et al. [111, 119-120] found the optimum grain size to be 3 - 10 nm. For nc-ZrN/Cu, and nc-ZrN/Ni Musil et al. [121-122] reported values from about 25 to 35 nm, respectively. Zehnder and Patscheider found an optimum grain size of ~ 5 nm for nc-TiC/a-C:H [123]. Due to the small quantity of the matrix material it is very difficult to measure the intergranular distance. Usually the estimation is based on TEM observations and the chemical composition. The exact value depends on the particular material, for example, in nc-TiN/$SiN_{1.3}$ it is estimated to be about 1 nm (approximately 2 monolayers) [124].

Despite recent progress in the nanostructured systems, there are still many open questions concerning new materials, fabrication techniques and process parameters, especially temperature that often limits the choice of substrates. Optimizing the properties of the matrix material appears of particular importance. New measurement methodologies are, therefore, necessary, in order to correctly evaluate and interpret the enhanced mechanical properties in terms of structure-property relations. This can then help to further optimize such new materials and tailor their characteristics for specific applications, such as hard

coatings for cutting tools, protective and corrosion resistance coatings for machine parts, decorative coatings, tribological films in sliding bearings in MEMS and numerous others.

Chapter 3. Experimental methodology and characterization

This Chapter presents a detailed description of the experimental methodology of fabrication and characterization of hard nanocomposite coatings. It also provides additional information that was not included in the respective experimental sections of the articles. First, we describe the fabrication method, deposition system, and sample preparation. This is followed by a detailed methodology of assessing and interpretation of the mechanical properties. In the third section of this Chapter we present the measurements of optical properties. The last section is devoted to the structural and chemical characterization of the coatings.

3.1. Plasma deposition system and film fabrication

In this work, all films were deposited in RF plasma using a system schematically shown in Fig. 3.1. It consisted of a stainless steel vacuum chamber, 30 cm in diameter, a pumping system with turbomolecular (Varian V 300 ICE) and mechanical (Varian CP 451) pumps equipped for corrosive gases, gas distribution system, RF power supply unit and the heating system. The working pressure, p, was measured by a MKS capacitance gauge and the pumping speed was regulated by a throttling valve (Vacuum General MDV 040). The flow of gases, namely $TiCl_4$, SiH_4, CH_4, N_2, H_2, and Ar was adjusted by MKS and Sierra mass flow controllers in each line. The gas flows and p were monitored by a computer using Labview software. RF power was supplied from an Advanced Energy RFX II 3000 (13.56 MHz) generator through a matching unit (Advanced Energy, ATX 800) that was connected to a substrate holder-electrode 10 or 15 cm in diameter. Substrate bias, V_B, was measured by a voltmeter incorporated in the controller of the matching unit.

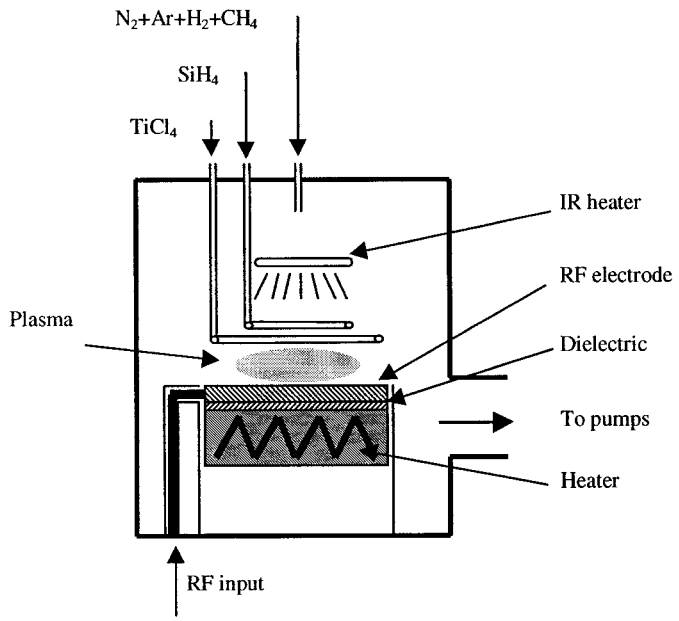

Figure 3.1. *Schematic illustration of the RF PECVD deposition system used for the fabrication of nc coatings.*

The heating system was modified several times during the experimental work. In the initial experiments the substrate holder was inductively heated to a maximum substrate temperature, T_s, of about 300 °C using an ASTEX system. In order to further increase T_s, ordinary halogen lamps of 600 W total power were installed. Given its proven efficiency, an IR heating element (WATLOW) of 1.5 kW power replaced the inductive heating in the second part of the project. It allowed reaching a maximum T_s above 500 °C. Before the deposition, and during the heating stage, T_s was measured directly by a K-type thermocouple touching the surface of the electrode. When steady state temperature was reached the thermocouple was withdrawn and the deposition process was initiated.

The majority of coatings were deposited onto crystalline Si wafers. In order to eliminate surface contaminants, the substrates were cleaned in an ultrasonic bath with propanol. Comparative depositions were also performed using stainless steel and Ti alloy substrates, including parts of a jet engine turbine. To better remove organic contaminants

from the substrate preparation process (cutting, polishing), the substrates were additionally cleaned in acetone prior to their immersion in propanol.

Following numerous preliminary depositions, a "standard" fabrication process has been established; it consisted of the following steps:

a) Before each process the chamber was pumped down to a base pressure of 10^{-5} Torr ($1.33*10^{-3}$ Pa).
b) The substrates were heated for about 1 hour to the desired temperature, controlled by the thermocouple.
c) Before the main deposition process was started the substrates were sputter-cleaned for about 15 min. in a discharge in Ar at p = 50 mTorr (6.66 Pa) and V_B = 600 V.
d) Ar sputtering was followed by surface pretreatment described in the respective articles.
e) The coating process lasted for 1 to 3 hours.
f) After deposition the system was allowed to cool down for about 3 hours.
g) Following the safety regulations the SiH_4 and $TiCl_4$ gas lines were purged with N_2 after each deposition cycle.

3.2. Mechanical properties

In every practical application of thin films and coatings their mechanical properties are of crucial importance [1]. The film has to adhere to the substrate, be resistant to static or dynamic mechanical contact and should withstand the effects of the working environment. These concepts are very general and they apply to different situations, ranging from hard coatings on cutting tools [3] to optical coatings on plastic substrates [16], or microsystems, such as MEMS [125]. The methodology of mechanical characterization is one of the main subjects of this thesis and it is systematically covered in the following sections.

3.2.1. Hardness

Hardness, H, is traditionally defined as resistance of a material to plastic deformation [3]. Therefore, H is directly related to σ_y in compression and depends on the strength of interatomic bonds and on the deformation mechanism that is determined by the structure of the material [83]. Materials possessing high intrinsic H are characterized by a high cohesive energy and short bond length (Fig. 2.5). H measurements are the practical way of estimating σ_y in compression when it is impossible to apply the tensile tests explained in Chapter 2 and presented schematically in Fig. 2.2. H can be associated with σ_y through the following relation:

$$H = g\delta_y \tag{3.1}$$

where g is a material-dependent constant, for metals $g \sim 3$ [126]. However, for materials possessing high values of H, such as nanocomposites, this relation is more complex and also depends on E and υ [83].

H can be measured in different ways. One way is scratching a softer material with a harder one. Scratch hardness is widely used in geology for the evaluation of minerals. It is based on the Mohs scale [84] that classifies materials from the hardest one (diamond, 10 on the Mohs scale) down to the softest one (talc, 0 on the Mohs scale). Scratch hardness is not very practical and another type of hardness, namely indentation hardness, has been widely adopted in metallurgy. H is measured by indenting an investigated material with a spherical, conical, or pyramidal indenter with loads that create permanent plastic deformation.

Numerically, H expresses the applied pressure on the surface, leading to a permanent deformation (measured in GPa, or in the engineering literature, in kg / mm^2). H is defined as:

$$H = \frac{L}{A_{in}}, \tag{3.2}$$

where L is the load applied to the indenter, and the contact area, A_{in}, is evaluated from the surface of an indent. Depending on the investigated material, or simply for historical reasons, there are several types of indenters: Brinell (10 mm steel ball), Vickers (diamond pyramid with an angle of 136° between the faces), Rockwell C (diamond cone with an angle of 120°), Rockwell B (1.59 mm steel ball), Knoop (diamond rhombic – based pyramid with edge angles of 172.5° and 130°) and Berkovich (three sided pyramid with a nominal angle of 65.3° between the face and normal to the base).

Indentation measurements are not trivial. High pressures created at the tip of the indenter lead to a complex stress distribution and a complicated deformation mechanism [127]. The latter depends on many factors: structure, temperature, geometry of the indenter, and L. The range of L in H measurements is schematically illustrated in Fig. 3.2.

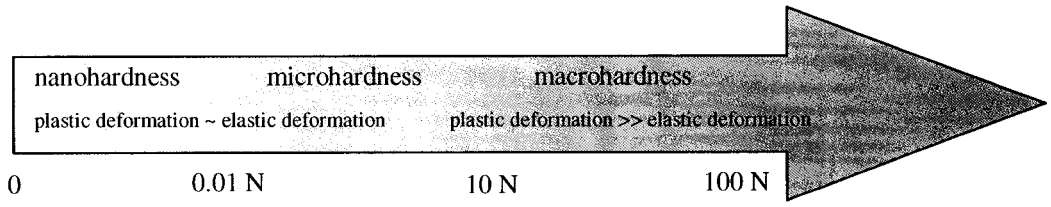

Figure 3.2. *Load range in the measurements of hardness.*

For high L, plastic deformation is substantially higher than the elastic one and the measured H is constant with respect to L. Small L must be applied in H measurements of thin films, in order to eliminate the influence of the substrate. The zone of plastic deformation beneath the indenter should not exceed the thickness of the film. Therefore, the maximum "allowed" penetration depth, h, depends on the mechanical properties of the film. As a "rule of thumb" 5 – 10 % of the film thickness is usually considered a maximum value of h. In the micro- and nanohardness regime indents are very small, elastic deformation become significant, and it may even exceed the permanent plastic one. This effect may lead to an increase of the apparent H value. The dependence of H on the indentation size, s, is generally known as the Indentation Size Effect (ISE) [128]:

$$H = qs^{M-2}, \tag{3.3}$$

where q is a constant value of H at unit indentation size, and M is the Meyer index describing the properties of the material. For most metals and ceramic materials $1.6 < M < 1.9$, and H increases with decreasing s (and hence L) [129]. For $M = 2$, H is independent of s, for $M > 2$, H decreases for decreasing s. The constants q and M are usually found by mathematical fitting of the experimental data points. Special care should be taken when measuring small indents by optical microscopy. Large discrepancies in H values were found when compared with scanning electron microscopy (SEM) measurements [50].

In the case of deep indents, for which $h > 10$ % of the coating thickness, several mathematical models can be applied to eliminate the influence of the substrate and to correctly evaluate H. They are described in Chapter 4.

Recently, DSI measurements of H have become popular. It allows one to apply low loads down to several μN and to measure H from very shallow indentations below 100 nm. In DSI, H is calculated from the load-displacement curve, namely the relation between L and h [130]. In addition, this technique also allows one to determine E and to evaluate the elasto-plastic behavior of the material. An example of surface deformation during indentation and the resulting $L(h)$ curve for an elasto-plastic material with work hardening (exhibiting permanent plastic deformation, h_f) are shown in Fig. 3.3.

The $L(h)$ curve is a "nanomechanical fingerprint" of any material. H is calculated from Eq. 3.2, where A_{in} represents the tip area function that defines the projected area of the contact between the film surface and the tip under load. Special attention has to be paid to a correct evaluation of A_{in} as a function of the so called corrected penetration depth, h_c. h_c is used to describe the deformation of the surface under load (see Fig. 3.3a), and can be expressed as:

$$h_c = h_{\max} - 0.72 L_{\max} \left(\frac{dL}{dh} \right)^{-1}, \tag{3.4}$$

where h_{max} is the maximum penetration depth, L_{max} is the maximum value of L, and $\frac{dL}{dh} = S_{in}$, represents the tangent to the unloading curve at the maximum load and it defines the stiffness, S_{in}. The factor 0.72 for the Berkovich indenter corrects for h_s that represents the depression of the surface around the indentation (see Fig. 3.3a).

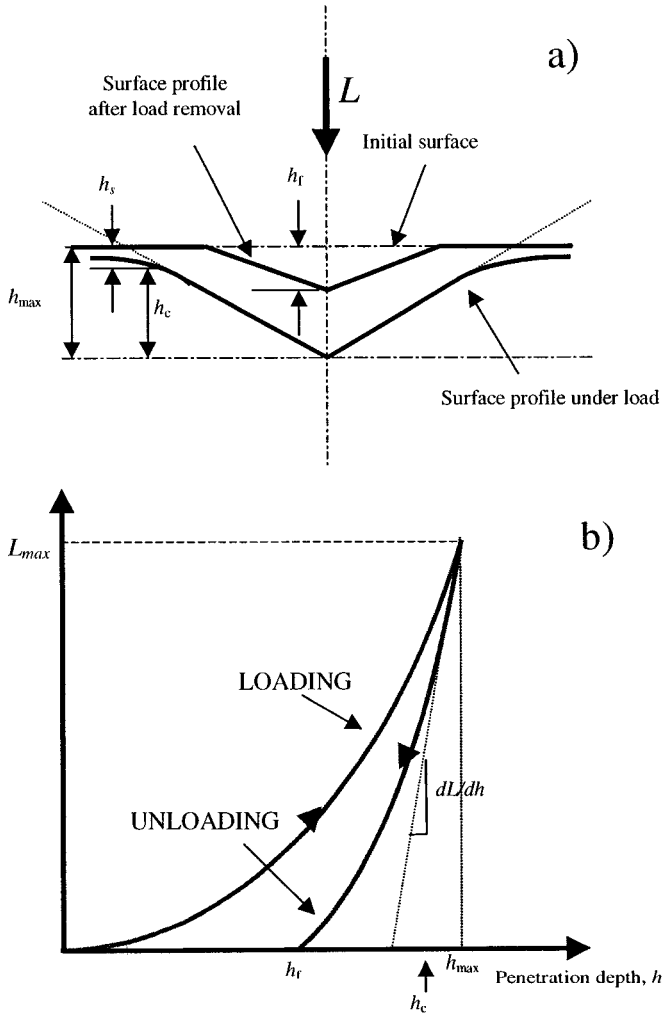

Figure 3.3. *Surface deformation during indentation (a) and the corresponding load displacement curve (b)* [130].

For an ideal Berkovich indenter $A_{in} = 24.5h_c^2$. However, the geometry of a real indenter is not ideal and it changes during usage. A comparison between a brand new and a one year old Berkovich indenter is shown in Fig. 3.4. It is obvious that A_{in} must be corrected for these geometrical changes. The actual value of A_{in} can be approximated by the fifth order polynomial of the form [130]: $A_{in} = 24.5h_c^2 + C_1h_c + C_2h_c^{1/2} + ... + C_5h_c^{1/16}$. The constants C_1 through C_5 are found from the measurements of a standard material with a known value of E. In our case the reference material was fused silica with E = 72 GPa. An underestimation of A_{in} due to blunt (worn) indenters may lead to incorrect high values of H.

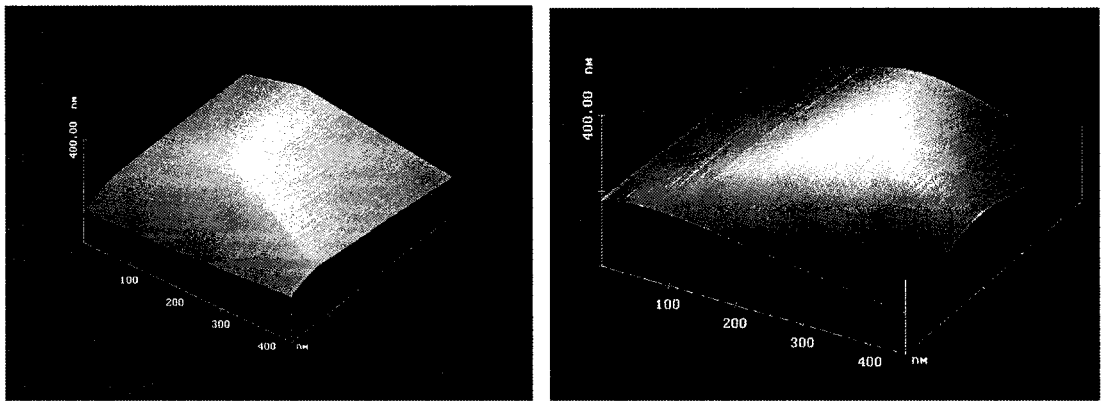

Figure 3.4. *Brand new (a) and one year old Berkovich tip (b).*

3.2.2. Young's modulus.

Another very important mechanical property is Young's modulus, E. It is defined by Hooke's law and can be determined from the slope of the $\sigma(\varepsilon)$ dependence in the elastic regime as described by Eq. 2.4 and indicated in Fig. 2.2. Following Eq. 2.8, we can write:

$$E \sim \left.\frac{dF(r)}{dr}\right|_{r_0} = \left.\frac{d^2U(r)}{dr^2}\right|_{r_0} \tag{3.5}$$

We observe that high values of E result from the deep energetic minima described by high curvatures of $U(r_0)$ and small interatomic distances (equilibrium positions, r_0). As

mentioned above, E can be measured by a tensile test. However, this method is not suitable for thin films, for which two techniques are frequently applied, namely the surface acoustic wave (SAW) propagation [131], and nanoindentation [130] methods.

In nanoindentation the value of E is obtained from the unloading part of the $L(h)$ dependence shown in Fig. 3.3b. Elastic behavior of a measured specimen is combined with the elasticity of the load frame of the nanoindenter and is modeled in terms of compliance. The compliance defines the relation between the stress and strain. In its general form it is the inverse of the elastic stiffness matrix in Eq. 2.1. Treating the sample-indenter system in one dimensional approximation we can write:

$$C_s + C_f = \left(\frac{dL}{dh}\right)^{-1}, \tag{3.6}$$

where C_s is the sample and C_f is the load frame compliance. C_f is specific for a given load frame combination and it is measured during the calibration procedure. C_s is expressed as:

$$C_s = \frac{1}{2E_r}\left(\frac{\pi}{A_{in}}\right)^{0.5}, \tag{3.7}$$

where E_r is the sample's reduced Young's modulus defined as:

$$\frac{1}{E_r} = \left(\frac{1-\upsilon^2}{E}\right) + \left(\frac{1-\upsilon_i^2}{E_i}\right), \tag{3.8}$$

where the subscript i represents the indenter (for diamond indenters, υ_i = 0.07, and E_i = 1140 GPa). Therefore, combining Eqs. 3.6 – 3.8, and knowing A_{in}, it is possible to calculate E_r. In the calibration procedure with a standard of a known value of E_r it is possible to determine A_{in} from the $L(h)$ relations at different h values.

Other elasto-plastic characteristics can also be obtained from the $L(h)$ relation. This particularly applies to the elastic rebound, R_{el}, defined as the ratio of the energy of elastic deformation, W_e, to the total work of indentation, W_{tot}. W_e is defined as the area under the unloading curve, and W_{tot} corresponds to the area under the loading curve (see Fig. 3.3b).

A material's resistance to plastic deformation is expressed as the H^3/E^2 ratio [132-133]. In the case when the value of H is high and that of E is small, the plastic deformation is also small, since the load is distributed over the larger area and the stress distribution is uniform.

R_{el} and H^3/E^2 are related to W_s defined by Eq. 2.21. As it was explained in Chapter 2, a high value of W_s means that a given material is able to accommodate large elastic strain. This property of the stress-strain relation (see Fig. 2.2) corresponds to a large area under the linear part of the $\sigma(\varepsilon)$ curve. In order to obtain a high value of W_s, σ_y should also be high but E relatively small. This fact gives rise to high values of R_{el} and H^3/E^2 since H is proportional to σ_y.

H and E were obtained by DSI using a Triboindenter (Hysitron Inc.), equipped with a Berkovich pyramidal tip, using loads from 1 to 10 mN, and in compliance with the international standards [134].

3.2.3. Mechanical stress

Control of the total mechanical stress, σ_{tot}, is very important from the point of view of practical applications [1, 3]. The σ_{tot} is the sum of the thermal stress, σ_{th}, and the intrinsic stress, σ_{in}. σ_{th} results from the difference in the coefficients of thermal expansion (CTE) between the coating and the substrate due to cooling down the coating-substrate system after the deposition process or by temperature changes under the operation conditions [1, 3]. σ_{in} is determined by the internal structure of the material, in particular structural defects like macroscopic voids, gas entrapment or phase transformation [1, 3, 135-136]. Usually, low values of σ_{tot} in compression are advantageous since they inhibit propagation of cracks. High values of σ_{tot} can add to applied external loads and lead to

delamination or cracking. σ_{tot} may be balanced or set at a desired level by a simultaneous control of σ_{th} and σ_{in}.

The coating - substrate system under stress condition is schematically presented in Fig. 3.5. In order for the system to be in equilibrium, σ_{tot} in the coating gives rise to a bending moment in the substrate. Since the substrate is much thicker than the film, σ_{tot} in the substrate is much lower. As illustrated in Fig. 3.5 there exists a stress discontinuity at the coating/substrate interface. If the interface forces exceed the forces of adhesion, the coating delaminates.

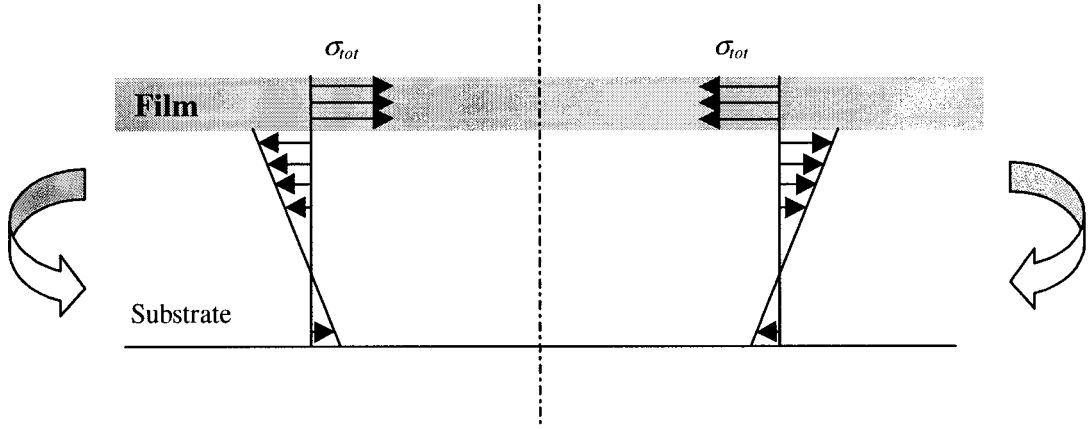

Figure 3.5. *The coating – substrate system under the stress condition.*

In this work σ_{tot} was obtained by measuring the curvature of the c-Si substrate before and after deposition; this was then substituted into the Stoney formula [1]. The curvature was measured by Dektak II profilometer and a Tencor FLX 2900 thin film stress measurement system. In order to avoid complex flat plate bending problems, samples for stress measurements were formed by long c-Si strips approximately 30 mm long, 5 mm wide and 0.5 mm thick. This allowed us to assume the coated samples to be beams in pure bending. During the coating process samples for stress measurements were free standing. Any form of attachement to the substrate-holder was found to introduce additional strains that can lead to inconsistent measurements of σ_{tot}. The measurement

precision is related to the thickness uniformity of the coating and the measurement of the substrate's curvature. In general, the spread in the data was in the range of 15 to 20 %.

3.2.4. Toughness

Toughness is a mechanical property that characterizes the resistance of a material to crack propagation. In elastically isotropic body subjected to σ, the accumulated W_s may be released by crack formation. The energetic condition of crack propagation is that the total energy of the strained system should decrease upon the crack opening. The energy balance between W_s and the surface energy of the open crack based on the Griffith's analysis of fracture mechanics yields the stress, σ, necessary to propagate a crack. For a crack of length $2c$, σ is expressed in its general form as [1]:

$$\sigma = \sqrt{\frac{4\gamma_s E}{\pi c}}. \tag{3.9}$$

The term:

$$K = \sqrt{4\gamma_s E}, \tag{3.10}$$

is called the critical stress intensity factor, and it represents the toughness of a material. The higher the value of K, the higher the stress necessary to propagate a crack. This intrinsic property of the material is very important from the point of view of practical applications. One should note the similarity between the Eqs. 3.9 and 2.9, representing σ_y for a brittle material. In fact, the theoretical value of σ_y for brittle materials is limited by the crack opening and propagation.

The parameter K of the films was determined from indentations using $L \sim 2$ N. An example of an indentation is presented in Article 1, Fig. 4.5. The relation between K and the resulting crack length, c, is [2]:

$$K = B_{in}\left(\frac{E}{H}\right)^{0.5}\left(\frac{L}{c^{1.5}}\right), \tag{3.11}$$

where B_{ind} is the indenter-dependent constant ($B_{in} = 0.016$ for the Vicker's indenter).

3.2.5. Wear

Wear can be defined as the removal of material from solid surfaces as a result of a dynamic contact [4, 137]. This can be described by several wear mechanisms: adhesive, abrasive and asperity deformation, fatigue and delamination, and chemical. They are schematically shown in Fig. 3.6. Under real contact conditions, several wear mechanisms are usually combined. Wear mechanisms depend on the surface morphology and the materials in contact. They can be determined by a detailed microstructural analysis of the wear track.

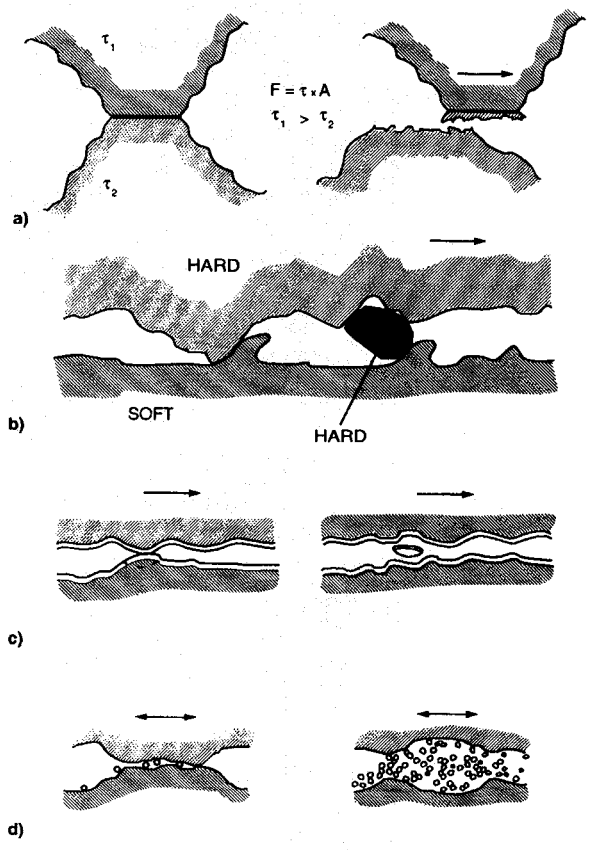

Figure 3.6. *Wear mechanism: adhesive (a), abrasive (b), fatigue (c), chemical (d)* [4].

Wear and the friction coefficient, μ, are not the material's intrinsic properties but the response of the solid surfaces in dynamic contact. Usually, low value of μ corresponds to a low wear and high value of μ to a high wear. However, this general relation is not always valid. For example, interfaces with solid lubricants and polymers exhibit relatively low μ and a high wear, while ceramic materials are characterized by high μ and low wear. The change of μ within one order of magnitude can induce a change of wear by several orders of magnitude.

The wear rate, W_r, is a quantitative parameter describing wear, and allows a comparison of different materials. W_r is defined as:

$$W_r = \frac{V}{Ls_t}, \tag{3.12}$$

where V is the volume of the removed material, s_t is the moved distance. W_r represents the energy, Ls_t (i.e. the input work, because L is directly proportional to the friction force), necessary to remove a certain volume, V.

Wear and friction, μ, characterize the tribological behavior of materials. The wear rate, W_r, was measured using Triboindenter with Berkovich tip on 3 μm x 3μm surface scanned with frequency of 3 Hz and L = 100 μN. μ was tested with Microscratch-tester (MST, CSEM, Neuchatel) at L = 1 N, using a Rockwell C hemispherical diamond tip of 200 μm radius.

3.3. Optical properties

The optical properties are important in the area of hard and protective films applied as decorative coatings. Quantitative evaluation of optical properties, such as reflectance, dispersion relations and color gives also insight into the electronic structure of the materials. The purpose of this section is to give a brief background to the evaluation of optical properties investigated in this work.

3.3.1. Dispersion relations

Basic optical properties of a material are described by the complex refractive index, N, defined as [1]:

$$N = n - ik, \tag{3.13}$$

where n is the refractive index and k is the extinction coefficient. Alternatively, Eq. 3.13 can be expressed in terms of the complex dielectric constant (complex permittivity), $\bar{\varepsilon}$:

$$\bar{\varepsilon} = \varepsilon_1 + i\varepsilon_2 = N^2 \tag{3.14}$$

Both N and $\bar{\varepsilon}$ depend on the wavelength (or energy) of the electromagnetic wave, expressed by the dispersive relations characteristic of the electronic structure of the investigated materials. In the present work the most suitable relations were found to be the Lorentz and Drude approaches. The Lorentz model describes the absorption due to direct interband electronic transitions while the Drude model deals with intraband transitions of free electrons.

The Lorentz model is based on an assumption that the electronic cloud surrounding the atomic nucleus is polarized by the external electromagnetic field. Using the simple oscillator approach it is possible to approximate the dielectric constant $\bar{\varepsilon}$ as [138]:

$$\begin{aligned} \mathrm{Re}(\bar{\varepsilon}) &= \varepsilon_1 = n^2 - k^2 = 1 + \frac{N_{el}e^2}{\varepsilon_0 m} \frac{(\omega_0^2 - \omega^2)}{(\omega_0^2 - \omega^2)^2 + \Gamma^2\omega^2} \\ \mathrm{Im}(\bar{\varepsilon}) &= \varepsilon_2 = 2nk = \frac{N_{el}e^2}{\varepsilon_0 m} \frac{\Gamma\omega}{(\omega_0^2 - \omega^2)^2 + \Gamma^2\omega^2} \end{aligned} \tag{3.15}$$

where ω is the frequency of the electromagnetic wave, ω_0 the resonance frequency of an oscillator, Γ the damping term, N_{el} the electron density, ε_0 is the dielectric constant of vacuum, and m the electron mass. A typical variation of ε_1 and ε_2 for a weakly-damped oscillator is shown in Fig. 3.7.

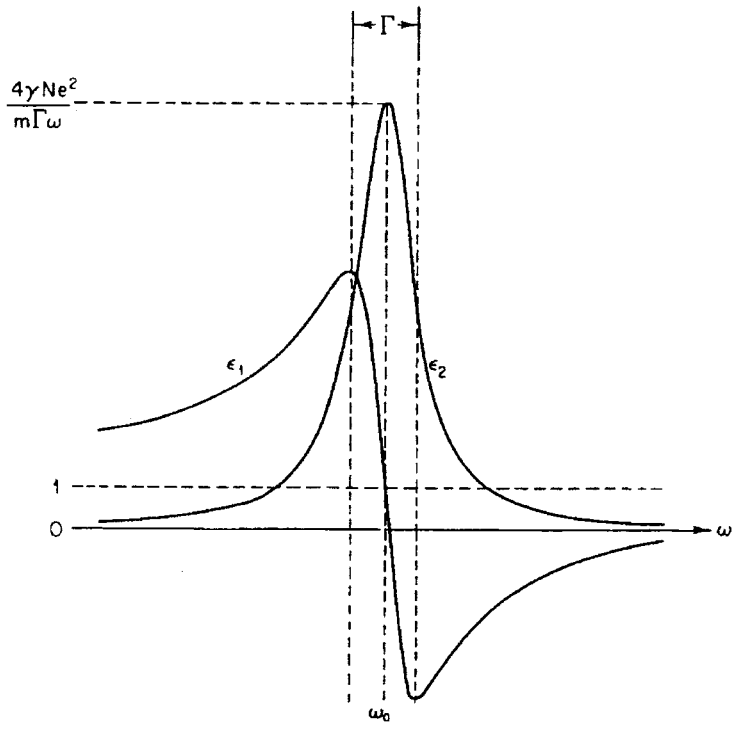

Figure 3.7. *Lorentz oscillator* [138].

$\bar{\varepsilon}$ is characteristic for a given material and it defines its optical behavior from which other optical properties can be derived. For example, plotting dispersion relations, described by Eq. 3.15 as a function of $\hbar\omega$, we can obtain the response of material in terms of reflectance, R_s (see Fig. 3.8). One can conclude that the material approximated by one Lorentz oscillator is transparent in region I (T), absorbing in region II (A), reflecting in region III (R), and again transparent in region IV (T).

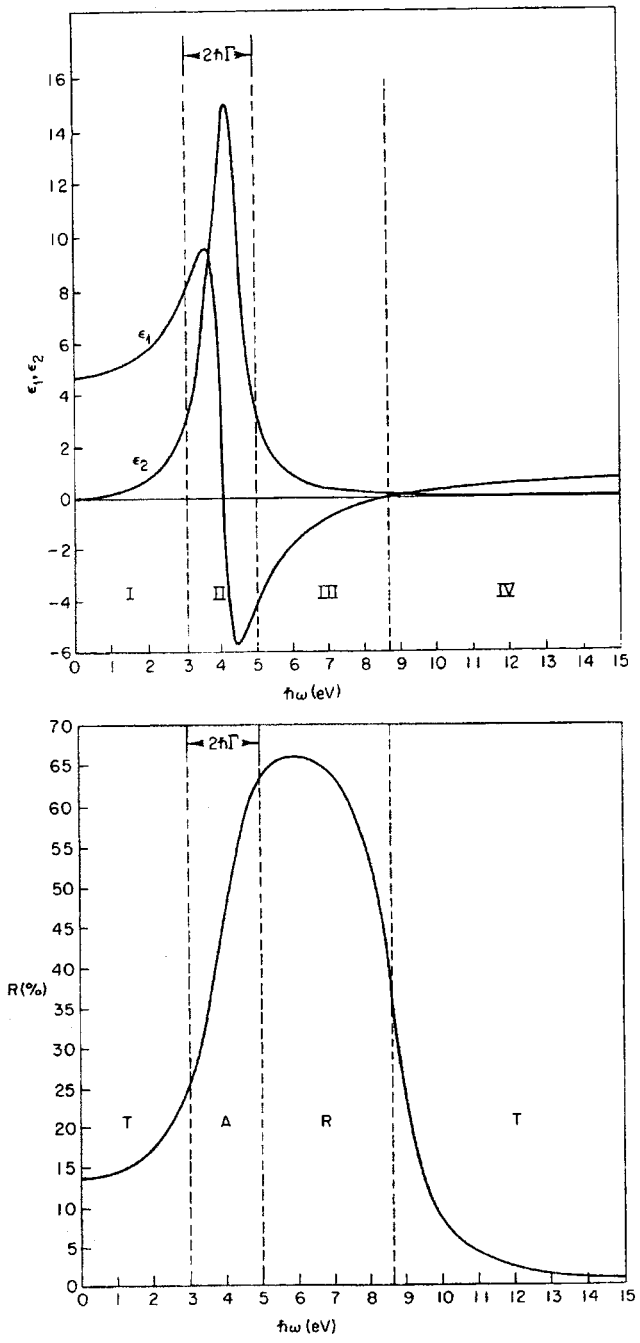

Figure 3.8. *Dispersion relation for ε_1 and ε_2 (a) and the resulting reflectance (b)* [138].

The Drude model is suitable for characterizing metals and it is based on a similar approach. Optical properties of metals are governed by the free electron gas. They are

modeled by setting the frequency of the Lorentz oscillator to zero. It means that the free electron gas in metals absorbs low frequency electromagnetic radiation in the infrared region. Eq. 3.15 then yields:

$$\varepsilon_1 = 1 - \frac{N_{el}e^2}{\varepsilon_0 m}\frac{1}{(\omega^2 + \Gamma^2)}$$
$$\varepsilon_2 = \frac{N_{el}e^2}{\varepsilon_0 m}\frac{\Gamma}{\omega(\omega^2 + \Gamma^2)} \tag{3.16}$$

As indicated in Fig. 3.8, the properties of metals coincide with regions III and IV, i.e. they are reflecting in the infrared and transparent in the UV. The onset of region IV is defined by $\varepsilon_1 = 0$. The frequency of electromagnetic wave at which $\varepsilon_1 = 0$ is called the plasma frequency and is expressed as [138]:

$$\omega_p = \sqrt{\frac{N_{el}e^2}{\varepsilon_0 m}}, \tag{3.17}$$

where N_{el} for metals is equal to the free electron density, n_e. For frequencies above ω_p, R_s of metallic materials drops dramatically. We will see below that modeling the material's optical behavior in terms of combined Lorentz and Drude approaches and R_s measurements allows one to evaluate transition from the metallic to dielectric properties, a particular characteristic of nc materials.

3.3.2. Colors

Color may be defined as "a sensation produced in the brain in response to light received by the retina of the eye" [139]. Therefore, color perception is a complex psycho-physiological phenomenon. The human eye possesses four types of receptors: rods and three kinds of cones. Rods are responsible for the perception of light intensity only, and, therefore, for black and white vision. The cones are responsible for color vision.

Perceived color may have up to five different characteristics. However, for simplicity, only three color attributes are considered here. They are hue, saturation and brightness

[139]. Hue is the sensation perceived by an observer in response to a particular stimulus, for example red or blue light. The human eye can normally distinguish about 200 hues. Colors that possess a hue are called chromatic colors in contrary to achromatic ones that are perceived while looking at white, neutral gray or black. Saturation is a measure of hue concentration. For example, comparing red and pink, we can distinguish them by saturation, i.e. by the proportions of chromatic (hue) and achromatic components. Red has a higher concentration of hue than pink, therefore, it has a higher saturation. Colors produced by monochromatic light possess 100 % saturation. The third color attribute is brightness, defined as the illumination in which an object is viewed.

A color that can be reproduced by three primary colors is said to be within the gamut of these colors. However, not every real color can be reproduced by a mixture of three real colors. Therefore, it was necessary to introduce a concept of imaginary colors. This concept is very useful because it allows one to reproduce every real color. The visual response of a typical viewer in terms of imaginary colors is defined as CIE (Commission Internationale d'Eclairage) 1931 standard observer [140-141]. It describes in which proportion the three imaginary primary colors (red (R), green (G) and blue (B)) have to be mixed to match the color of one watt of radiant power at a given wavelength. The so called color mixture functions are presented in Fig. 3.9.

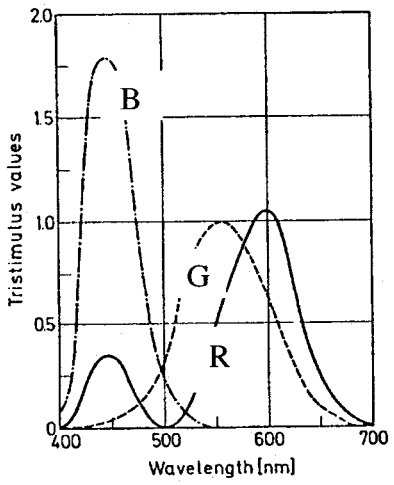

Figure 3.9. *Color mixture functions* [139].

In order to facilitate the description, the color mixtures are normalized to 1 and presented in the *xy* coordinate system (see Fig. 3.10). The real colors that may be perceived by the human eye are situated within the tongue-shaped area on the chromacity diagram, defined as the spectrum locus. The colors situated on the spectrum locus are produced by monochromatic light and they all possess 100 % saturation. Colors outside of the spectrum locus are imaginary and are ignored. The color saturation decreases as the color gets closer to point E, which indicates zero saturation, that is the color white. There are other color systems, for example the L*a*b* system that is presented in Chapter 5.

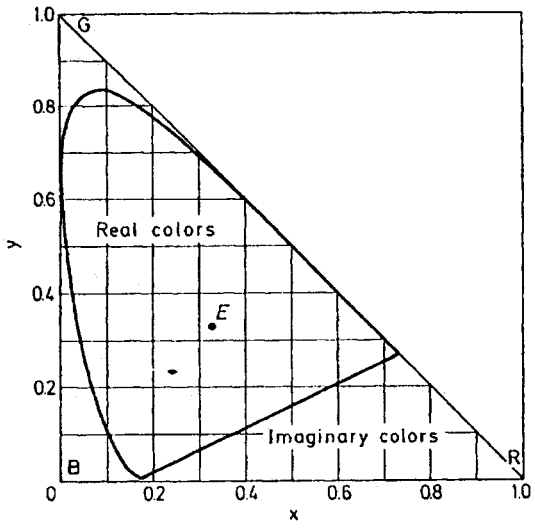

Figure 3.10. *CIE (1931) chromacity diagram* [139].

3.3.3. Optical measurements

The optical measurements of nanostructured films is part of the multitechnique characterization approach applied throughout this work. The complex dielectric constant $\bar{\varepsilon}$, in the visible (VIS) and near infrared ranges (NIR) was obtained by variable angle spectroscopic ellipsometry (VASE J.A. Woollam Co.). The measured range was between 280 and 1600 nm (4.41 and 0.77 eV), using angles of incidence between 55° and 75°. The

ellipsometric models were fitted to the experimental spectra using the same mathematical algorithms as in IR VASE and described in Chapter 5. R_s was measured using a Perkin–Elmer Lambda 19 spectrophotometer in the specular mode at near normal incidence. R_s spectra were then used to evaluate ω_p and the colors. A detailed description of the color measurement methodology is given in Chapter 5.

3.4. Structure and chemical composition of the films

Different complementary characterization techniques were employed in order to obtain detailed information about the microstructure and composition of the films. All these techniques were available in the characterization facilities of the "Group de recherche en physique et technologie des couches minces (GCM)" and the "Centre du caractérisation microscopique de matériaux (CM^2)" on the Campus of the Université de Montréal.

3.4.1. Microstructure

The morphology of coatings was determined by scanning electron microscopy (SEM) using a Philips XL 20 apparatus. SEM observations were performed on the cleaved cross sections of coated Si wafers. In order to avoid charge accumulation, samples were additionally metallized by sputtering using an Au target.

The transmission electron microscopy (TEM, Philips CM 30) was employed to confirm the nanocomposite nature of the coatings and to measure the size of nanoparticles and their distribution. Observations were made in bright and dark fields. The electron diffraction patterns gave the information concerning the crystallographic structure of the nanoparticles. The observations were done with magnifications ranging from 128 to 550,000, and using a voltage of 300 keV. Samples for TEM were prepared by mechanical polishing and intense Ar broad ion beam milling (Gatan 691). Alternatively, focused ion beam (FIB, Hitachi FB 2000A) milling was performed with Ga ions with an energy

varying from 10 to 30 keV. This technique allows for monitoring the milling process and it offers a significantly higher precision.

X-ray diffraction (XRD) was used to identify the crystalline phases, determine lattice parameters, and to estimate average crystal sizes (complementary to direct TEM observations). In order to avoid the substrate influence, the scans were done at a grazing angle of 0.2 – 0.5° from the surface plane with a step of 0.02°. Measurements were performed using a Philips X'pert system equipped with a Cu-K_α X-ray source.

Surface morphology was investigated by atomic force microscopy (AFM) using the Digital Instruments Nanoscope E system. The scanned surface of 1 μm x 1 μm or 10 μm x 10 μm was imaged in the contact mode. Surface roughness was expressed in terms of R_a, the arithmetic mean value of the deviation in height from the profile mean value y(x), defined as:

$$R_a = s_t \int_0^{s_t} |y(x)| dx \tag{3.18}$$

where s_t is the lateral distance.

3.4.2. Chemical composition

Several complementary techniques were used in order to determine the chemical composition of the films. Compositional depth profiles were determined by elastic recoil detection in the time-of-flight regime (ERD-TOF) [142]. This technique allows one to establish the quantitative chemical composition without standards. Moreover, ERD can quantify the H concentration, that is of primary importance for PECVD films frequently fabricated in a hydrogen-rich environment. In the experimental setup around a 6 MV tandem accelerator, the investigated samples were bombarded by heavy ions of Cl, Si, and Cu with equal incidence and recoil angles of 15°, leading to a scattering angle of 30°. These ions eject atoms from the sample (forward recoil) towards the detector. Their time

of flight is measured between the thin carbon foil, generating the first timing signal, and the cooled silicon surface barrier detector, measuring their energy and generating the second timing signal. This combination allowed for the determination of the mass of particles ejected from the sample. The H content was determined by another silicon surface barrier detector covered with a foil blocking other atoms. Mass-separated spectra as a function of energy were converted into the compositional depth profiles by in-house computer software.

Auger electron spectroscopy (AES, JEOL JAMP-10S) was used to evaluate the N, Si and Ti concentrations in the nc-TiN/$SiN_{1.3}$. Surface contaminants were removed by mild Ar sputtering. The deconvolution of the principal peak of N ($KL_{23}L_{23}$) and the secondary peak of Ti ($L_3M_{23}M_{23}$) was performed using the approaches proposed in literature [143-144].

XPS analysis was performed in a VG ESCALAB 3 Mark II instrument with a resolution of 0.7 eV using a non-monochromated MgK_α source (1256.7 eV). Mild Ar ion sputtering was used to partially remove oxygen and hydrocarbons from the surface. Low energy ion bombardment was applied in order to avoid preferential sputtering. As a result, oxygen and carbon were not completely removed. However, combining XPS with ERD depth profiles allowed for reliable quantitative measurements of chemical composition and identification of chemical bonds between the elements present in the coatings.

The dielectric $SiN_{1.3}$ and SiCN coatings were also examined by infrared variable angle spectroscopic ellipsometry (IR VASE, J.A. Woollam Co.). This technique allows one to qualitatively determine the chemical structure in a way similar to Furrier transform infrared spectroscopy (FTIR). IR VASE measurements were also used to determine the film thickness. The latter were generally found to be identical to the values obtained by visible (VIS) VASE and directly observed by SEM. This result serves as a confirmation of the validity of the optical models of dielectric films.

Complementary measurements were performed by Microraman spectroscopy. Raman scattering spectra were obtained using a Renishaw RM 2000 Raman microscope in the Stokes scattering mode using an Ar laser (λ = 514.5 nm). A detailed description of the experimental setup is given in Chapter 5.

Chapter 4. Article 1: Relationship Between the Mechanical Properties and the Microstructure of Nanocomposite TiN/$SiN_{1.3}$ Coatings Prepared by Low Temperature Plasma Enhanced Chemical Vapor Deposition

The first article is devoted to the fabrication of nc-TiN/$SiN_{1.3}$ coatings at low T_s and to a systematic characterization of their mechanical properties and structure. Even if the nc-TiN/$SiN_{1.3}$ is not completely new in the area of nc coatings, its study was motivated by the following two principal reasons:

a) To demonstrate the possibility to fabricate nc structures at a low temperature of 300 °C and to compare the resulting structure and mechanical properties with those obtained by a high temperature process. Low T_s is important since it allows one to coat a wider range of substrate materials. It also decreases the thermal stress, σ_{th}, an effect leading to improved adhesion.

b) To establish the mechanical testing methodology, so important for testing superhard coatings. This was necessary in order to respond to some controversies in this area. In fact, we showed that both depth sensing indentation (DSI) and static indentation (SI) approaches yield consistently very similar results if the data analysis is performed correctly. Different mathematical models are applied, that allows one to estimate the substrate influence. The ISE effect was also taken into consideration.

Relationship Between the Mechanical Properties and the Microstructure of Nanocomposite TiN/$SiN_{1.3}$ Coatings Prepared by Low Temperature Plasma Enhanced Chemical Vapor Deposition

P. Jedrzejowski, J.E. Klemberg-Sapieha and L. Martinu

Groupe des couches minces GCM and Department of Engineering Physics, Ecole Polytechnique, Montreal, Quebec, H3C 3A7 Canada

Published in: Thin Solid Films **426** (2003) 150-159

Keywords: PECVD, nanocomposites, mechanical properties

4.1. Abstract

Nanocomposite hard coatings were fabricated by PECVD from $TiCl_4/SiH_4/N_2/H_2$/Ar gas mixtures at substrate temperatures of 300 °C and 500 °C. The mechanical characteristics such as micro- and nanohardness, Young's modulus, toughness and stress were evaluated, respectively, by depth-sensing and classical indentations, and by curvature method. The mechanical and tribological properties are systematically correlated with the film microstructure and composition determined by XRD, SEM, ERD-TOF, XPS, and AFM. For optimized nanocomposite films consisting of about 8 nm size TiN grains incorporated in an amorphous $SiN_{1.3}$ matrix, we found reduced Young's modulus > 270 GPa and > 350 GPa, hardness > 25 GPa and > 40 GPa, and compressive stresses ~ 1.0 GPa and ~ 2.5 GPa for low and high deposition temperatures, respectively. The effect of microstructure on the mechanical characteristics is discussed and the methodology of hardness measurements, in particular, the correlation between the depth-sensing indentation and the indentation size effect are addressed in detail.

4.2. Introduction

During the last decade we have witnessed a rapid advancement in the field of hard and protective coatings. This trend has been stimulated by the development of new fabrication techniques, advanced process control, modern vacuum technology, and, finally, by a significant progress in the characterization techniques of thin films. Hard coatings with tailored functional properties are increasingly important for applications in many different areas of engineering and industry [1]; this includes coatings for cutting tools for dry and high speed machining, protective coatings for turbine blades and machine parts, diffusion barriers for electronics, hard coatings for infrared optics, anticorrosion and decorative coatings, and films for micro-electromechanical systems (MEMS).

Important practical limitations of hard coatings are the temperature of deposition, accumulation of stress, and inherent adhesion problems. Stress related to adhesion results from a difference in the thermal expansion coefficients between the coating and the substrate, difference in the lattice parameters, gas entrapment etc. [1, 4, 24]. Low temperature deposition techniques, such as PVD (physical vapor deposition) and PECVD (plasma enhanced chemical vapor deposition) are particularly popular: gas phase processes offer an alternative to wet coating methods, often used for decorative applications, which become increasingly unacceptable for environmental reasons. The control of hardness and other mechanical properties of materials can be achieved in two ways [1, 24]: (a) by using materials with strong covalent interatomic bonding, or (b) by designing the structure of materials on the micro- and nanometer scales.

The first group (a) considers hard materials such as polycrystalline diamond (pc-D), carbon nitrides (CN_x), and other nitrides and carbides (e.g. c-BN, WC, TiN, TiC, TiCN). They possess excellent mechanical and tribological properties, high hardness, high wear resistance, low friction coefficient [24] and high stability in corrosive environments.

They also provide attractive colors [145, 146]. Their key property is the strong chemical bonding. Characteristics such as the nucleation process and adhesion of pc-D [77], as well as the elastoplastic properties and the significant elastic recovery in CN_x films [68] have been studied.

In the second group (b) of hard materials enhanced mechanical performance is obtained by introducing inner interfaces for blocking the propagation of dislocations and the growth of cracks [119, 147]. This is achieved by mixing a hard, more brittle material, with a material, which is softer and more elastic. In such case the design of microstructure aims at obtaining a higher hardness than the one resulting from the simple rule of mixture. Such design requires understanding of the materials properties and operation on the nanoscale. Two approaches can be applied: (i) 2D systems, such as multilayers and superlattices [24, 71-72, 100, 104, 148], and (ii) 3D systems, such as nanocomposites [73-74, 111, 118-119, 122, 149-152].

In the first case (i), the layers possessing a lower hardness, H, and a lower Young's modulus, E, block the propagation of dislocations, produced under high stress conditions in the layer possessing higher H and E. In such a structure the stress concentration in the interface region can be substantially reduced. For optimal mechanical properties frequently yielding H values in the order of ~ 50 GPa, the period of the multilayer structure must be very small (typically few nm) [72, 148]. In the second case (ii), the composites consist of small nanocrystals of a hard material, a few nanometers in diameter, that are embedded in a matrix of a softer amorphous material [111]. Appropriate choice of materials constituting the matrix and the nanocrystals may prevent boundary sliding. Moreover, there are virtually no dislocations present in very small crystals. For such systems, H is enhanced beyond a value expected from the rule of mixture, and values even up to 100 GPa have been reported [118-119] and discussed [112, 120, 153].

PECVD is increasingly attractive for the deposition of hard coatings. In fact, it combines the advantages of both CVD (chemical vapor deposition) and PVD techniques; this includes: (i) initiation of chemical reactions in the gas phase, accompanied by the presence of new chemical species such as ionized precursors, (ii) deposition at a low substrate temperature, and (iii) large range control of plasma-surface interactions that influence film structure and morphology.

In the present work, we study nanocomposite (nc) films formed by TiN particles embedded in an amorphous hydrogenated silicon nitride matrix (nc-TiN/$SiN_{1.3}$) fabricated by PECVD at low substrate temperature (T_s = 300 °C). In such case, low T_s offers obvious advantages such as wider choice of substrates, lower thermal stress and possibly lower cost. The nc-TiN/$SiN_{1.3}$ are compared with those prepared at T_s = 500 °C which possess high *H, E* (> 40 GPa and > 350 GPa, respectively) and higher thermal stresses. A multitechnique characterization approach is applied in order to establish a simple structural model, which explains the film properties.

In the first part we focus on the methodology of hardness measurement which is frequently a source of contradicting *H* values reported in the literature [154]. In fact there are two main difficulties associated with *H* and *E* measurements for thin films on a substrate. One stems from the influence of the substrate itself, the second one from negligence of the elastic properties of the investigated materials [153]. In this critical analysis we compare the approaches based on geometrical models of Jonsson and Hogmark (J-H) [155], Burnett and Rickerby (B-R) [129, 156], Chicot and Lesage (C-L) [157], Korsunsky et al. (KOR) [158] and Ichimura et al. (ICH) [159] with direct depth–sensing indentation (DSI) hardness measurements interpreted using the classical method of Oliver and Pharr (O-P) [130] and the Work of Indentation (W-I) [160]. In the second part of this paper the behavior of the nc-TiN/$SiN_{1.3}$ coatings is explained in terms of the structure–property relationships.

4.3. Experimental methodology

4.3.1. Film deposition

The films were deposited in a radio frequency (RF, 13.56 MHz) plasma system in which the substrates were placed on an RF powered electrode (10 cm in diameter) where an RF-induced, negative DC self-bias, V_B, develops. The substrate holder could be heated up to 500 °C by using an inductive heater from the backside and halogen lamps from the front side. Working gases, namely $TiCl_4$, SiH_4, N_2, H_2 and Ar were introduced via circular distributors; their flow was controlled by MKS and Sierra mass-flow controllers in each line, and the working pressure was measured by a capacitance gauge (MKS Baratron). Prior to experiment the system was evacuated to 10^{-5} Torr ($1.33*10^{-3}$ Pa) using a turbomolecular pump.

The film fabrication process consisted of two plasma pretreatment steps in Ar and in N_2, followed by a 1 hour deposition time using the conditions summarized in Table 4.1. The choice of process parameters results from our preliminary optimization study in which we obtained the properties (H and chemical composition) of pure TiN comparable to those reported for PVD films. During the deposition all conditions were kept constant, while the concentration of the $SiN_{1.3}$ phase in the nc-TiN/$SiN_{1.3}$ was controlled by adjusting the SiH_4 flow between 0 sccm (pure TiN) and 3 sccm. The films were deposited at T_s = 300 °C and T_s = 500 °C, and the thickness was between 1.5 and 2.0 μm, measured by a Sloan Dektak II profilometer. Based on our earlier studies of ion fluxes and ion energy distribution functions [36], we estimate that the ion current density during the film growth was about 100 μA/cm^2. Crystalline silicon, (c-Si) (100), was used as substrate, and it was cleaned in an ultrasonic bath with acetone and isopropanol to eliminate organic surface contaminants.

Table 4.1. *Deposition conditions for the nc-TiN/SiN$_{1.3}$ films.*

Process	Time [min]	Substrate temperature [°C]	Pressure [mTorr, Pa]	Bias voltage [V]	Gas flow [sccm]				
					Ar	N_2	H_2	$TiCl_4$	SiH_4
Pretreatment (1)	10	300, 500	40, 5.33	-600	40	---	---	---	---
Pretreatment (2)	30	300, 500	300, 40.00	-600	---	40	---	---	---
Deposition of TiN/SiN$_{1.3}$	60	300, 500	200, 26.66	-600	40	15	100	9	0-3

4.3.2. Mechanical properties

In the first series of experiments the hardness measurements were made using the micro scratch tester (MST, CSEM, Neuchatel, Switzerland), modified to perform indentations. H was obtained from the length of the imprint diagonal using a Vickers indenter, loads from 0.05 to 0.1 N, and a loading rate of 0.01 N/s. In the second series, the mechanical properties were assessed by DSI using the Triboindenter (Hysitron Inc.) equipped with a Berkovich pyramid. The applied loads ranged from 3 to 9 mN. For each load, H was obtained from ten indentations.

Toughness was determined from indentations made at a load of 2 N, while the length of the resulting radial cracks was measured optically. The relationship between the fracture toughness, K, and the indentation crack length, c, can be expressed as [2]:

$$K = B_{in}\left(\frac{E}{H}\right)^{0.5}\left(\frac{L}{c^{3/2}}\right) \tag{4.1}$$

where B_{in} is a geometrical constant depending on the indenter (for Vickers, B_{in} = 0.016) and L is the applied load.

Film stress was obtained from the curvature of silicon substrates before and after deposition, using a Sloan DEKTAK II profilometer and a Tencor FLX 2900 thin film stress measurement system, both employing the Stoney formula [1].

4.3.3. Structural characterization

The film microstructure and composition were evaluated by different techniques. X-ray diffraction (XRD) measurements were performed with a Philips X'Pert diffractometer using the Cu-K_α line (λ = 1.54 Å). The TiN grain size was obtained using the Debye-Scherrer formula [161]. Scanning electron microscopy (SEM) observations were performed using a Philips XL 20 system equipped with an X-ray detector. Complementary compositional depth profiles and surface roughness were obtained, respectively, by elastic recoil detection in the time–of-flight regime (ERD-TOF [142]) and by atomic force microscopy (AFM, Digital Instruments, 10 x 10 μm scanned surface). Additional analyses (not shown here) were made by transmission electron microscopy (TEM) Philips CM 30 and X-ray photoelectron spectroscopy (XPS) using a VG-ESCALAB 3MKII instrument.

4.4. Results and discussion

4.4.1. Methodology of hardness evaluation

As mentioned above, there has been a considerable disagreement in the literature regarding the determination of hardness for relatively thin (typically < 3 μm thick) hard films. H of such films can be obtained if the indentation depth does not exceed 10 % of the film thickness, t_f. The size of residual impression in conventional hardness tests is usually considered to be identical to the contact area, A_{in}, at the full load, L, although the depth of penetration, h, may be significantly reduced by elastic recovery of the film. This effect should be taken into consideration when applying loads lower than 0.5 N.

Elastic recovery can be accounted for in DSI measurements; here, too, the hardness is calculated as $H=L/A_{in}$, but the load-displacement curve, $L(h)$, and the value of A_{in} must be carefully evaluated, as described below. In the following we systematically compare the

results obtained by both static indentations and DSI, while considering the elasto–plastic behavior.

In the first set of experiments we applied the J-H, B-R, C-L, KOR and ICH models to eliminate the influence of the substrate. These models were modified to take into account the Indentation Size Effect (ISE) that describes the variation of H for homogeneous films at different loads applied to the indenter. This stems from the errors associated with A_{in}, particularly when very small h values are used. H may be expressed as [129, 156]:

$$H = qs^{M-2} \tag{4.2}$$

where q is a constant, s is the indent diagonal (proportional to L), and M is the ISE (Meyer) index. For $M = 0$ there is no ISE effect, and H does not vary with L. When $M < 2$, H increases for decreasing L, and when $M > 2$, H increases with increasing L. The values of q and M can be determined by fitting Eq. 4.2 with experimental data. For ceramic coatings, such as TiN, M is typically between 1.6 and 1.7, while it may be substantially smaller for very hard coatings such as DLC. For most ceramics and many metals M is between 1.6 and 1.9 [3, 129, 156].

The ISE is illustrated in Fig. 4.1 for the particular case of c-Si, where a strong effect of applied load on H is clearly visible. Considering the Vickers indenter and using Eq. (4.2) and the loads ranging from 0.05 to 0.5 N, we obtained q = 12.5 GPa and M = 1.84. In these measurements, five indentations were made at each load and their size was determined by SEM. This approach largely decreases the uncertainty in the determination of s by optical microscopy for $s < 10$ μm. In fact, compared to SEM, s measured optically was found systematically 10% to 20% lower for $s \sim 10$ μm and $s \sim 2$ μm, respectively. Such discrepancies may lead to an overestimation of H when relying only on optical observations.

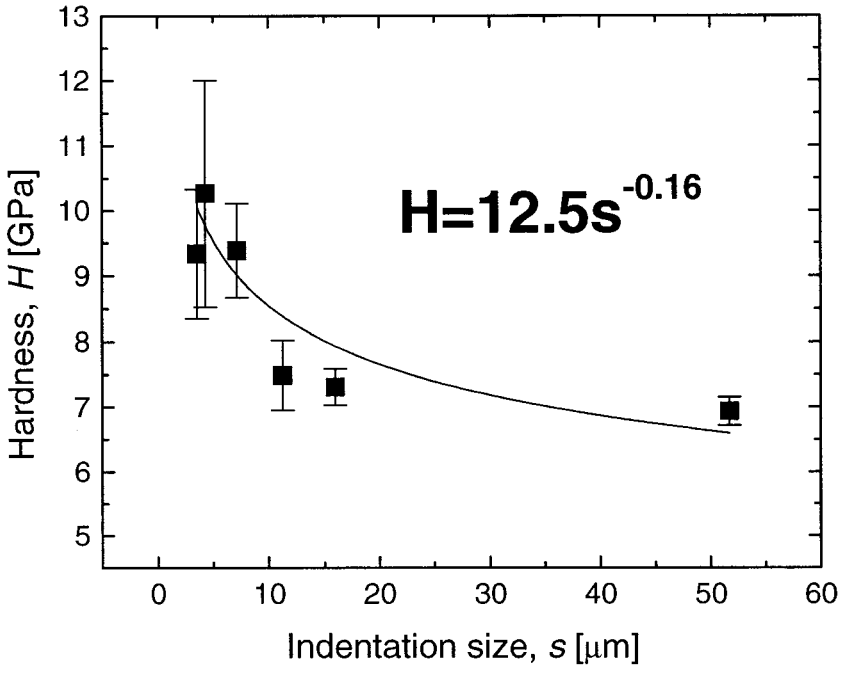

Figure 4.1. *Indentation Size Effect (ISE) for a c-Si substrate.*

Numerous models based on static indentations attempt to relate the measured composite hardness, H_c, with the hardness of the substrate, H_s, and of the film, H_f. All geometrical models presented below can be expressed using the following equation:

$$H_c = H_s + a_h(H_f - H_s) \tag{4.3}$$

where a_h is a coefficient defined below.

Jonsson and Hogmark [155] based their J-H model on purely geometrical considerations. It is valid for indentations where the relative indentation size ($\beta = h/t_f$) is high. The main assumption is that the cracked parts of the coating (due to indentation) transmit the load to the substrate. The increase of H_c with respect to H_s is related to the area of the deformed coating that surrounds the indentation region. The coefficient a_h from Eq. 4.3 is then expressed as:

$$a_h = 2C\frac{t_f}{s} - \left(C\frac{t_f}{s}\right)^2 \tag{4.4}$$

where C is the geometrical constant. For hard coatings on soft substrates, using a Vickers indenter, $C = 2\sin^2(11^\circ)$, and for coatings with a hardness comparable to that of the substrate, $C = \sin^2(22^\circ)$.

Burnett and Rickerby [129, 156] proposed an approach (B-R), assuming a hemispherical volume of deformation during indentation. They calculated the volumes of plastically deformed film and substrate, and subsequently applied the mixture law to calculate the increase of H_c caused by the film. The increase of the measured hardness is proportional to the ratio of the deformed film volume to the total deformed volume of the film and the substrate. The coefficient a_h is given as:

$$a_h = \left(\frac{V_f}{V_s + V_f}\right)^{1/2} \tag{4.5}$$

where V_f and V_s are the volumes of the plastically deformed film and the substrate, respectively. The volume of plastic deformation can be calculated using a model of spherical cavity with radius $b_{f,s}$, which is related to the size of indentation as [162]:

$$b_{f,s} = r_{in}s\left(\frac{E_{f,s}}{H_{f,s}}\right)^{1/2}\cot^{1/3}\xi \tag{4.6}$$

where r_{in} is a constant (approximately equal to 1), ξ is the indenter semi-angle ($\xi = 74^\circ$ for the Vickers indenter), and f and s denote the film and substrate, respectively.

A similar model based on the calculations of plastically deformed volumes and the mixture law was proposed by Chicot and Lesage (C-L) [157]. The coefficient a_h in this case is:

$$a_h = \frac{3}{2}\frac{t_f}{s}\left[\left(\frac{H_f}{E_f}\right)^{1/2} + \left(\frac{H_s}{E_s}\right)^{1/2}\right]\tan^{1/3}\xi \tag{4.7}$$

A different approach was proposed by Korsunsky et al. [158]. The KOR model considers plastic work of deformation in the substrate and deformation and fracture in the coating. The coefficient a_h is given as:

$$a_h = \frac{1}{1 + k_{in}\beta^2} \tag{4.8}$$

where k_{in} is the material constant determined experimentally.

Recently, another model was introduced by Ichimura et al. [159]. Based on the mixture law the a_h coefficient in the ICH approach is written as:

$$a_h = 3\left(\frac{H_f}{E_f}\right)^{1/2} \frac{t_f}{s} \tan^{1/3}\theta_{in} \tag{4.9}$$

where θ_{in} is the angle between the opposite faces of the indenter ($\theta_{in} = 68^\circ$ for the Vickers indenter).

Evaluation of hardness obtained from DSI measurements is based on the O-P [130] and W-I [160, 163-167] methods. In the frequently used O-P approach to nanoindentation, A_{in} is expressed as:

$$A_{in} = \frac{\pi}{4}\left(\frac{S_{in}}{E_r}\right)^2 \tag{4.10}$$

where E_r is the reduced Young's modulus and S_{in} is the stiffness defined by the initial slope of the unloading curve:

$$S_{in} = \frac{dL}{dh} \tag{4.11}$$

In order to obtain reliable H values, A_{in} has to be known with high precision (in the subsequent text, $H = H_f$). The most commonly encountered source of error in determining A_{in} derives from a non-ideal shape of the indenter. After repetitive indentations, there are inevitable changes in the indenter geometry due to wear, especially

when hard or superhard (H > 40 GPa) materials are tested. The indenter becomes more blunt and h and A_{in} decrease resulting in higher apparent H values. We estimate that after 1 year of regular use of an indenter the changes in A_{in}, if not properly corrected, can account for an overestimation of H up to 30%. Therefore, we strongly underline the need for appropriate determination of A_{in}. In our experiments, A_{in} was evaluated from a series of indents with loads ranging from 1 μN to 1000 μN on a fused silica standard with known values of H, E_r and the Poisson's ratio, υ.

Other possible sources of error are related to the material properties such as roughness, residual stress, surface oxide etc. Inadequate values of A_{in} and non–rigorous evaluation of the elastic rebound are frequently responsible for very high values of H and E reported in the literature.

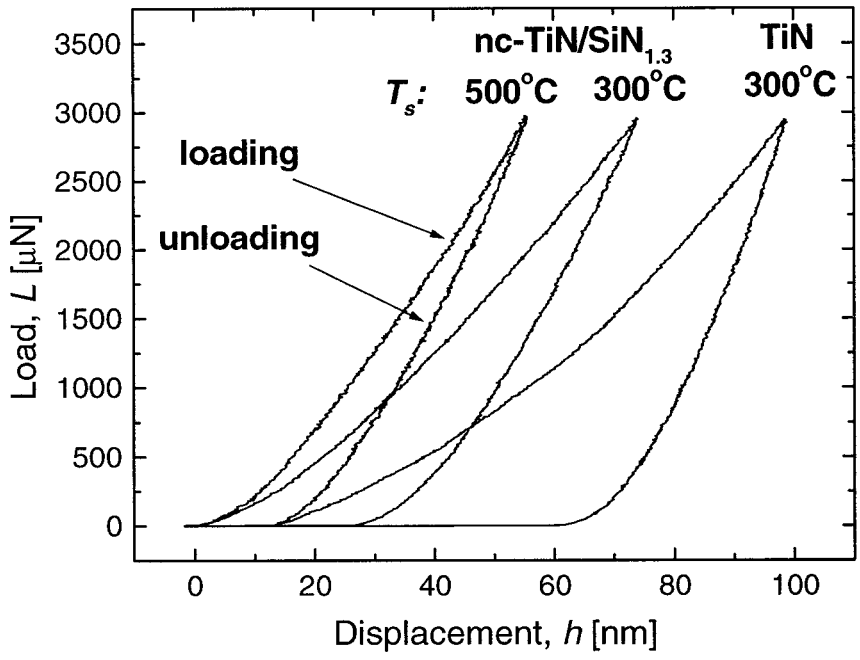

Figure 4.2. *Load-displacement curves for nc-TiN/SiN$_{1.3}$ and TiN films.*

The W-I method takes into consideration the elasto–plastic behavior of the material. The energy of plastic deformation, W_p, can be expressed as a difference of the area between the loading and unloading curves. The energy of elastic deformation, W_e, is the area under the unloading curve (Fig. 4.2). H is defined as:

$$H = \frac{W_p}{V_f} \tag{4.12}$$

where V_f is the volume of plastic deformation. Different models were proposed to determine V_f, frequently using the following relationship for the relative indentation volume [163-164]:

$$\alpha_{in} = \left(\frac{V_f}{\Delta V} \right)^{1/3} \tag{4.13}$$

where ΔV is the volume of indentation. In the present work, we consider nc coatings with a ratio of $E_r/H \sim 10$, small loads between 3 and 9 mN, and $\alpha_{in} \sim 1.0$. It means that V_f is almost equal to ΔV. This result, based on the models mentioned above, underlines the significance of the elastic properties of the investigated nc coatings.

Using the methodological approaches described above, we can now compare the experimental values of H obtained for the nc–TiN/$SiN_{1.3}$ films deposited at 300 °C (see Fig. 4.3). Comparison of H values determined by static indentation and different mathematical models is shown in Fig. 4.3a, while the H values obtained by DSI, using the O-P and W-I models, are shown in Fig. 4.3b.

There is a good agreement between all methods. The J-H, KOR, and B-R models yield systematically higher values, compared to the C-L and ICH models and the DSI measurements. The differences between the direct measurements (DSI) and the models arise from the fundamental problem of hardness definition in these two cases, especially from neglecting the elastic behavior in static indentations.

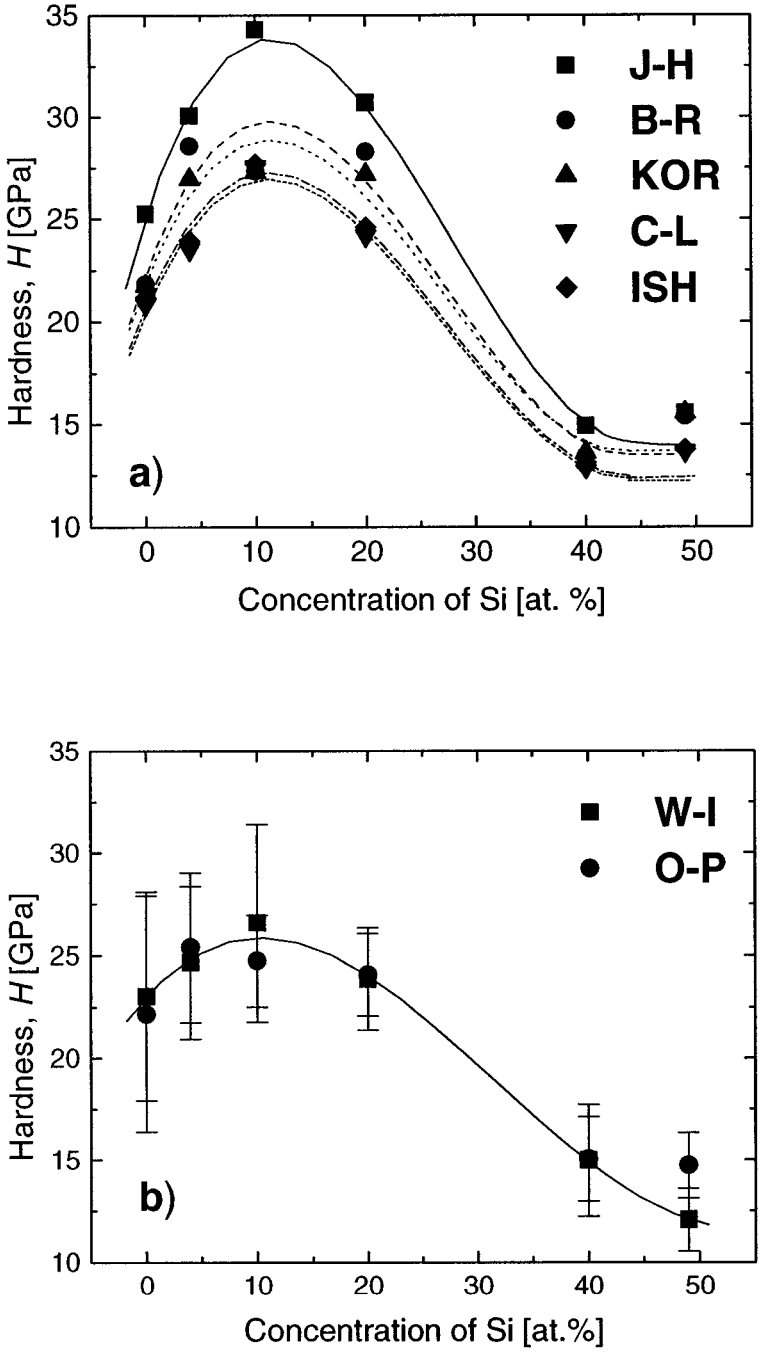

Figure 4.3. *Hardness vs Si concentration in nc-TiN/$SiN_{1.3}$ films deposited at T_s = 300 °C, obtained from different approaches: (a) static indentation models, and (b) Oliver and Pharr (O-P), and Work-of-Indentation (W-I) models.*

The high standard deviation in H obtained from depth–sensing indentations is possibly due to very small loads (from 3 to 9 mN). In such case, the penetration depth is small (not exceeding 200 nm), and surface inhomogeneities and surface roughness may have contributed to a scatter of experimental data. In addition, the fact that the depth of penetration is squared increases the experimental error [154].

4.4.2. Mechanical properties of nc-TiN/$SiN_{1.3}$ films

After having established the methodology of hardness measurements we will now analyze in more detail the mechanical properties of the nc-TiN/$SiN_{1.3}$ films. The effect of Si concentration, [Si], on H and E_r obtained by DSI for films fabricated at T_s = 300 °C and T_s = 500 °C is shown in Fig. 4.4. Both dependencies clearly exhibit a maximum at an optimum [Si] situated between 5 and 10 at. %. This corresponds to an amount of $SiN_{1.3}$ phase which forms a matrix in which TiN particles are embedded. The effect of TiN precipitation is less pronounced at a lower T_s = 300 °C; this gives rise to lower values of H = 25 GPa and E_r = 270 GPa compared to higher values of H = 45 GPa and E_r = 350 GPa for films deposited at T_s = 500 °C.

The nc-TiN/$SiN_{1.3}$ system exhibits a more elastic behavior compared to TiN as already shown in Fig. 4.2. In fact, the W_p/W_e ratio for TiN is much higher than for the nc-TiN/$SiN_{1.3}$. For T_s = 300 °C, E increases by 25% from 200 GPa for pure TiN to E = 270 GPa for the nc-TiN/$SiN_{1.3}$; for T_s = 500 °C this difference is even higher (~ 30%). Highly elastic behavior for the nc structures can be explained by crack formation within the grain boundaries under high-stress conditions [119]. When the stress (indentation load) is removed the cracks close, releasing back the energy.

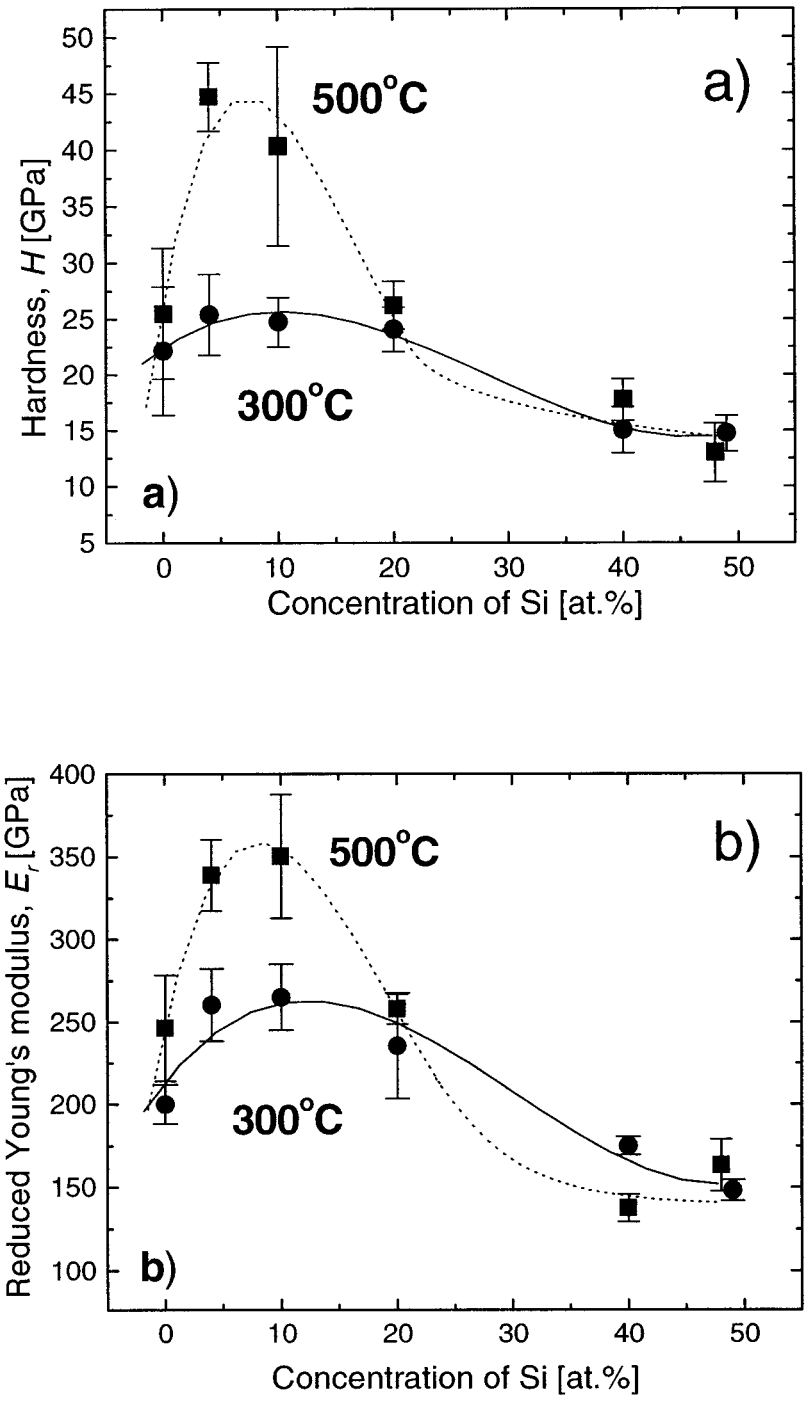

Figure 4.4. *Hardness (a) and reduced Young's modulus (b) vs Si concentration in nc-TiN/$SiN_{1.3}$ films fabricated at T_s = 300 °C and 500 °C.*

Toughness is an important mechanical property related to the materials resistance against shock loads, and it describes the resistance against the formation of cracks resulting from stress accumulation in the vicinity of structure imperfections. K determined for our nc-TiN/$SiN_{1.3}$ films is plotted versus [Si] in Fig. 4.5. It appears that the K values follow a similar behavior compared to E_r (see Fig. 4.4). The maximum in K coincides with the maximum value of the E_r/H ratio (see Eq. 4.1), corresponding to an optimum [Si] of 5 - 10 at. %; in this case K increased from 1.3 MPa $m^{1/2}$ for pure TiN up to 1.8 MPa $m^{0.5}$. Further increase in K for [Si] > 40 at. % can be related to the predominant $SiN_{1.3}$ phase, for which we obtained high K (~ 4 MPa $m^{1/2}$) but substantially lower H (~ 18 GPa) and E_r (~ 160 GPa) values. For comparison, H and E values for pure TiN have been reported to vary from 20 to 27 GPa and from 200 to 590 GPa, respectively [1, 95]. For nc-TiN/$SiN_{1.3}$ films fabricated at T_s > 500°C, H and E_r values were found to vary from 35 to even 110 GPa, and from 300 to 600 GPa, respectively [112, 120, 151].

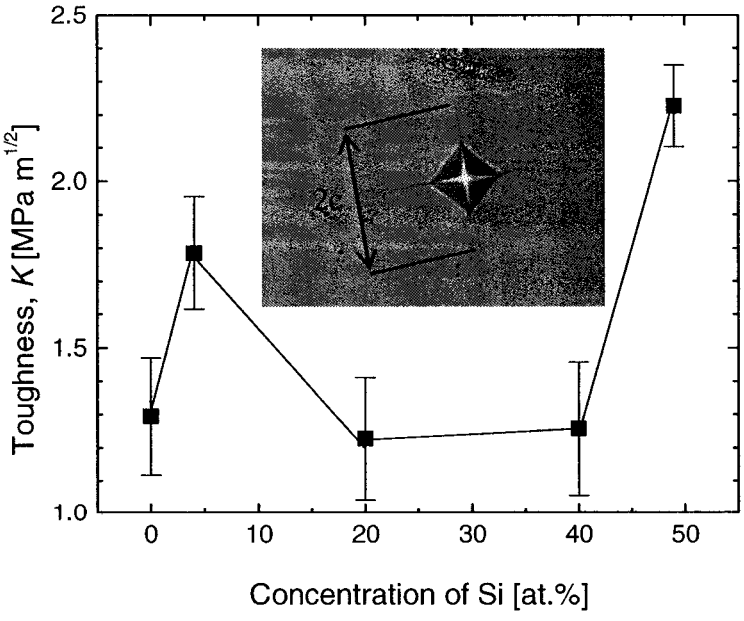

Figure 4.5. *Toughness vs Si concentration in nc-TiN/$SiN_{1.3}$ films deposited at T_s = 300 °C.*

In general, the theoretical strength of materials (cohesive energy) is approximately equal to 0.1 G, where G is the shear modulus of a given material. However, the practical strength is 2 to 4 orders of magnitude smaller due to the presence of defects, such as dislocations and cracks, which lead to material failure under high stress conditions. For the small grains of a crystalline material (in our case ~ 8 nm) and small interparticle distances (1 – 2 nm), where the inner surface to volume ratio is larger. This feature of the binary TiN/$SiN_{1.3}$ nanocomposites has a large influence on their physical properties, namely H, E_r, and K, as it was shown above and as also observed by others [74-75, 111-112, 118-120, 149, 151]. Introduction of new internal interfaces prevents grain boundary sliding [147]; this lowers the limit of the inverse "Hall-Petch" effect that occurs for a grain size of about 20-50 nm [3]. Therefore, virtual absence of dislocations in small (~ 8 nm size) grains leads to a significant increase of H [112-113].

The amorphous $SiN_{1.3}$ phase is characterized by a smaller value of E and H, where cracks can appear more easily under high stress conditions. However, their propagation on microscale, that results in plastic deformation on macroscale, is blocked by the densely packed nanocrystals as discussed by Veprek et. al. [119]: in order to propagate in the nanocomposite, the crack must undergo bending and branching that stop its propagation. Moreover, the crack sizes are limited to nanocrystal dimensions; therefore, the ratio of their length to width is small and the stress concentration factor is low. In addition, small cracks are also easy to close. Therefore, some of the cracks, initiated during the loading part of the indentation process, close during the unloading cycle, releasing the accumulated energy. This can explain the highly elastic behavior of such materials.

Fig. 4.6 shows the total stress, σ_{tot}, for films grown at 300°C. A maximum is reached for [Si] ~ 5 %, similarly to the behavior observed for H, E_r and K vs [Si] in Figs. 4.4 and 4.5. The value of σ_{tot} is a sum of the intrinsic stress, σ_{in}, and the thermal stress, σ_{th}, while $\sigma_{tot}=\sigma_{in}+\sigma_{th}$. In order to separate σ_{in}, we calculated σ_{th} by approximating the coefficient

of thermal expansion (CTE) for the nc-TiN/$SiN_{1.3}$ by a mixture law. For pure TiN and pure $SiN_{1.3}$ we considered the CTE values of $9.35*10^{-6}K^{-1}$ and $2.5*10^{-6}K^{-1}$, respectively [1]. For films possessing the highest H values ([Si] ~ 5 - 10%) we assumed TiN grains (8 nm in diameter observed in TEM and measured by XRD) separated by 1 nm thin $SiN_{1.3}$ layers (see section 3.3). In such case the estimated thermal stress is tensile, σ_{th} = +0.4 GPa. According to these calculations the maximum σ_{in} varies between -1.1 to –1.5 GPa for samples exhibiting the highest H. This value appears small compared to the σ_{in} values for PVD nc-TiN/$SiN_{1.3}$ coatings reported by others [151] for a similar coating thickness (2 μm) and T_s (300 °C). Lower stresses in PECVD films with respect to their PVD equivalents is most probably due to lower ion bombardment energies during the deposition process.

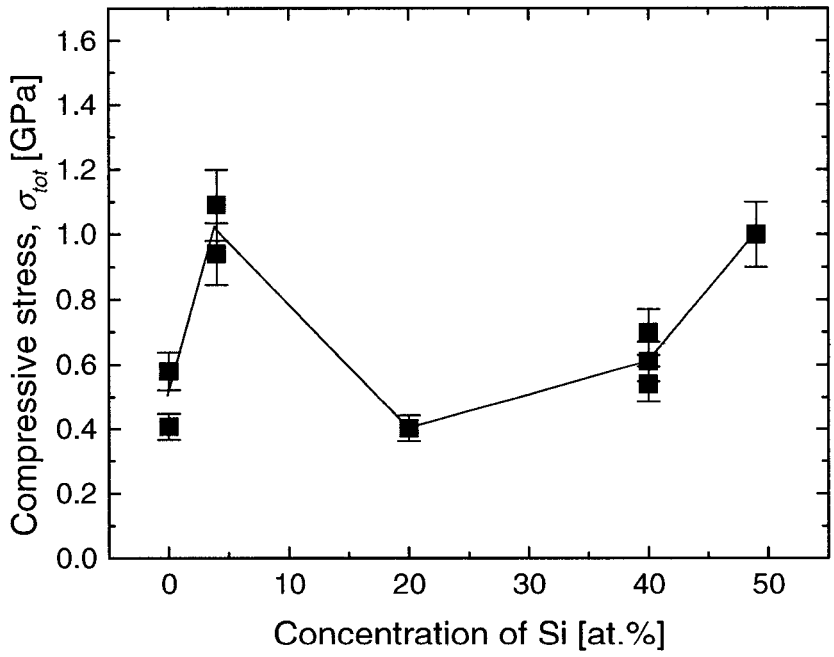

Figure 4.6. *Total compressive stress as a function of Si content in nc-TiN/$SiN_{1.3}$ films deposited at T_s = 300 °C.*

The presence of a maximum in Fig. 4.6 confirms the importance of the [Si] in the development of the nc structure, as well as the contribution of stress to the highest H and E_r values. For [Si] > 10 % σ_{tot} increases monotonously.

4.4.3. Structural characterization

In this section we evaluate the film microstructure with the aim to explain the mechanical behavior of the nc-TiN/$SiN_{1.3}$ coatings. Typical XRD spectra are shown in Fig. 4.7 for films with different [Si]. All peaks are due to the TiN component. When [Si] is increased, all features due to TiN, namely the [200], [220], [311] and [222] orientations decrease their intensity, while a new orientation ([111]) appears. High intensity of the [200] peak is symptomatic of TiN materials deposited under intense ion bombardment leading to film densification [73, 168]. We found that for all peaks the FWHM, $\Delta\theta$, does not vary with [Si]. For [111], [200] and [220] orientations $\Delta\theta$ values were 1.7°, 1.3° and 1.8°, respectively. This indicates that the crystal size does not change, but the crystals become more "diluted" (increased separation) at higher [Si] values. Using the Debye–Sherrer equation, the TiN crystal size was estimated between 5 and 8 nm. These values were also confirmed by direct TEM observations (not shown here), which indicated an average grain size between 8 and 10 nm. This result is in agreement with the findings of other authors [119-120].

In the case of TiN and $SiN_{1.3}$ for which no ternary system exists, formation of the binary TiN/$SiN_{1.3}$ nanocomposite structure can be explained by the thermodynamically driven segregation of TiN and $SiN_{1.3}$. Phase segregation occurs when the second derivative of the formation energy, ΔE_g, of the mixed phase (eg. $Ti_{1-x}Si_xN$), is negative [112, 120, 169]:

$$\frac{\delta^2(\Delta E_g)}{\delta x^2} < 0 \qquad (4.14)$$

Under such circumstances, any local fluctuation of composition leads to spontaneous phase separation.

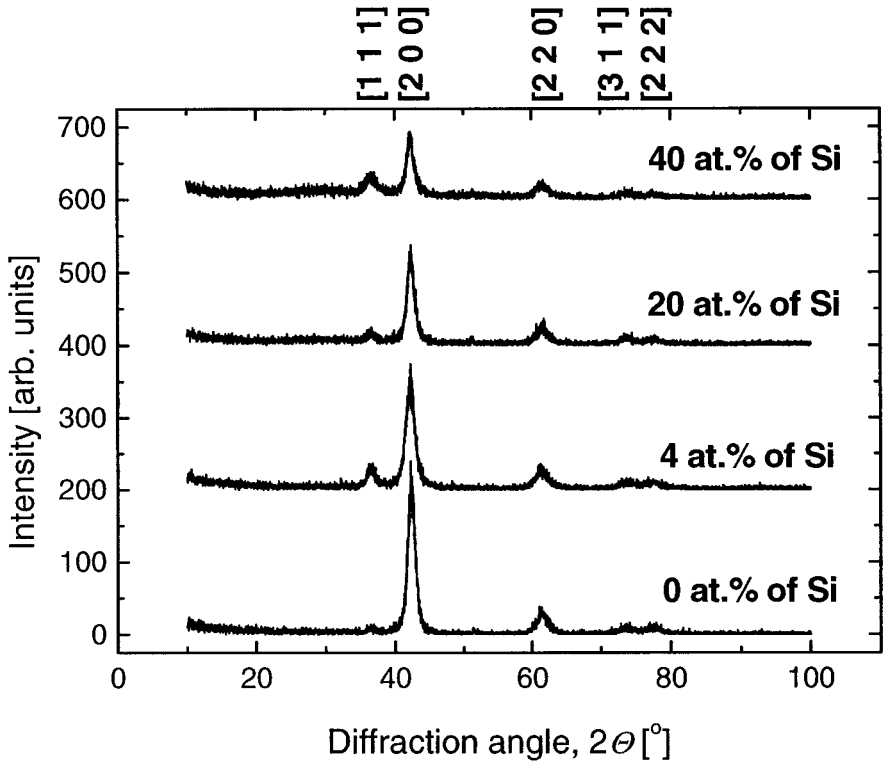

Figure 4.7. *XRD spectra of nc-TiN/SiN$_{1.3}$ films deposited at T_s = 300 °C .*

Film composition was evaluated by ERD-TOF and XPS. As an example, an ERD-TOF concentration depth profile is shown in Fig. 4.8 for a nc-TiN/SiN$_{1.3}$ sample deposited at 300 °C which possesses the highest H value (see Fig. 4.3). In this case we detected around 50 at. % of Ti, 40 at. % of N, 5 at. % of Si, 3 at. % of Cl and 1 at. % of O. All samples exhibited a good compositional uniformity throughout the layer thickness, with a small amount of oxygen present at the surface. All samples were found substoichiometric in N, but all N was bonded to Ti or Si. Lower values of [N] can be related to the low values of T_s, which was probably insufficient to enhance reaction of Ti and Si with nitrogen. XPS analysis confirmed the presence of silicon and titanium nitrides, but no formation of Ti-Si bonds has been detected.

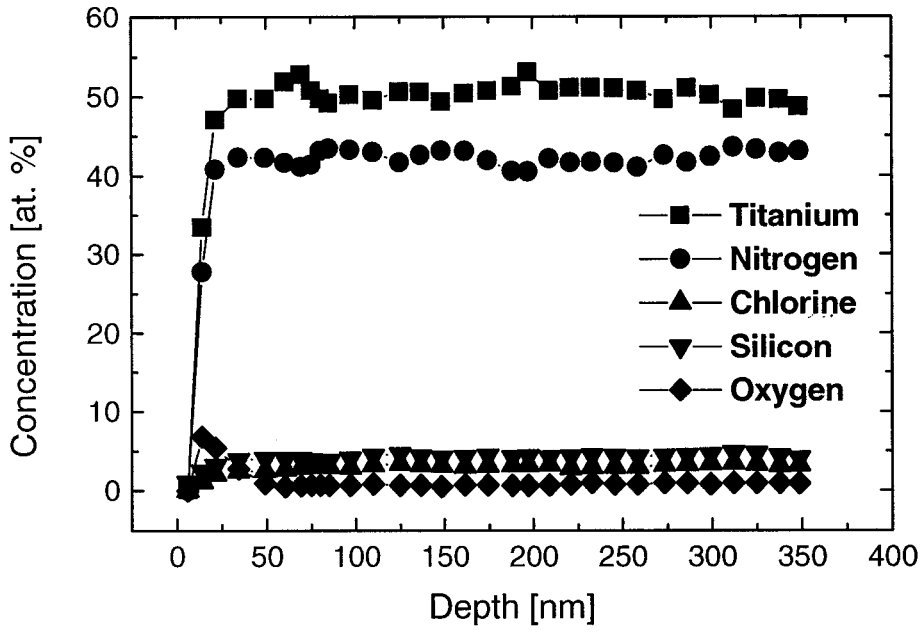

Figure 4.8. *ERD TOF concentration depth profile through a nc-TiN/$SiN_{1.3}$ film deposited at T_s = 300 °C.*

The materials morphology is illustrated by SEM cross sections in Fig. 4.9 for films deposited at 300 °C. The predominantly columnar structure of pure crystalline TiN (Fig. 4.9a, film thickness 1.1 μm) is disrupted by introducing the amorphous $SiN_{1.3}$ phase as clearly visible when nc-TiN/$SiN_{1.3}$ is deposited on top of TiN (Fig. 4.9b). In the latter case, phase segregation between the crystalline and amorphous materials is responsible for stopping grain growth and for stimulation of renucleation; this results in nc structure with no columnar growth. In this way, the microstructural development traditionally described for single-phase materials using the Structure Zone Models [25-26] is fully changed by containing a small amount of "additives" [122].

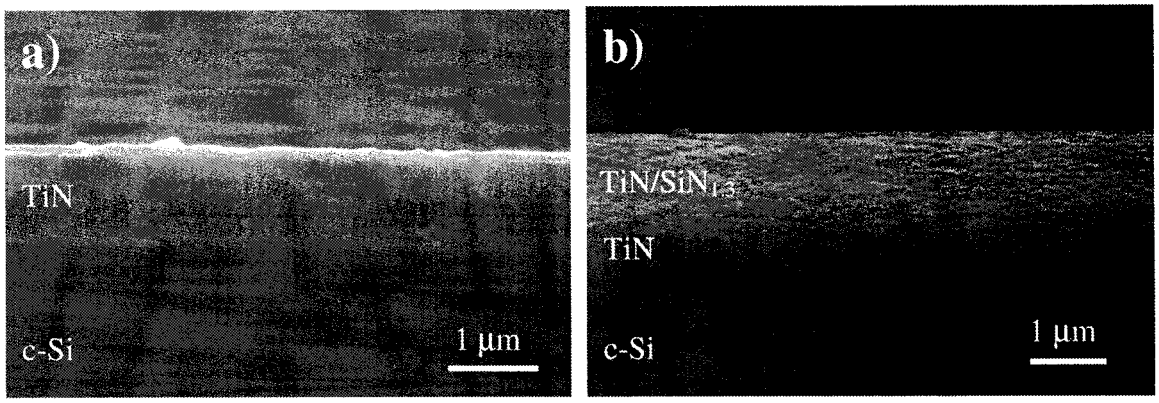

Figure 4.9. *SEM cross section micrographs of (a) TiN and (b) nc-TiN/$SiN_{1.3}$-TiN double-layer films deposited at 300 °C on a c-Si substrate. The film thicknesses were 1.1 μm and 1.6 μm, respectively.*

Evolution of the microstructure strongly affects the surface roughness, R_a. The initial value of R_a ~ 5.2 nm for the polycrystalline TiN drops to about 2 nm when the amorphous $SiN_{1.3}$ component is added (see Fig. 4.10). For comparison, R_a ~ 1 nm for pure $SiN_{1.3}$ films. Such change indicates a transition from a columnar TiN structure to a "feature–less" nc system, an effect which underlines high surface quality of amorphous PECVD films.

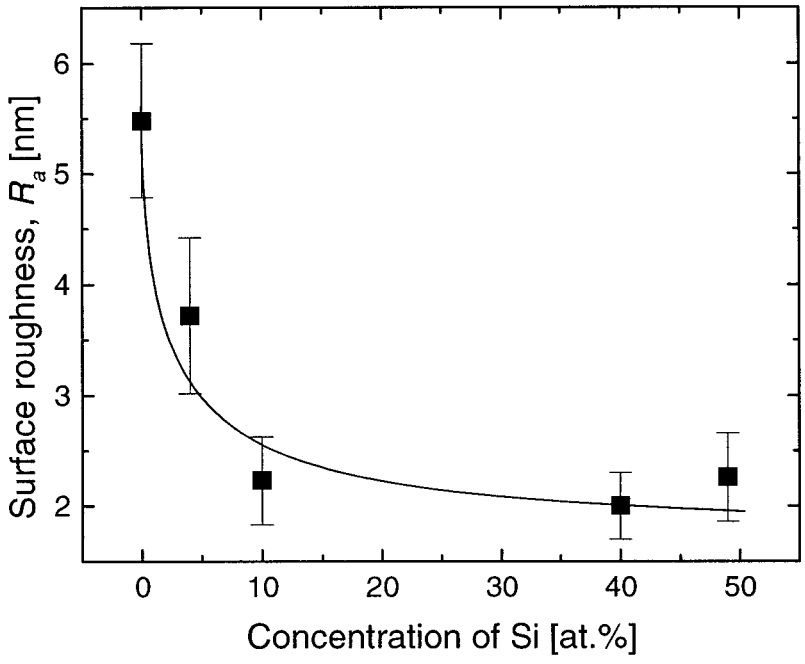

Figure 4.10. *Effect of Si content on the surface roughness, R_a, for films deposited at T_s = 300 °C.*

4.5. Conclusions

In the present work, we systematically studied the mechanical properties of nanocomposite TiN/$SiN_{1.3}$ films, in which the concentration of the $SiN_{1.3}$ component was varied. We have determined that the TiN/$SiN_{1.3}$ materials behave as a two phase material; in fact, occurrence of an alloying effect could be ruled out, since the film properties, in particular H and E, do not obey the mixture law. In addition we observed that significant changes in the material's performance (namely H, E_r, K and σ_{tot}) are induced by a small change in the microstructure.

In the first part of this study, we investigated the methodology and the interpretation of the mechanical measurements, namely hardness and reduced Young's modulus. We have quantitatively compared the results from DSI, using the Oliver and Pharr model, with those taking into account the work of plastic and elastic deformation, and different models considering the indentation size effect. We concluded that, if applied correctly, these approaches yield comparable values within about 10 %.

In the second part, we systematically studied the mechanical behavior and microstructure of the nc-TiN/$SiN_{1.3}$ films. For an optimum concentration of Si (5 – 10 at. %), we obtained high values of microhardness (25 and 45 GPa) and of reduced Young's modulus (270 and 350 GPa) for the films deposited at 300 and 500 °C, respectively. These values are substantially higher than for the individual TiN (H ~ 22 GPa, E_r ~ 200 GPa) and $SiN_{1.3}$ (H ~ 18 GPa, E_r ~ 160 GPa) materials. The film behavior was explained by a phenomenological model based on a system in which TiN nanocrystals of a constant size (~ 8 nm) are embedded in a $SiN_{1.3}$ matrix. The highest H value is obtained when the inter–particle distance (1 – 2 nm) is optimized which also coincides with a maximum in the film toughness (K = 1.8 MPa $m^{1/2}$) and total compressive stress (σ_{tot} –1.0 GPa). Surface roughness was found to decrease from ~ 5.2 nm for TiN to ~ 2.0 nm for 50 % TiN / 50 % $SiN_{1.3}$. Encouraged by very attractive mechanical properties of the nc-TiN/$SiN_{1.3}$ films we now concentrate on a detailed investigation of the tribological and optical characteristics in view of their metallurgical, protective, decorative (optical) and other applications.

Acknowledgements

The authors acknowledge the expert technical assistance of Mr. Jiri Cerny and Mr. Gilles Jalbert. We also wish to thank Dr. Oleg Zabeida, Dr. Jorg Oberste-Berghaus and other members of the GCM for stimulating discussions. This work was supported by the Natural Sciences and Engineering Research Council (NSERC) of Canada.

Chapter 5. Article 2: Optical Characteristics and Color of TiN/$SiN_{1.3}$ Nanocomposite Coatings

This article is a continuation of the systematic characterization of nc-TiN/$SiN_{1.3}$ coatings. Due to their excellent mechanical properties and interesting colors hard nc-TiN/$SiN_{1.3}$ films can be applied as decorative coatings. The main motivation of this article was the following:

This is the first time the optical and color effects of nc coatings have been evaluated. First we determine quantitatively the colors, which allows us to judge their suitability for decorative applications. Second, the quantitative knowledge of the optical properties, namely n, k, R_s gives us more insight into the microstructure of the nc coatings.

Optical Characteristics and Color of $TiN/SiN_{1.3}$ Nanocomposite Coatings

P. Jedrzejowski, B. Baloukas, J.E. Klemberg-Sapieha and L. Martinu
Groupe des couches minces (GCM) and Department of Engineering Physics,
Ecole Polytechnique, Montreal, Quebec, H3C 3A7 Canada

Submitted to: Journal of Vacuum Science and Technology A on 02/09/2003

Keywords: PECVD; nanocomposite structure; optical properties, color, microstructure

5.1. Abstract

Decorative and protective coatings deposited by dry methods are very attractive due to the environmental restrictions on traditional wet chemical techniques. In this context, nanocomposite hard coatings were fabricated by PECVD from $TiCl_4/SiH_4/N_2/H_2/Ar$ gas mixtures at substrate temperatures of 300 °C and 500 °C. Their optical characteristics such as refractive index, extinction coefficient, luminosity and colors were quantitatively determined by spectroscopic ellipsometry and spectrophotometry. Pure TiN exhibited a metal-like behavior, and its optical properties were modeled by the Drude (free carrier) approach. Nanocomposite films consisting of about 5 to 10 nm size TiN grains incorporated in an amorphous $SiN_{1.3}$ matrix were modeled by a sum of Drude and Lorentz (interband) transitions. Optical properties of the films were explained by their morphology and chemical structure, investigated by a multitechnique approach using SEM, TEM, ERD–TOF, AES, XPS and Raman spectroscopy. Subsequent addition of Si to TiN caused a complex transformation from a polycrystalline to a nanocomposite microstructure, which adopted a predominantly amorphous character. This was accompanied by a transition from a metallic to a dielectric behavior in terms of the optical response and electronic properties.

5.2. Introduction

In recent years, rapid advancement of new fabrication techniques, process control, vacuum technology, and characterization techniques have stimulated significant progress in the field of hard and protective coatings [1]. Such coatings are applied in different areas of engineering and industry in order to improve the mechanical properties of surfaces [3]. Examples of fields of application are hard, anticorrosive and decorative coatings.

Pure transition metal nitrides provide attractive colors [145-146, 170-172] combined with good mechanical properties [1, 4, 95] as a consequence of mixed covalent and metallic bonding [173-177]. Depending on the particular application of the decorative coatings, the choice depends on their appearance and mechanical performance. The main limitations of the deposition process and film performance are temperature, mechanical stress and adhesion. Stress results from the structure of the deposited material [1, 3] (lattice parameter, gas entrapment, etc), but also from the difference in thermal expansion coefficients between the substrate and the coating. Therefore, low temperature deposition techniques such as PVD (physical vapor deposition) and PECVD (plasma enhanced chemical vapor deposition) are becoming popular. Recently, environmental constraints have become a key issue in the fabrication of decorative coatings; traditional wet deposition technologies appear increasingly unacceptable due to the high cost of recycling the chemicals [22-23].

Due to their excellent mechanical behavior, especially their very high hardness, nanocomposite materials have recently attracted much attention in many research groups [24, 73-74, 111, 118-120, 122, 149-153, 178]. In our previous work [179] we studied the mechanical properties of nanocomposite (nc) $TiN/SiN_{1.3}$ films prepared by PECVD at low (T_s = 300 °C) and higher (T_s = 500 °C) substrate temperatures. We reviewed the methodology of mechanical testing, and in particular, of hardness, *H*. The *H*

measurements were based on depth-sensing indentation and static indentations using different models of data interpretation. The optimum mechanical properties in terms of H, and reduced Young's modulus, E_r, were obtained for a Si concentration, [Si], between 5 and 10 at. %. The nc-TiN/$SiN_{1.3}$ films deposited at low T_s (H ~ 25 GPa, E_r ~ 250 GPa) were compared with those prepared at high T_s (H ~ 45 GPa, E_r ~ 350 GPa). Enhancement of the mechanical characteristics was explained in terms of a structural phenomenological model according to which the nc-TiN/$SiN_{1.3}$ films are formed by TiN particles (5-10 nm in diameter) embedded in an amorphous hydrogenated silicon nitride ($SiN_{1.3}$) matrix in agreement with the results from other groups.

Complementary to the mechanical evaluation of superhard coatings exhibiting highly elastic properties [116], the nondestructive, noncontact optical characterization of such materials appears to be very attractive. In the present work, we first study the effect of adding the $SiN_{1.3}$ matrix material to polycrystalline TiN on the optical response and color of the resulting nc-TiN/$SiN_{1.3}$ films. We then apply a multitechnique characterization approach in order to establish a quantitative relationship between the optical and electrical performance of the films and their microstructure.

5.3. Methodology of film deposition and characterization

5.3.1 Film deposition

The films were deposited in a radio frequency (RF, 13.56 MHz) plasma system in which the substrates were placed on an RF powered electrode (10 cm in diameter) where an RF-induced, negative DC self-bias, V_B, develops. The substrate holder was inductively heated from the backside and by halogen lamps from the front side, up to 500 °C. The flow of the working gases, namely $TiCl_4$, SiH_4, N_2, H_2 and Ar was controlled by MKS and Sierra mass-flow controllers in each line, and the working pressure was measured by a capacitance gauge (MKS Baratron). Prior to the

experiment the system was evacuated to 10^{-5} Torr ($1.33*10^{-3}$ Pa) using a turbomolecular pump.

The choice of the deposition parameters was based on our preliminary optimization in which we obtained the characteristics (*H* and chemical composition) of pure TiN comparable to those reported for PVD films. The film fabrication process consisted of two 10 and 30 minute plasma pretreatment steps in Ar and in N_2, at a pressure of 40 and 300 mTorr (5.3 and 40.0 Pa), respectively. They were followed by a 1 hour deposition with a flow ratio of $TiCl_4$ / N_2 = 9 sccm / 15 sccm at a pressure of 200 mTorr (26.66 Pa). The concentration of the $SiN_{1.3}$ phase in the nc-TiN/$SiN_{1.3}$ was controlled by adjusting the SiH_4 flow between 0 sccm (pure TiN) and 3 sccm. The films were deposited at T_s = 300 °C and T_s = 500 °C, and the thickness, t_f, measured by a Sloan Dektak II profilometer, was between 1.5 and 2.0 μm. Based on our earlier studies of ion fluxes and ion energy distribution functions [36], we estimate that the ion current density during the film growth was about 100 μA/cm^2. High resistivity crystalline silicon, (c-Si) (100), used as a substrate, was cleaned in an ultrasonic bath with acetone and isopropanol to eliminate organic surface contaminants.

5.3.2. Determination of the optical constants

The optical properties, namely the index of refraction, *n*, and the coefficient of extinction, *k*, were assessed by visible and near infrared variable angle spectroscopic ellipsometry (VASE) between 0.7 and 4.45 eV using four angles of incidence (55°, 60°, 65° and 70°). In all cases t_f was more than 100 nm, which is the limiting value for TiN to become optically thick [146] and to avoid any interference effects with the substrate. Ellipsometry measures the change in polarization of incident light upon reflection. This change can be expressed as a complex ratio, $\overline{\phi}$, of the electric field amplitudes of the incident and reflected light in *s* and *p* polarizations:

$$\bar{\phi} = \frac{F_r^p}{F_r^s}\frac{F_i^s}{F_i^p}\exp i(\delta_r - \delta_i) = \tan\Psi \exp i\Delta, \tag{5.1}$$

where F is the electric field amplitude, δ is the phase, and the indices *i, r, s* and *p* indicate the incident and reflected components for *s* and *p* polarizations, respectively. Ψ and Δ are the values directly measured by the ellipsometer. $\bar{\phi}$ was used to determine the optical response of the material in terms of the complex dielectric function $\bar{\varepsilon} = \varepsilon_1 + i\varepsilon_2$ [180]. Knowing the optical response of the film, $\bar{\varepsilon}$ was modeled and fitted [181] as a sum of the Drude (free carrier) and Lorentz (interband) absorptions:

$$\bar{\varepsilon} = \varepsilon_1 + i\varepsilon_2 = \varepsilon_\infty - \frac{A}{E_{photon}^2 + i\Gamma E_{photon}} + \sum_k \frac{A_k}{E_0^2 - E_{photon}^2 - i\Gamma_k E_{photon}}, \tag{5.2}$$

where ε_∞ is a constant representing the contribution of bonded electrons, A is the amplitude of the oscillator, E_{photon} is the photon energy, Γ is the broadening parameter of each oscillator, and E_0 is the center energy of the oscillator.

Since our films were optically thick (1 μm < t_f < 1.5 μm), the ellipsometric model consisted of two layers with fitted thickness values: a Lorentz oscillator layer (containing a series of Lorentz oscillators) and a surface roughness layer. Free carrier absorption was modeled by the Lorentz oscillator centered at E_{photon} = 0 eV. The surface roughness layer was modeled by the effective medium approximation [182], mixing 50 % volume of film bulk material with 50 % volume of void. All parameters of the model were fitted using the Levenberg-Marquardt algorithm. The *n* and *k* values were obtained from $\bar{\varepsilon}$ using the Kramer's-Kroning relations. The resistivity, ρ, is related to $\bar{\varepsilon}$ through the Drude contribution of the ellipsometric model (see Eq. 5.2) that may be written as:

$$\bar{\varepsilon} = \frac{-\hbar^2}{\varepsilon_0 \rho(\tau E_{photon}^2 + i\hbar E_{photon})}, \tag{5.3}$$

where $\hbar$ is Planck's constant, ε_0 is the dielectric constant of vacuum, and τ is the scattering time.

The plasma energy, E_{plasma}, describes the properties of the free electron gas and it is defined as:

$$E_{plasma} = \hbar\omega_p = \hbar\sqrt{\frac{n_e e^2}{\varepsilon_0 m^*}}, \tag{5.4}$$

where ω_p is the plasma frequency, n_e is the density of free electrons, and e and m^* are the charge and the effective mass of an electron, respectively. ω_p divides the visible spectrum into two parts: (i) if $\omega > \omega_p$ and $\varepsilon_1 > 0$, the electromagnetic wave propagates in the layer, (ii) if $\omega < \omega_p$ and $\varepsilon_1 < 0$, the electromagnetic wave is reflected [180]. E_{plasma} was determined by ellipsometry and by specular reflectance, $R_s(E_{photon})$, measurements, using a Perkin-Elmer Lambda 19 spectrophotometer at near normal incidence.

5.3.3. Evaluation of color

The color was evaluated using a spectrophotometer equipped with a standard D65 light source. The scanned range was from 1.5 to 5.0 eV, and the color and gloss were obtained from the $R_s(E_{photon})$ dependence. The results are presented in two color systems: (i) the "physical" *xyY* system, and (ii) the "physiological" *L*a*b** system [139-140, 145-146, 170]. The *xyY* system is considered "physical" and, therefore, less subjective. According to Grassmann's laws [183], each color may be made up with three primary colors: red, green and blue. To obtain the color tristimulus (*X*, *Y*, *Z*), $R_s(E_{photon})$ was multiplied by the color matching functions for a standard CIE 1931 observer, namely $\bar{x}(E_{photon})$, $\bar{y}(E_{photon})$, $\bar{z}(E_{photon})$, respectively, and by the relative spectral power distribution for D65 illuminant, $s(E_{photon})$:

$$X = \sum_{E_{photon}=1.5eV}^{5.0eV} s(E_{photon})\bar{x}(E_{photon})R_s(E_{photon})\Delta\lambda$$

$$Y = \sum_{E_{photon}=1.5eV}^{5eV} s(E_{photon})\bar{y}(E_{photon})R_s(E_{photon})\Delta\lambda \quad , \tag{5.5}$$

$$Z = \sum_{E_{photon}=1.5eV}^{5eV} s(E_{photon})\bar{z}(E_{photon})R_s(E_{photon})\Delta\lambda$$

where $\Delta\lambda$ is the bandwidth. Assigning the quantity of each color to X, Y and Z, we can calculate the CIE (Commission Internationale d'Eclairage) 1931 chromacity in the xyY system. The x, y, z coordinates are calculated by normalizing the values of the tristimulus with respect to 1:

$$\frac{X}{(X+Y+Z)}+\frac{Y}{(X+Y+Z)}+\frac{Z}{(X+Y+Z)}=1 \tag{5.6}$$

This may be re-written as:

$$x + y + z = 1 \tag{5.7}$$

The color triangle allows one to present colors in a more visual way [139]. Assigning one axis to x and one to y, z may be calculated from Eq. 5.7. Y represents luminosity that is a coordinate, which varies from 0 (black) to 100 (white), perpendicular to the xy plane. In the $L^*a^*b^*$ color space, L^* represents the luminosity, a^* represents the green-red axis, and b^* the blue-yellow axis. This color space has been most commonly used for human color perception, and it can be calculated directly from the X, Y, Z tristimulus values:

$$\begin{aligned} L^* &= 116*(Y/Y_n)^{1/3}-16 \\ a^* &= 500*[(X/X_n)^{1/3}-(Y/Y_n)^{1/3}] \\ b^* &= 200*[(Y/Y_n)^{1/3}-(Z/Z_n)^{1/3}] \end{aligned} \tag{5.8}$$

where X_n=95.5, Y_n=100.0, and Z_n=108.9 are the tristimulus values of the reference white achromatic stimulus, and X/X_n, Y/Y_n and $Z/Z_n > 0.00856$ [139].

5.3.4. Structural characterization

The film microstructure was evaluated by scanning electron microscopy (SEM, Philips XL 20) and transmission electron microscopy (TEM, Philips CM 30). Complementary compositional depth profiles were obtained by elastic recoil detection in the time–of-flight regime [142] (ERD–TOF), Auger electron spectroscopy (AES) analysis and X-ray photoelectron spectroscopy (XPS). Raman scattering spectra were obtained using a RM 2000 Renishaw Raman microscope with a grating monochromator and a photon counting detection system. Spectra were recorded from 100 to 1500 cm^{-1} with a 1 cm^{-1} spectral resolution, using a linearly polarized Argon ion laser beam with green light at 514.5 nm. The laser probe was focused onto the sample surface to a spot of 1 μm in diameter with a 100 x microscope objective. The resistivity, ρ, of the films was measured using a four-point probe with steel contacts mechanically pressed onto the surface of the film [184].

5.4. Results and discussion

5.4.1. Optical properties

In the first set of experiments, we studied the optical and electronic properties of the films as a function of Si concentration, [Si], that also determines the volume fraction of the $SiN_{1.3}$ matrix material. Examples of ellipsometric measurements at different angles are presented in Fig. 5.1 for a sample characterized by the highest value of H (45 GPa) corresponding to about 5 at. % of Si. One can observe a good agreement between the Ψ and Δ data directly measured by ellipsometer (experimental) and those fitted with the mixed Drude and Lorentz approaches (generated). Based on this confirmation we apply these two models throughout the rest of this paper.

Examples of the dispersion curves for pure TiN and for nc-TiN/$SiN_{1.3}$ with an optimum and the highest [Si] are presented in Fig. 5.2 for low and high T_s. One can see that adding

$SiN_{1.3}$ to TiN systematically leads to an increase of n and a decrease of k. This trend is characteristic of a transition of the optical properties from their metallic to dielectric character. Pure TiN and the nc-TiN/$SiN_{1.3}$ with a small concentration of Si exhibit typical Drude-like behavior up to about 2.6 eV, an energy coinciding with the onset of the interband transitions [173, 177]. These samples possess a E_{plasma} of about 2.7 and 2.5 eV for low and high T_s, respectively, suggesting the more metallic character of the former one. When the dielectric component is introduced, ε_1 and hence n increase. At higher photon energies, the free carrier characteristics overlap with an increase of the absorptive part, ε_2, and therefore k. This trend is qualitatively similar for samples prepared at both substrate temperatures.

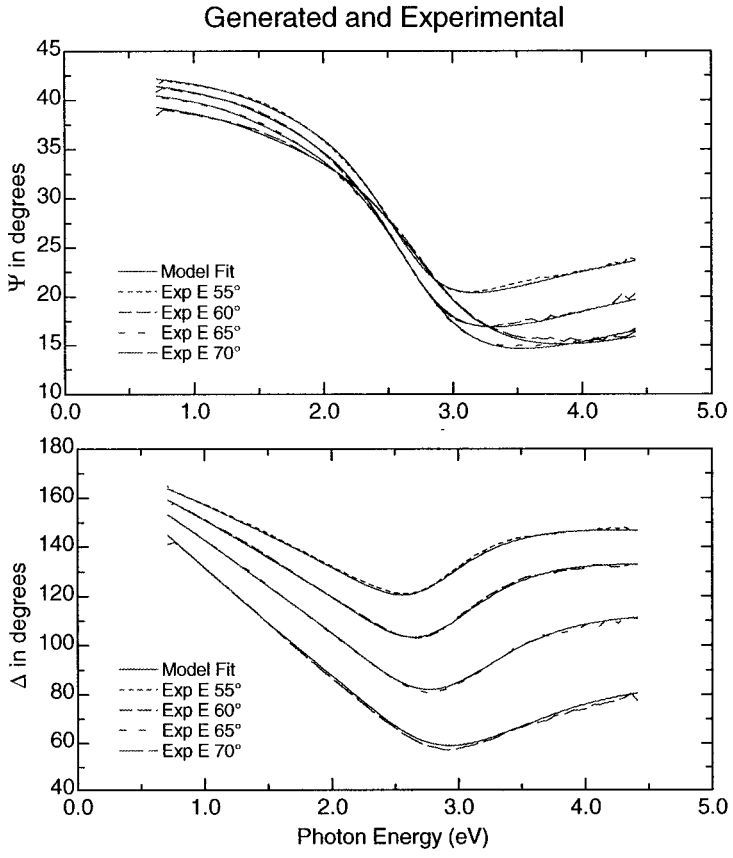

Figure 5.1. *Comparison of generated and experimental ellipsometric angles Ψ and Δ for a sample with [Si] = 5 at. %, prepared at T_s = 500 °C.*

Evolution of the values of n and k at E_{photon} = 2.24 eV (λ = 550 nm) with increasing [Si] is presented in Fig. 5.3. One can see an increase of n from 1.2 up to 2.7 and 2.2 for low and high T_s, respectively, and a decrease of k from 2.2 to 0.4 and 1.4 for low and high T_s, respectively.

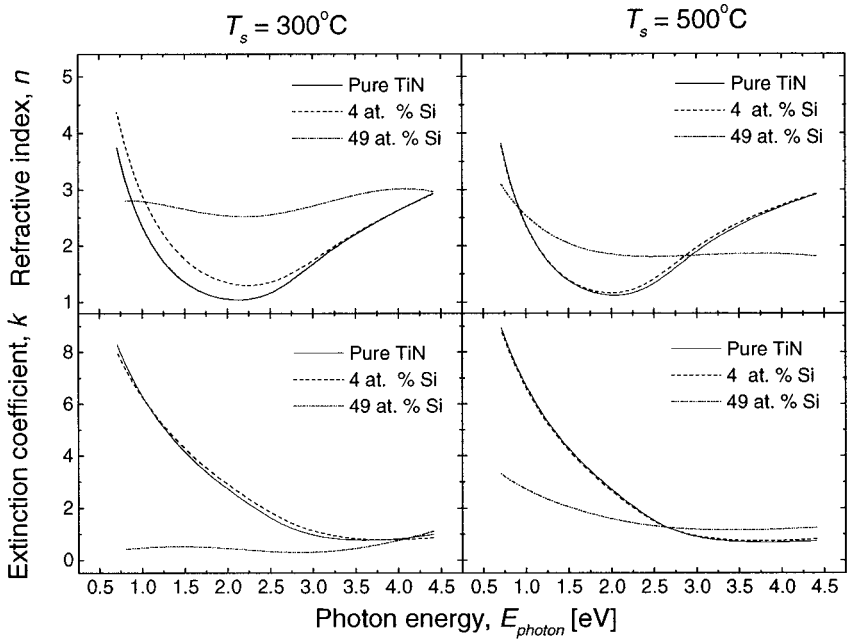

Figure 5.2. *The n and k dispersion curves for pure TiN and nc-TiN/SiN$_{1.3}$ with [Si] = 4 and 49 at. % fabricated at T_s = 300 and 500 °C.*

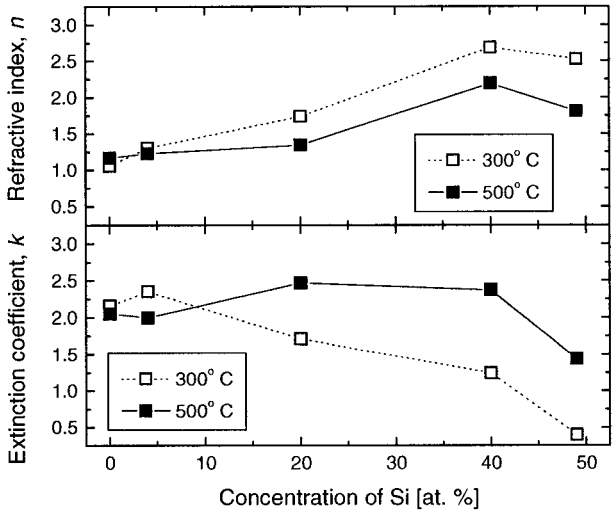

Figure 5.3. *Refractive index, n, and extinction coefficient, k, at 2.24 eV (550 nm) as a function of [Si] for films fabricated at T_s = 300 and 500 °C.*

Transition from a metallic to a dielectric character of the films is illustrated in Fig. 5.4 by the evolution of E_{plasma}. At $E_{photon} = E_{plasma}$, $R_s(E_{photon})$ possesses a minimum. Under the assumption that m^* is constant [185], introducing $SiN_{1.3}$ decreases n_e, and E_{plasma} shifts to lower photon energies, in agreement with Eq. 5.4. E_{plasma} is slightly higher for the material prepared at low T_s, in good agreement with ellipsometric measurements.

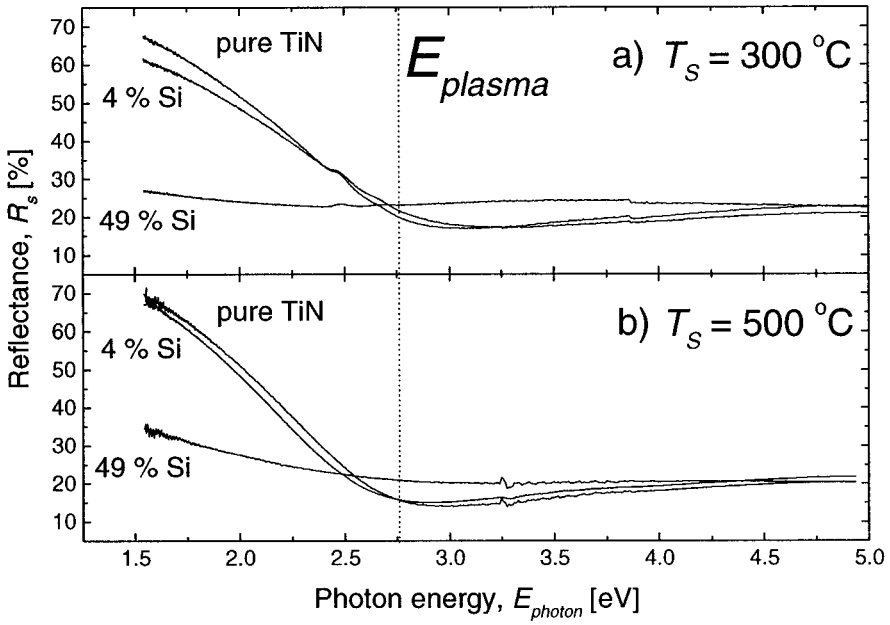

Figure 5.4. *Reflectance spectra for pure TiN and nc-TiN/SiN$_{1.3}$ with [Si] = 4 and 49 at. %, fabricated at T_s = 300 and 500 °C.*

The effect of [Si] on ρ is presented in Fig. 5.5. The metallic character of pure TiN and of the nc-TiN/SiN$_{1.3}$ with the lowest [Si] was confirmed by the low values of ρ, about 70 – 95 μΩcm, in good agreement with other authors [174, 177]. According to the nanocomposite structural model [73-74, 111, 118-120, 149, 151, 178], at higher [Si] (and hence a higher amount of the dielectric SiN$_{1.3}$ phase) the distance between the conductive TiN grains increase. Therefore, the nc-TiN/SiN$_{1.3}$ material prepared at high T_s loses its metallic character, and ρ increases up to about 1000 μΩcm for the highest [Si] (~ 50 at. %). Samples with the highest [Si] (~ 50 at. %) prepared at low T_s did not exhibit Drude–like behavior but rather that of a dielectric, yielding ρ in the range of $7*10^4$ μΩcm. Higher values of ρ for films prepared at T_s = 300 °C coincide with a higher transparency (lower k, see Fig. 5.2) compared to films deposited at T_s = 500 °C.

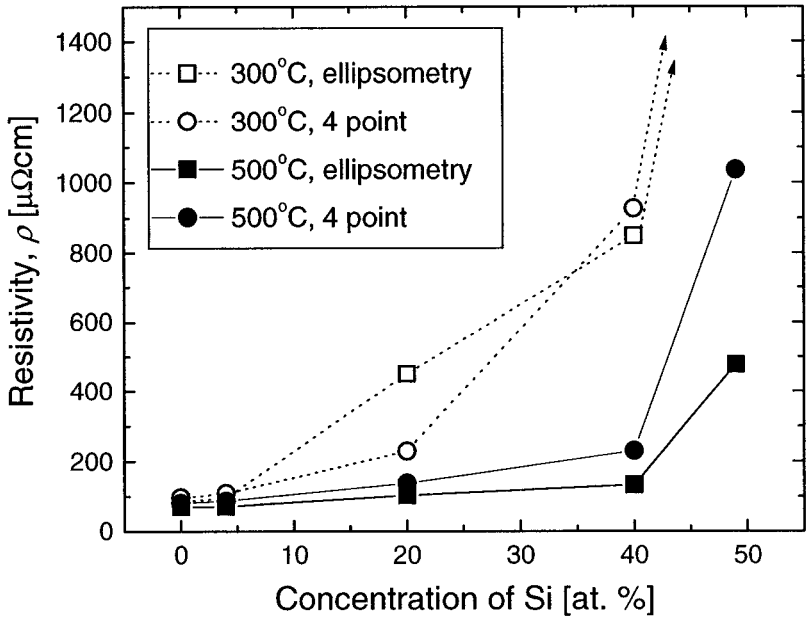

Figure 5.5. *Electrical resistivity as a function of [Si] measured by ellipsometry and by the four-point probe method for films fabricated at T_s = 300 and 500 °C.*

Despite a higher value of n_e, the materials prepared at low T_s possess generally higher ρ (see Fig. 5.5). This can be attributed to the scattering of charge carriers due to a higher defect concentration. Such defects increase the DC value of ρ, but have smaller effect on the optical ellipsometric measurements [177]. Therefore, direct four-point DC measurements result in ρ values systematically higher than the ellipsometric data.

5.4.2. Colors of nc-TiN/SiN$_{1.3}$ coatings

Color characteristics of the nc-TiN/SiN$_{1.3}$ films are presented in Figs. 5.6 – 5.8. Reduction in the reflected light intensity is related to a decrease in luminosity (Fig. 5.6). With an increase of [Si] the nc-TiN/SiN$_{1.3}$ looses its metallic gloss, and the luminosity decreases from about 70 % to 50 % and to 55 % for low and high T_s, respectively. The

color variations are presented in Fig. 5.7 in terms of the *L*a*b** color system, and in Fig. 5.8, in terms of the *xyY* system. In both spaces, one can observe a transition from the gold color of pure TiN to a grayish one as [Si] is increased. Pure TiN films produced at high T_s possess a color that is closer to that of Au than those produced at low T_s. Since in stoichiometric TiN the interband transition occurs at the same energy as for Au (~ 2.6 eV) [186], departure from the corresponding color can be associated with changes in the film composition as will be discussed in the next section.

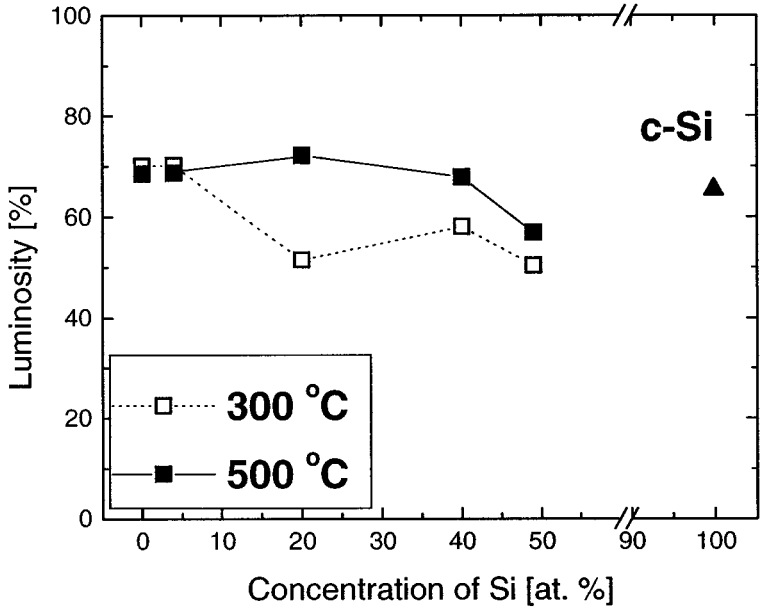

Figure 5.6. *Luminosity as a function of [Si] for pure TiN and nc-TiN/SiN$_{1.3}$ fabricated at T_s = 300 and 500 °C. The value for c-Si is shown for comparison.*

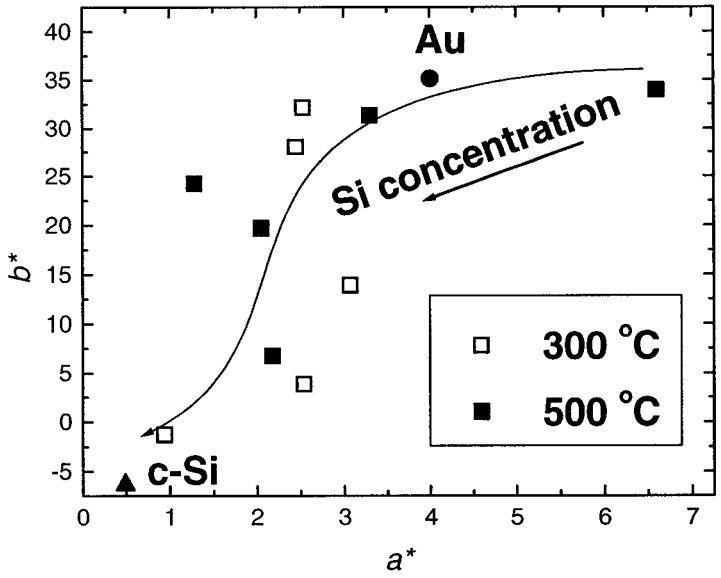

Figure 5.7. *L*a*b* color space for pure TiN and nc-TiN/SiN$_{1.3}$ fabricated at T_s = 300 and 500 °C. Au and c-Si are also shown for comparison.*

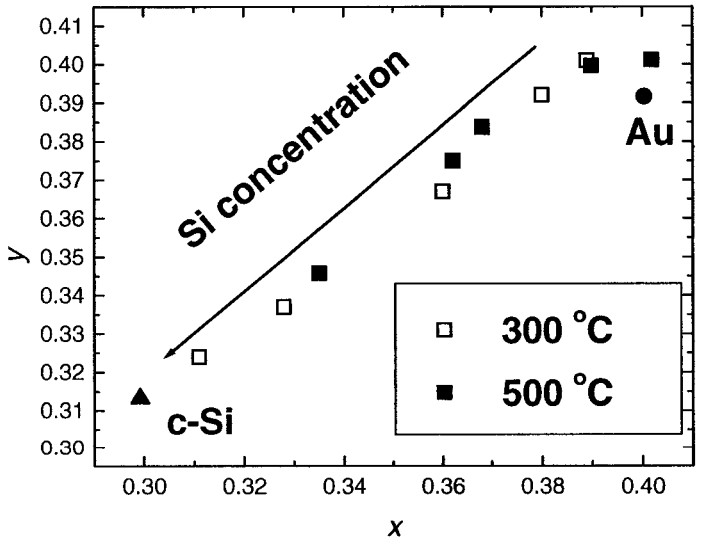

Figure 5.8. *xyY color space for pure TiN and nc-TiN/SiN$_{1.3}$ fabricated at T_s = 300 and 500 °C. Au and c-Si are also shown for comparison.*

5.4.3. Film structure and composition

In the second part of this work, we relate the observed optical characteristics to the changes of the film microstructure. First, the presence of TiN nanocrystals was confirmed by direct TEM observations (see Fig. 5.9), as illustrated by the dark field image from [111] and [200] diffraction rings and the diffraction pattern with indicated TiN phases. The average size of the nanocrystals was estimated between 5 and 10 nm, a result that is in agreement with the findings of other authors [124].

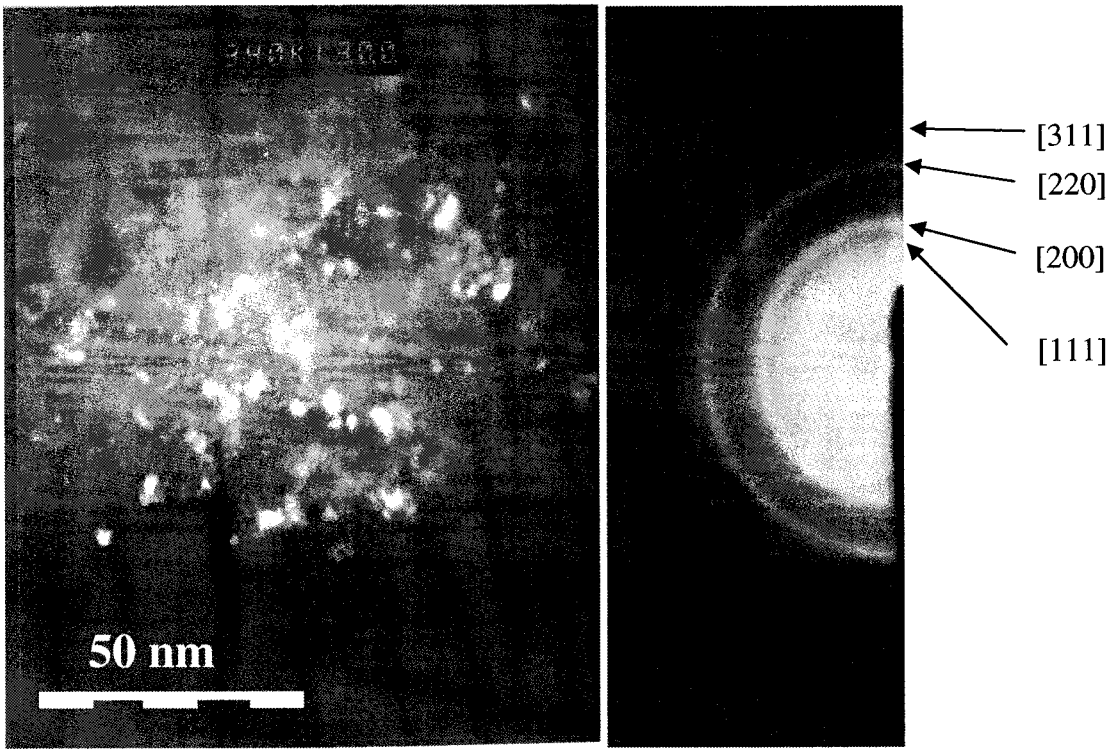

Figure 5.9. *TEM dark field image of nc-TiN/$SiN_{1.3}$ from [111] and [200] diffraction rings and corresponding diffraction pattern.*

Film composition was evaluated by ERD-TOF, AES and XPS. As an example, an ERD-TOF concentration depth profile is shown for pure TiN prepared at low T_s (Fig. 5.10 a) and high T_s (Fig. 5.10 b). The former sample was found to be substoichiometric with

respect to N ([Ti] / [N] ~ 1.1), while near stoichiometry was obtained for the latter one ([Ti] / [N] ~ 1). Lower incorporation of N can be related to a low value of T_s, which is probably insufficient to activate completely the reaction of Ti with N. All samples exhibited good compositional uniformity throughout the layer thickness, with a small amount of oxygen present at the surface. In both cases, we detected less than 3 at. % of Cl and less than 1 at. % of O [179]. XPS analysis (not explicitly shown here) confirmed the presence of silicon and titanium nitrides [179].

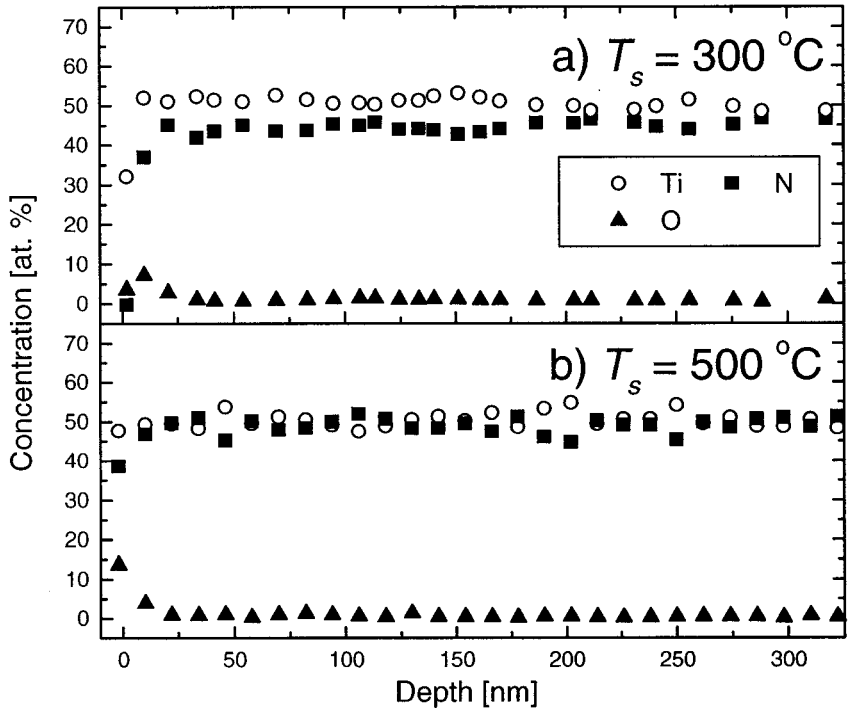

Figure 5.10. *ERD TOF concentration depth profiles through a TiN film deposited at T_s = 300 °C (a) and T_s = 500 °C (b).*

The microstructural evolution was studied by Raman spectroscopy. Fig. 5.11 presents Raman spectra for pure TiN and for the nc-TiN/$SiN_{1.3}$ films with the highest [Si] content deposited at both low and high T_s values. They are characterized by acoustic peaks due to vibrations of the Ti ions and by optical peaks due to vibrations of N ions. The intensity

ratio of these peaks is related to the film stoichiometry [187]. Raman scattering in TiN is due to the defects in the microstructure in the form of Ti and N vacancies. The spectra reveal three broad peaks situated between 100 and 400 cm^{-1}, 400 and 700 cm^{-1}, and around 800 cm^{-1} respectively. According to the assignment described in the literature [187-188] the peak between 100 and 400 cm^{-1} results from the first order transverse acoustic vibrations (TA), centered at about 200 cm^{-1}, and from longitudinal acoustic vibrations (LA), centered at about 300 cm^{-1}. The peak between 400 and 700 cm^{-1} is due to multiphonon TA and LA contributions at about 500 cm^{-1}, a transverse optical (TO) peak between 520 to 580 cm^{-1}, and second order LA vibrations at about 600 cm^{-1}. The broad peak centered at about 800 cm^{-1} is a result of combined multiphonon LA and TO contributions.

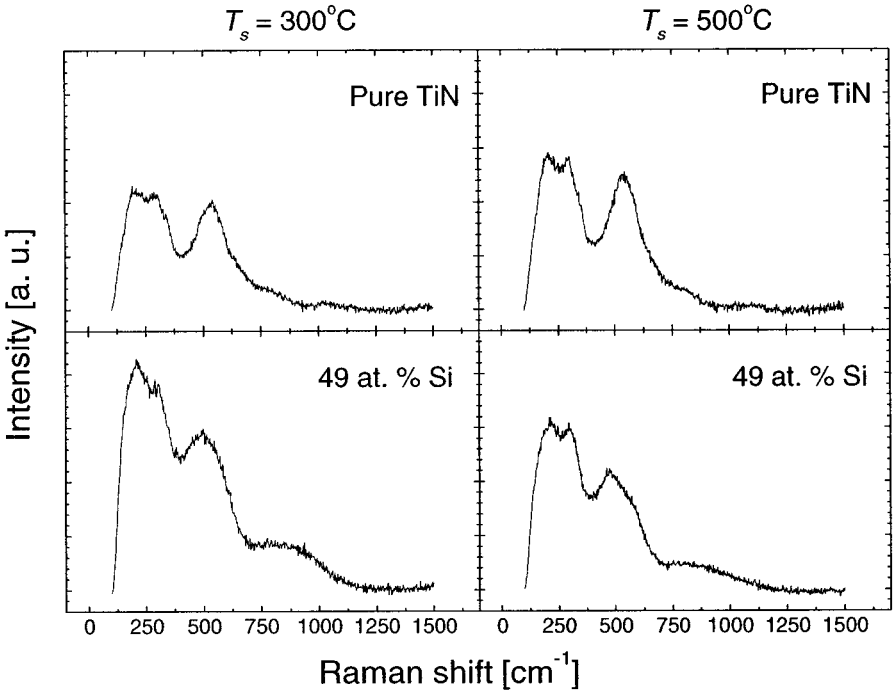

Figure 5.11. *Raman spectra for pure TiN and nc-TiN/$SiN_{1.3}$ with [Si] = 49 at. %, fabricated at T_s = 300 and 500 °C.*

For both T_s values, one can observe that the intensity ratio of the peaks around 200 cm^{-1} to that around 500 cm^{-1} increases when Si is added. Since the first peak is only due to acoustic vibrations and the second one is due to a combination of both acoustic and optical vibrations, this effect clearly coincides with the increase of the [Ti]/[N] atomic ratio. Such substoichiometry is related to the presence of Si that reacts with N forming the $SiN_{1.3}$ matrix. The intensity of the multiphonon peak at 800 cm^{-1} was also observed to increase with increasing [Si].

The shift of E_{plasma} can be explained in terms of an ionic model of TiN [170] that is characterized by a mixture of metallic and covalent bonds. In the TiN molecule, the electron charge is transferred from the Ti ion to the N ion, leaving about one conduction electron per lattice unit. Since the materials produced at low T_s are slightly substoichiometric in N, as confirmed in Figs. 5.10 and 5.11, n_e is higher, and E_{plasma} shifts to higher photon energies.

SEM observations confirmed that introducing $SiN_{1.3}$ suppresses the characteristic columnar growth of TiN [73, 179, 189], as illustrated in Figs. 5.12a and 5.12b. For an optimum [Si] (Figs. 5.12c and 5.12d), for which the highest hardness has also been determined (H ~ 25 and 45 GPa for T_s = 300 °C and 500 °C, respectively) [179], the structure of nc-TiN/$SiN_{1.3}$ possesses suppressed columns. The nc-TiN/$SiN_{1.3}$ produced at low T_s (Fig. 5.12c) possesses a clearly visible texture in the cross section. These features are less pronounced for a sample prepared at high T_s (Fig. 5.12d), suggesting its higher density. Further increase of [Si] causes development of a featureless amorphous structure, as observed in Figs. 5.12e and 5.12f. This effect is in agreement with the structural model [73-74, 111, 118-120, 124, 149, 151, 178, 189], according to which an increase of the amorphous matrix increases the distance between the individual grains.

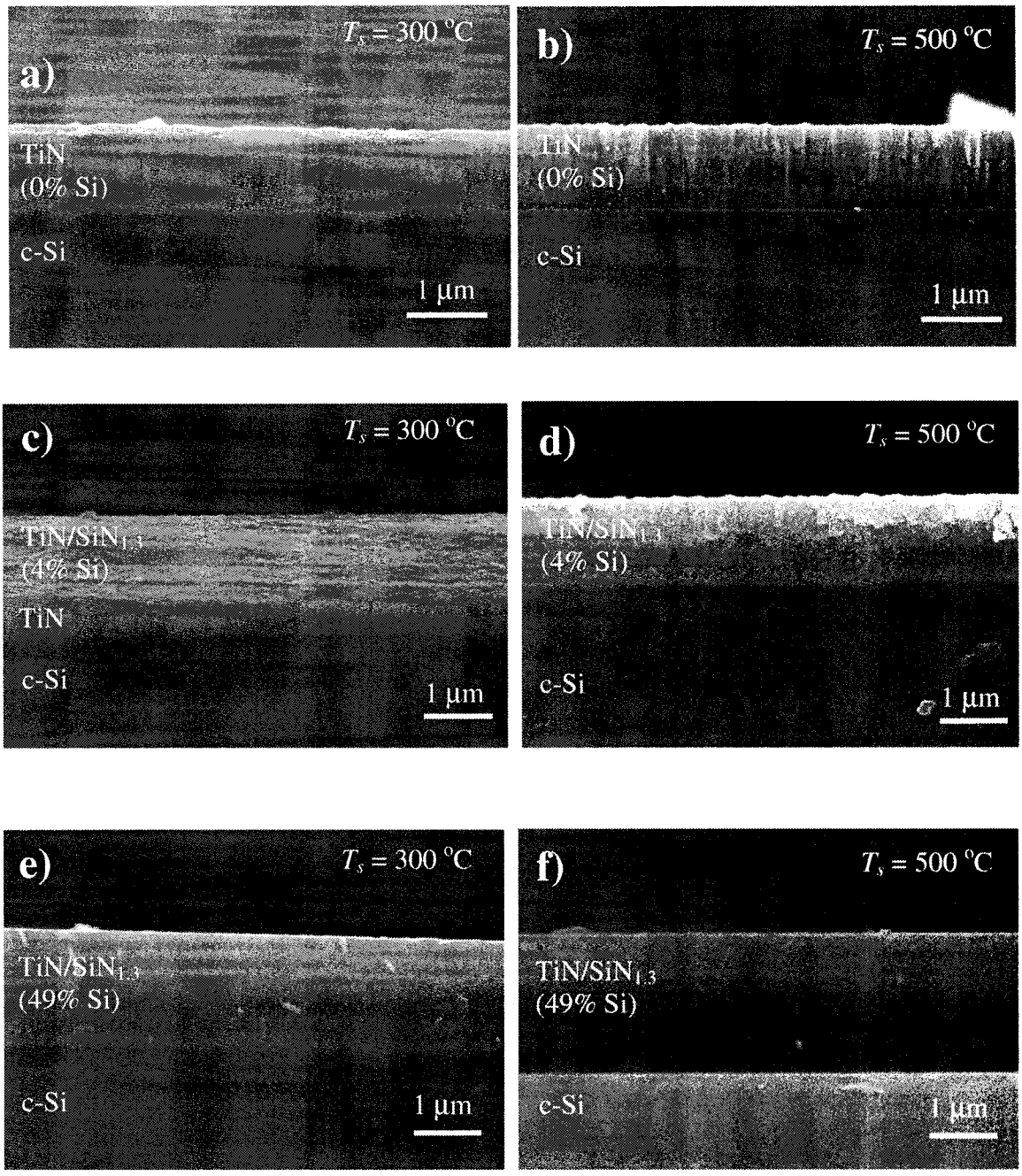

Figure 5.12. *SEM cross section micrographs of films deposited at T_s = 300 °C (a, c, e) and 500 °C (b, d, f) on c-Si substrate: TiN (a, b), nc-TiN/SiN$_{1.3}$ (c, d) with [Si] = 4 at. %, and nc-TiN/SiN$_{1.3}$ (e, f) with [Si] = 49 at. %*

As discussed in earlier papers [73-74] TiN and $SiN_{1.3}$ are immiscible materials and, under specific conditions, form a nanocomposite structure. An increase of [Si] leads to a higher amount of the $SiN_{1.3}$ dielectric phase, an increase of ρ, a decrease of E_{plasma} and a change in $R_s(E_{photon})$, that directly affect the color of the samples. As a result, a smooth transition from a metallic to a dielectric character of the optical and electronic properties can be observed. As shown above, samples produced at low T_s are slightly substoichiometric, and E_{plasma} shifts towards higher values (see Fig. 5.4). Therefore, the colors are shifted accordingly for similar [Si] (see Figs. 5.6 – 5.8).

5.5. Conclusions

In the present work, we studied the structure and optical properties of nc-TiN/$SiN_{1.3}$ films in which the $SiN_{1.3}$ content was systematically varied. The optical constants, electronic properties and colors were measured by ellipsometry and spectrophotometry, and were explained by changes of the microstructure, determined by a multitechnique approach, including SEM, TEM, ERD–TOF, AES, XPS and Raman spectroscopy. Through the control of the film's microstructure, we were able to vary the refractive index at 2.24 eV (550 nm) from 1.2 to 2.7 and 2.2 for low and high T_s, respectively, and the extinction coefficient from 2.2 to 0.4 and 1.4 for low and high T_s, respectively. The resistivity of pure TiN and of the nc-TiN/$SiN_{1.3}$ with an optimum [Si] was about 70 – 95 μΩcm, thus confirming the metallic character of these films. Color changes were quantitatively evaluated and explained by deviations from the stoichiometric TiN and by intra- and interband mixing effects that influence the reflectance characteristics. We surmise that the present results will further stimulate practical implementation of the nc-TiN/$SiN_{1.3}$ films as hard, protective and decorative coatings with controlled optical and electronic characteristics suitable for various technological applications.

Acknowledgements

The authors acknowledge the expert technical assistance of Mr. Jiri Cerny, Mr. J.-P. Masse and Mr. Gilles Jalbert. We also wish to thank Dr. Oleg Zabeida, Dr. Jorg Oberste-Berghaus and other members of the GCM for stimulating discussions. This work was supported by the Natural Sciences and Engineering Research Council (NSERC) of Canada.

Chapter 6. Article 3: Mechanical and Optical Properties of Hard SiCN Coatings prepared by Low Temperature PECVD

Control of the structure of the nanocomposites is key to their excellent mechanical properties and interesting optical behavior. It consists of nanometer size crystalline particles in the amorphous matrix. As we have seen earlier (Section 2.4.3), crack propagation and hence the hardness of nc materials is controlled by the properties and microstructure of the matrix material. To inhibit the growth and propagation of cracks, the distances between individual grains must be very small, possibly in the order of one or two atomic layers. Therefore, the quantity of amorphous material is relatively small what makes it very difficult to analyze. In this context, we study SiCN as a potential candidate for the future TiC_xN_y/SiCN nanocomposite.

Mechanical and Optical Properties of Hard SiCN Coatings prepared by Low Temperature PECVD

P. Jedrzejowski, J. Cizek*, A. Amassian, J.E. Klemberg-Sapieha, J. Vlcek*, and L. Martinu

Groupe des couches minces GCM and Department of Engineering Physics, Ecole Polytechnique, Montreal, Quebec, H3C 3A7 Canada

**Department of Physics, University of West Bohemia, Univerzitni 22, 306 14 Plzen, Czech Republic*

Submitted to: Thin Solid Films (2003), in press.

Keywords: PECVD, SiCN, mechanical properties, spectroscopic ellipsometry, microstructure

6.1. Abstract

Novel amorphous SiCN coatings are becoming increasingly attractive because of their mechanical, optical and electronic properties. In the present work, SiCN films were fabricated by PECVD from $SiH_4/CH_4/N_2/Ar$ gas mixtures at a temperature of 400 ^oC. Mechanical properties such as hardness, Young's modulus, friction coefficient and stress were evaluated, respectively, by depth-sensing indentation, pin-on-disk, micro-scratch and curvature methods. Films deposited under optimized conditions exhibited a hardness > 30 GPa, reduced Young's modulus > 190 GPa, elastic rebound of 85 %, and a compressive stress of about 1 GPa. A friction coefficient against Al_2O_3, ranging from 0.75 to 0.25, and a low surface roughness of about 1 nm were found to be accompanied by a refractive index ranging from 1.85 to 2.10 (at 550 nm) and an extinction coefficient between 1.0×10^{-4} and 4.5×10^{-2}. The film behavior is correlated with the microstructure

and composition determined by SEM, XPS, AFM and broad-range UV-VIS-NIR-IR spectroscopic ellipsometry.

6.2. Introduction

In recent years ternary silicon carbon nitrides (SiCN) have attracted considerable interest due to their exceptional mechanical, tribological, and optical properties. Chemical inertness and high hardness [190-193] make SiCN ceramics a promising option for new micro-electromechanical systems (MEMS) [194]. Good wetting behavior [195], attractive tribological properties [196] and high temperature oxidation resistance [197] offer many other applications in coating technologies. "Tunable" band gap characteristics (band gap engineering) [190, 198-199], adjustable transparency in the visible and IR regions [200-202] and high thermal stability [203] make them attractive for microelectronics and optoelectronics.

SiCN can be formed by combining binary materials, such as $SiN_{1.3}$, SiC, and CN. Each of these three materials provides the following intrinsic property: $SiN_{1.3}$ is a highly transparent, wide band gap (~ 5 eV) dielectric [204-205]. SiC possesses a lower band gap (~ 2.8 eV) and is characterized by excellent mechanical performance [205-206], and CN contributes high hardness, partial electrical conductivity and high elastic rebound [68] due to a fullerene-like microstructure [67]. These three materials form solid solution [207]. Therefore, by changing the phase content and by controlling the short range order it is possible to tune the properties of SiCN films to specific applications. In addition, this ternary material also possesses a complex chemical structure containing Si, C, and N.

SiCN films have been prepared by various techniques, which include: pyrolysis of polymer precursors [197], chemical vapor deposition (CVD) at elevated temperatures [191], bias-assisted hot filament CVD [208], radio frequency plasma-enhanced CVD (PECVD) [209-210], microwave PECVD [211-212], electron cyclotron resonance

PECVD [198-200], pulsed laser deposition [193, 202], ion beam sputtering [192, 213] and reactive magnetron sputtering [195, 214-215].

Although many significant and encouraging results have been reported on ternary SiCN films, optimization of the optical and mechanical performance and microstructure has not yet been fully explored. PECVD technique offers an attractive opportunity to fabricate amorphous hydrogenated SiCN films at intermediate substrate temperatures, and it provides high quality films with good adhesion, good coverage of complicated substrate shapes, and high deposition rate. In the present work we specifically focus on the correlation between process parameters, structure, and mechanical, tribological, and optical properties of these films. Our methodological approach is based on the enhancement of the mechanical properties of $SiN_{1.3}$ by adding CN_x and SiC components in anticipation of obtaining a hard material with a wide band gap and with suitable optical and electronic characteristics.

6.3. Experimental methodology

6.3.1. Film deposition

SiCN films were deposited in a radio frequency (RF, 13.56 MHz) plasma system in which the substrates were held on a RF powered electrode (15 cm in diameter). A RF-induced negative DC self-bias, V_B, developed on the electrode. The substrate holder was heated to 400 ^{o}C using halogen lamps. SiH_4, CH_4, N_2, and Ar working gases were introduced via circular distributors. Their flow was controlled by MKS and Sierra mass-flow controllers in each line, and the working pressure was measured by a capacitance gauge (MKS Baratron). Prior to deposition the system was evacuated to 10^{-5} Torr ($1.33*10^{-3}$ Pa) using a turbomolecular pump.

The film fabrication process consisted of two plasma pretreatment steps in Ar and in N_2 for 10 and 20 min., respectively, followed by a 1.5 hour long deposition using the conditions summarized in Table 6.1. The choice of process parameters resulted from a preliminary optimization study which obtained high quality $SiN_{1.3}$ with respect to its optical and mechanical properties [204]. In all depositions, the conditions were held constant, while the concentration of carbon (C) in $SiN_{1.3}$ was controlled by adjusting the flow of CH_4 (F_{CH4}) between 0 sccm (pure $SiN_{1.3}$) and 60 sccm. Film thickness, measured by a Sloan Dektak II profilometer and a Variable Angle Spectroscopic Ellipsometer (VASE, J. A. Woollam Co.), was between 1.0 and 1.5 μm. Based on our earlier studies of ion fluxes and ion energy distribution functions in the same reactor [36], we estimated that the ion current density during the film growth was about 150 $\mu A/cm^2$. Crystalline silicon (c-Si) (100) was used as substrate, and was cleaned prior to deposition in an ultrasonic bath with acetone and isopropanol to eliminate organic surface contaminants.

Table 6.1. *Deposition conditions for PECVD SiCN films.*

Process	Time [min]	Substrate temperature [°C]	Pressure [mTorr, Pa]	Bias voltage [V]	Gas flow [sccm]			
					Ar	N_2	SiH_4	CH_4
Pretreatment (1)	10	400	50, 6.66	-600	60	---	---	---
Pretreatment (2)	30	400	50, 6.66	-600	10	25	---	---
Deposition of SiCN	90	400	100, 13.33	-600	8	35	5	0-60

6.3.2. Composition characterization

Chemical composition and chemical structure were analyzed, respectively, by X-ray photoelectron spectroscopy (XPS), and infrared variable angle spectroscopic ellipsometry (IR VASE). XPS analysis was carried out in a VG ESCALAB 3 Mark II instrument with a non-monochromated MgK_α source (1256.6 eV) with a 0.8 eV resolution. The IR VASE spectra were measured between 2.5 and 34 μm (i.e. approximately from 4000 to 220 cm^{-1}) using 5 angles of incidence between 65° and 75°. Similar to VIS VASE, these measurements were taken in reflection; therefore, the influence of substrate absorption,

which is a critical factor in standard FTIR spectroscopy, was eliminated. Contrary to FTIR measurements, IR VASE (and ellipsometry in general) did not directly measure the absorption coefficient, α, but it was determined from a simulation of the optical behavior in the IR region. The physical model used for IR VASE data consisted of a c-Si substrate with a native SiO_2 layer, 3 nm thick, a "general oscillator" and a surface roughness layer. In the "general oscillator" model, interband absorptions were simulated by Lorentz-type oscillators; their parameters were found using the Levenberg-Marquardt algorithm during a fitting procedure. In addition, inhomogeneities in the optical constants throughout the film thickness were modeled by "mixing" the optical response of the pure material with voids. Detected inhomogeneities were not larger than 10 %. Film morphology was also assessed by scanning electron microscopy (SEM, Philips XL 20) and by Atomic Force Microscopy (AFM, Digital Instruments, 2 μm x 2 μm scanned surface).

6.3.3. Optical and mechanical properties

The refractive index, n, and extinction coefficient, k, were determined by VASE in the visible (VIS) and near infrared (NIR) regions between 300 and 1600 nm using angles of incidence of 55°, 65° and 75°. The optical data were fitted using the WVASE23 software (J.A. Woollam Co. Inc.) and the same model as for IR VASE.

The hardness, H, and reduced Young's modulus, E_r, were assessed by depth–sensing indentation using a Triboindenter (Hysitron Inc.) equipped with a Berkovich pyramid, and using the Oliver and Pharr [130] method for data analysis. Since the methodology of mechanical testing of very hard films with a pronounced elastic response is controversial, we performed a detailed analysis of the depth-sensing indentation procedure [179]. This included evaluation of the effects of indentation load, depth of penetration and assessment of the indenter area function. The results presented in this work were obtained from 10 indentations using a load ranging from 3 to 10 mN.

Film stress was obtained from the curvature of silicon substrates before and after deposition, using a Sloan DEKTAK II profilometer and the Stoney formula [1]. The stress measurements were performed on silicon wafer stripes which were 30 mm long, 5 mm wide, and 0.3 mm thick. The friction coefficient, μ, at room temperature (~ 25 ^{o}C) and a relative humidity of about 55 % was evaluated using pin-on-disc tribometer and micro-scratch tester (CSEM, Neuchatel). The tribometer was equipped with a 6 mm diameter Al_2O_3 ball. In all experiments the applied load was 0.25 N, and the sliding speed was 10 cm s^{-1}. The values of μ reported here refer to the steady–state conditions. In all cases the traveled distance was greater than 50 m. The micro-scratch tester was equipped with a 200 μm radius Rockwell C diamond stylus. The applied load was 1 N, and μ was measured along a distance of 10 mm.

6.4. Results and discussion

6.4.1. Composition characterization

The results of XPS compositional analysis are shown in Table 6.2. The high-resolution XPS spectra of C 1s and Si 2p core level peaks are presented in Fig. 6.1 and Table 6.3 for pure $SiN_{1.3}$ and SiCN with different F_{CH4}. The Si 2p spectrum for pure $SiN_{1.3}$ showed a presence of Si-N bonds at 101.6 eV and a contribution of Si-O_x bonds at 103.0 eV due to surface contamination. When CH_4 was added the Si-C bond at 100.4 eV appeared. The C 1s spectrum for SiCN was deconvoluted into five components due to C-Si at 283.4 eV, C-C or C-H at 285.0 eV, C-N at 286.0 eV (C-O was also possible), C=N at 287.0 eV (C=O was also possible), and O-C=O at 289.0 eV chemical bonds [216]. The N 1s spectrum at 397.6 - 400.2 eV exhibited a broad peak, difficult to deconvolute due to overlapping of different N- containing groups (not shown here).

Table 6.2. *Elemental composition measured by XPS.*

	Elemental composition [at. %]			
CH_4 flow [sccm]	Si	N	C	O
0	37.1	45.9	9.0	8.0
0.75	30.8	37.6	21.0	10.6
3.5	34.9	28.0	25.6	11.5
7.0	31.2	32.6	27.0	9.2
15	25.1	38.1	28.0	7.8
30	31.0	25.8	31.2	12.0
60	32.0	22.0	35.0	11.0

Table 6.3. *Peak position and area of deconvoluted C 1s and Si 2p peaks for $SiN_{1.3}$ and SiCN.*

	Peak: C1s [eV]					Peak: Si2p [eV]		
CH_4 flow [sccm]	C-Si 283.2 – 283.4	C-C 285.0	C-O C-N 286.0	C=O C=N 287.0	O-C=O 289.0	Si-C 100.4	Si-N 101.6 – 101.8	Si-O 103.0
0		86.0	8.6	2.2	3.2		79.6	20.4
0.75	6.5	71.9	6.6	7.0		11.6	82.1	6.3
3.5	18.7	61.1	10.0	5.4	4.8	24.8	62.2	14.5
7.0	20.9	59.1	12.0	3.0	5.0	35.8	61.3	2.9
15	25.0	47.6	17.8	5.3	4.3	52.3	41.0	6.7
30	28.2	53.7	8.0	4.4	5.7	58.2	37.2	4.6
60	30.2	52.5	7.0	5.1	5.2	62.8	33.8	3.4

Complementary information about the chemical structure was obtained from IR VASE measurements. Examples of deconvoluted absorption spectra for F_{CH4} = 0, 0.75, and 60 sccm are presented in Fig. 6.2. Assignment of the absorption bands was based on literature data [205, 207, 217-222] (see Table 6.4). The IR spectra in Fig. 6.2 revealed the main absorption region between 500 to 1500 cm^{-1} due to the presence of Si-C, Si-H, Si-N, and N-H bonds. The relative intensity of these peaks varied with F_{CH4}. Due to the amorphous structure and a complex short range order chemical environment, the main Si-N absorption peak was relatively large. The Si-C / Si-N ratio increased and the main peak shifted towards lower wavenumbers.

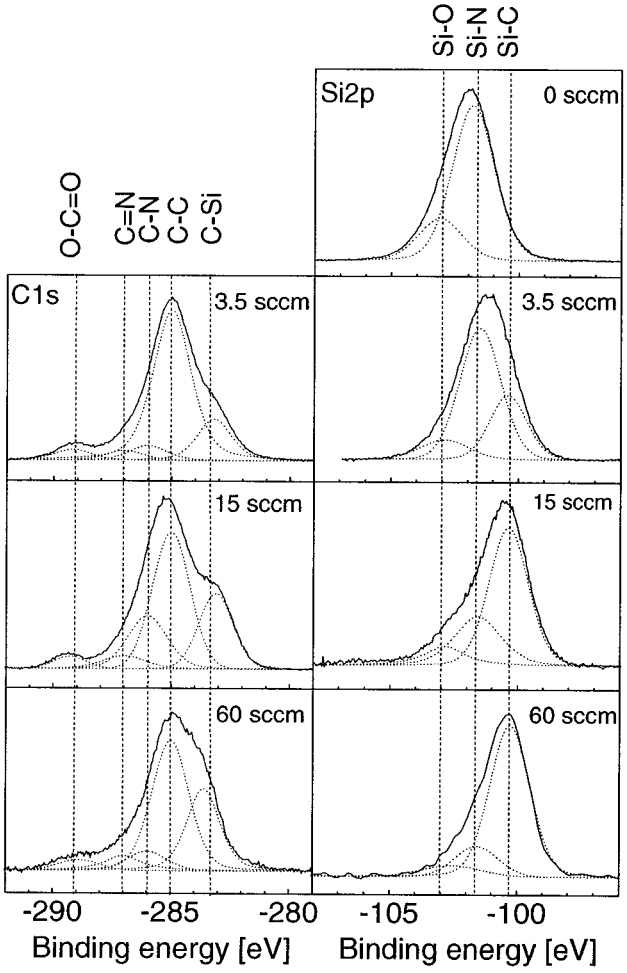

Figure 6.1. *High resolution XPS spectra of C 1s and Si 2p core levels for CH_4 gas flows of 0, 3.5, 15, and 60 sccm.*

Table 6.4. *Position of IR absorption peaks.*

Bonding	Wavenumber [cm^{-1}]
Si-C	~ 800
Si-H	~ 870
Si-N	975 – 990
N-H	~ 1233
C-N	~ 2200
$C-H_x$	~ 2900
N-H	~ 3400

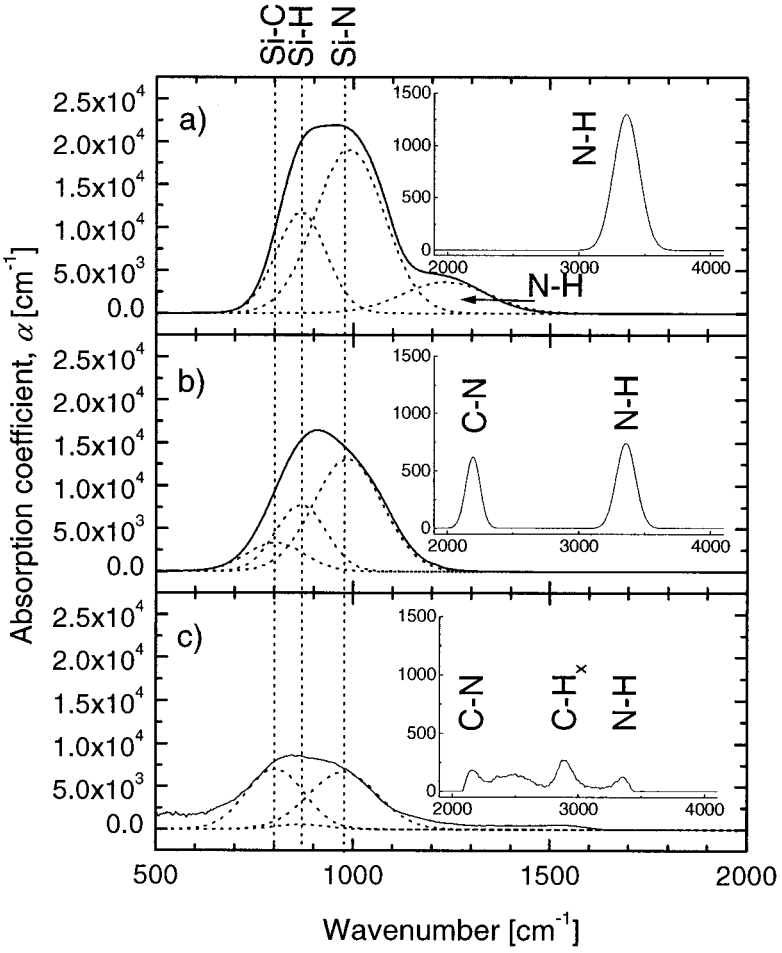

Figure 6.2. *IR spectra obtained by IR VASE for 0 sccm of CH_4 (a), 3.5 sccm of CH_4 (b), and 60 sccm of CH_4 (c).*

The data obtained from the IR VASE and XPS measurements are summarized in Fig. 6.3. The effect of F_{CH4} added to the gas mixture on the surface composition is presented in Table 6.2 and in Fig 6.3a. C content steadily increased, while Si and N content fluctuated with a tendency to decrease. We estimated that at least 9 at. % of C was due to adventitious hydrocarbons, while surface contamination by O was about 8-10 at. %.

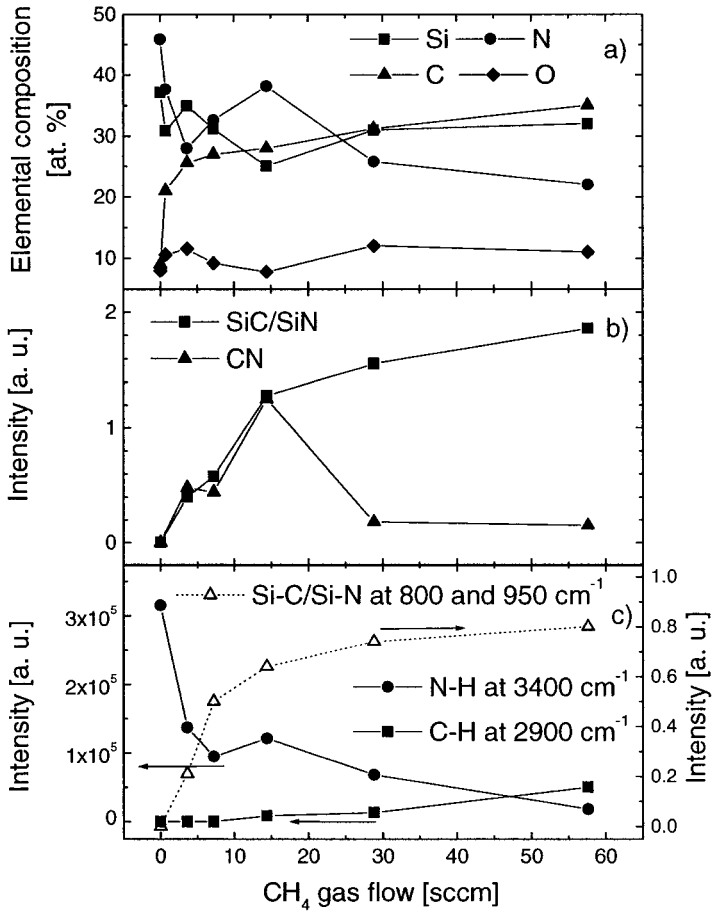

Figure 6.3. *The effect of CH_4 flow on the elemental composition (a), on the peak intensities due to CN bonds and SiC / SiN phase ratio obtained by XPS (b), and on the IR absorption peak intensity for N-H and C-H_x bonds and for the SiC / SiN bond concentrations ratio measured by IR VASE (c).*

Both techniques indicated that increasing F_{CH4} gave rise to a steadily increasing Si-C / Si-N ratio. This suggested that C substituted for N in the chemical structure of SiCN. The CN phase content increased with F_{CH4} up to 15 sccm, but it decreased for higher flow rate values. This was accompanied by an appearance of C-H_x bonds and a steady decrease of

N-H bonds (Fig. 6.3c), indicating that additional carbon contributed to the formation of C-H_x bonds rather than C-N bonds.

All samples studied in this work were found to be amorphous and densely packed as confirmed by the featureless SEM cross-section observations. Direct measurement of the film thickness confirmed the data obtained by VASE. Surface roughness, R_a, was found to be about 1 nm, thus confirming a very smooth surface of PECVD amorphous films.

6.4.2. Optical and mechanical properties

Examples of dispersion curves of SiCN films obtained from VASE measurements in the UV-VIS-NIR regions are shown in Fig. 6.4 for the films deposited with increasing F_{CH4} and hence C. For low F_{CH4} (< 3.5 sccm), the $n(\lambda)$ curves are very similar. For F_{CH4} > 3.5 sccm, n and k increase, an effect which can be attributed to the presence of SiC and CN bonds (n ~ 2.50, 2.60 and 1.85 for SiC, CN, and $SiN_{1.3}$, respectively). The n and k values at λ = 550 nm are shown plotted in Fig. 6.5. The increase of n from 1.85 to 2.10 is accompanied by an increase of k from 10^{-4} to 4 x 10^{-2}. The increase in absorption can be attributed to the presence of carbon that is bonded neither to Si nor to N (as observed by IR VASE).

Fig. 6.6 presents a comparison of the load displacement curves obtained for $SiN_{1.3}$ and for SiCN that exhibits the highest H and E_r values. The shape of the curve clearly points to high elastic properties of the SiCN films. By calculating the ratio of the area below the unloading curve (energy of elastic deformation) to the area between the loading and unloading curves (energy of plastic deformation) we obtain the elastic recovery, R_{el}. For the SiCN curve in Fig. 6.6, R_{el} ~ 85 %.

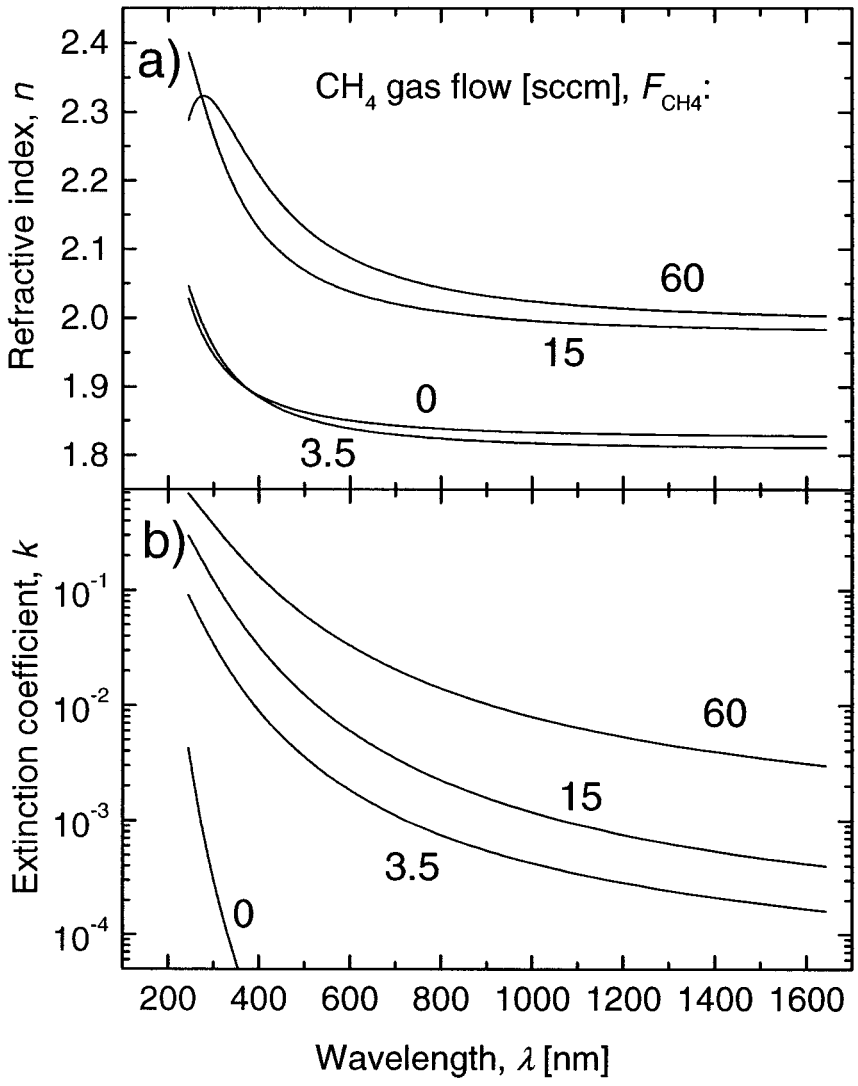

Figure 6.4. *Refractive index (a) and extinction coefficient (b) as a function of CH_4 gas flow.*

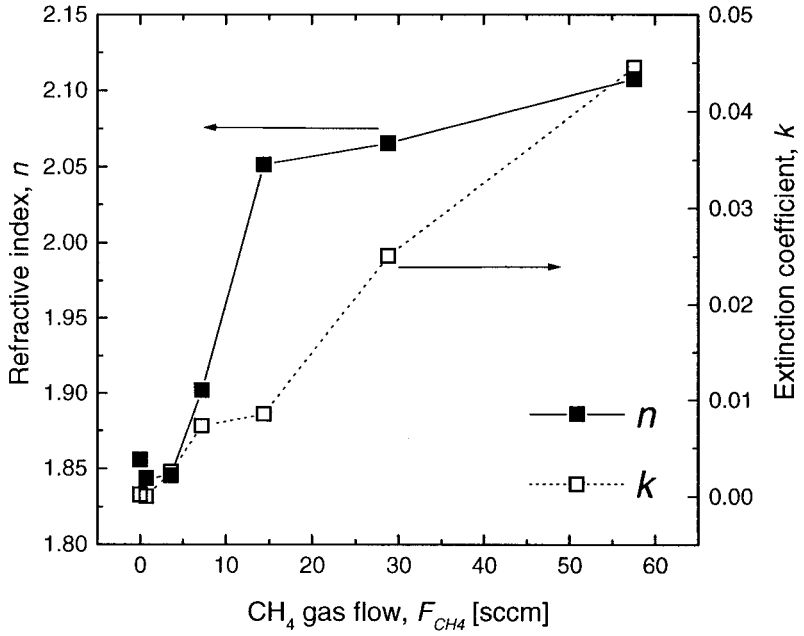

Figure 6.5. *Refractive index and extinction coefficient at 550 nm as a function of CH_4 gas flow.*

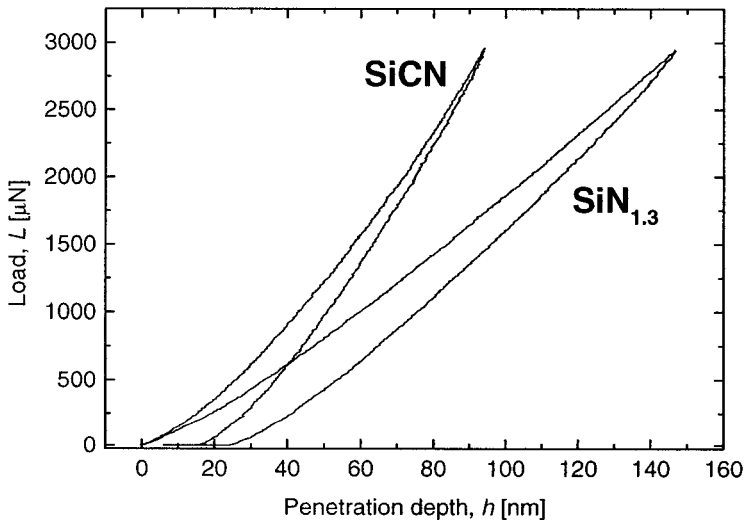

Figure 6.6. *Examples of load-displacement curves for pure $SiN_{1.3}$ and for SiCN with H = 33 GPa.*

The effect of F_{CH4} on the evolution of the mechanical properties is shown in Fig. 6.7. Both H and E_r dependencies (Fig 6.7a) exhibit a similar behavior; they increase with increasing F_{CH4} from 18 and 120 GPa for pure $SiN_{1.3}$, up to 33 and 200 GPa at F_{CH4} = 15 sccm, respectively. Further increase of F_{CH4} leads to a decrease of H and E_r.

In general, SiC and CN are materials possessing high H and E values. They may reach ~ 26, ~ 480 GPa, and ~ 60 and ~ 250 GPa, respectively, for SiC and CN [1, 67]. Adding C to $SiN_{1.3}$ led to the creation of C-Si and C-N bonds and increased both H and E_r to a maximum value at the optimum F_{CH4}. At F_{CH4} = 15 sccm, the phase composition was characterized by the highest amount of CN phase (see Fig. 6.3b). Increase of C beyond this value led to the creation of CH_x groups (see Fig 6.3a), which decreased H and E.

Increasing F_{CH4} led to a monotonic decrease of σ_{tot} from -1.5 GPa to -1.0 GPa, as presented in Fig. 6.7b. In this figure the value of σ_{tot} is the sum of the intrinsic stress, σ_{int}, and the thermal stress, σ_{th} ($\sigma_{tot}=\sigma_{int}+\sigma_{th}$). In order to separate σ_{int}, we calculated σ_{th} by approximating the coefficient of thermal expansion (CTE) for SiCN by the CTE for pure $SiN_{1.3}$ ($3.3*10^{-6}$ K^{-1}) and for the c-Si substrate ($4.1*10^{-6}$ K^{-1}) [1]. In this case σ_{th} was compressive (σ_{th} = -0.1 GPa) and small compared to σ_{tot}. The stress in PECVD films was low compared to their PVD equivalents, for which σ_{tot} > 2 GPa has been reported [223]. This could be attributed to a lower ion bombardment energy and lower ion current intensity during the PECVD deposition process. For a typical RF discharge at about 13 Pa, the Ar^+ ion energies are in the range of 100 eV when using the power levels described in this work [36].

The effect of F_{CH4} on μ is shown plotted in Fig. 6.7c. The values of μ monotonically decreased from 0.75 to 0.25. This could be related to an increasing concentration of C-C bonds that rendered the surface more lubricious [4]. Similar values measured under the same conditions were found for PVD SiCN films for C ranging from 6 to 60 at. % [214].

For comparison, μ measured by the micro-scratch tester using a diamond stylus was found to be very small (between 0.04 and 0.06) and constant with F_{CH4}. This low value clearly resulted from the low friction coefficient of diamond.

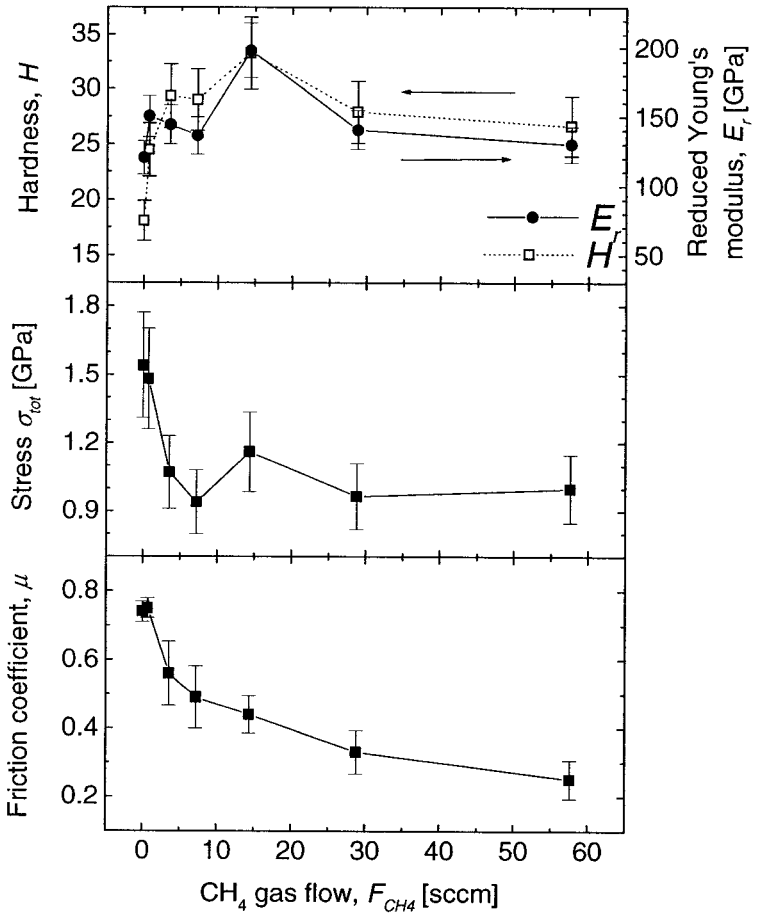

Figure 6.7. *The effect of CH_4 gas flow on the hardness and reduced Young's modulus (a), total compressive stress (b), and the friction coefficient (c).*

6.5. Conclusions

We systematically studied the composition, the mechanical, and optical properties of amorphous SiCN films in which the carbon content was sequentially varied from 0 to 35 at. %. For an optimum F_{CH4} = 15 sccm, that corresponds to 28 at. % of C, we obtained the

highest values of hardness and reduced Young's modulus (33 and 200 GPa, respectively). These films were characterized by a high elastic rebound of ~ 85 %, low compressive stress of ~ 1.1 GPa, low surface roughness R_a ~ 1 nm, and a friction coefficient of 0.4. Through the control of the film's composition we were able to vary the refractive index and the extinction coefficient (at 550 nm) from 1.85 to 2.10 and from 1.0 x 10^{-4} to 4.5 x 10^{-2}, respectively. The "optimum" properties correspond to a composition of 25 at. % Si, 38 at. % N, and 28 at. % C associated with the SiN, CN and SiC bonding as determined by XPS, and broad range UV-VIS-NIR-IR spectroscopic ellipsometry. Future work will be directed to the implementation of SiCN in the thin film systems for electronic, optoelectronic and tribo-mechanical devices.

Acknowledgements

The authors acknowledge the expert technical assistance of Mr. Jiri Cerny and Mr. Gilles Jalbert. We also wish to thank Dr. Oleg Zabeida, Dr. Jorg Oberste-Berghaus and other members of the GCM for stimulating discussions. This work was supported by the Natural Sciences and Engineering Research Council (NSERC) of Canada and by the Ministry of Education of the Czech Republic (Project No. MSM 235200002).

Chapter 7. Article 4: Quaternary Hard Nanocomposite TiC_xN_y/SiCN Coatings Prepared by PECVD

In the previous articles we have thoroughly characterized nc-TiN/$SiN_{1.3}$ materials using a multitechnique approach and we have established the structure – property relationship. Knowing the beneficial influence of C on the SiCN material we fabricated nc-TiC_xN_y/SiCN coatings by addition of CH_4 to the working gas mixture. In this way we synthesized a new nc material that has not been studied before. This nc benefits from the higher strength of the SiCN matrix, giving rise to a very high hardness of up to 55 GPa. The improved mechanical properties of the resulting material were explained by the change of their structure. We determined an interesting effect of C on the characteristics of the nanoparticles and on the matrix. In addition, the optical properties and the color were quantitatively evaluated.

Quaternary Hard Nanocomposite TiC_xN_y/SiCN Coatings Prepared by PECVD

P. Jedrzejowski, J.E. Klemberg-Sapieha and L. Martinu
Regroupement québecois sur les matériaux de pointe (RQMP)
and Department of Engineering Physics,
Ecole Polytechnique, Montreal, Quebec, H3C 3A7 Canada

Submitted to: Thin Solid Films on 4/11/2003

Keywords: nanocomposites, microstructure, PECVD, mechanical and tribological properties

7.1. Abstract

Individual hard thin film materials such as TiN, $SiN_{1.3}$, SiC and CN_x exhibit attractive mechanical, tribological, optical and electronic properties related to their microstructure and chemical bonding. In the present work we combine the characteristics of such materials, while systematically studying quaternary thin films prepared by plasma enhanced chemical vapor deposition (PECVD) from $TiCl_4/SiH_4/N_2/CH_4$ mixtures with different concentrations of CH_4. Detailed structural and chemical characterizations using TEM, XRD, XPS, and ERD suggest formation of a TiC_xN_y/SiCN nanocomposite structure. Depth-sensing indentation, static indentation and curvature measurements, on samples prepared under optimal conditions, reveal a hardness of 55 GPa, reduced Young's modulus of 306 GPa, a compressive stress of 2.0 GPa, an elastic rebound of more than 80 %, H^3/E_r^2 coefficient of 1.8 GPa, and a high toughness. The friction coefficient and the wear rate, measured against diamond, are 0.13 and $12*10^{-6}$ mm^3/Nm, respectively. We compare the properties of the present TiC_xN_y/SiCN coatings with the performance of PECVD films from our earlier studies: these include TiN/$SiN_{1.3}$

nanocomposites and SiCN, for which we obtained a hardness of 43 GPa and 33 GPa, and a reduced Young's modulus of 350 GPa and 200 GPa, respectively.

7.2. Introduction

There has been an increasing interest in hard tribological coatings with tailored functional characteristics such as low surface friction, thermal and oxidation stability, wear- and abrasion resistance, controlled color, biocompatibility, and many others [3-4]. Significant progress in this area has been made due to the advancement of the film fabrication technologies, in particular physical vapor deposition (PVD) and chemical vapor deposition (CVD), as well as the characterization techniques [1].

Hard and protective coatings that have gained industrial popularity are based on ionic oxides, such as Al_2O_3, ZrO_2, covalently bonded carbon and boron compounds, and refractory transition metal carbides and nitrides, especially TiN, TiC and TiCN [1, 3-4]. The properties of the latter group of materials have been significantly enhanced by alloying with other elements such as Al, Si, Mo, and B, that allows one to further improve hardness, wear resistance and friction [24]. Further progress in this area is based on the nanoengineering approach, first suggested by Koehler [71], that deals with 2-dimensional superlattice structures consisting of a sequence of thin, several nanometer thick layers [72, 100, 104, 148]. Later, 3-dimensional, nanocomposite structures have been proposed and tested [73, 111-114, 120, 122, 149-150, 153].

Nanocomposite systems are formed by small, nanometer-size grains embedded in the matrix of a polycrystalline or amorphous material. Their particular advantage is that they are isotropic and, therefore, less sensitive to thickness non-uniformity, in contrast to inherently important thickness control in superlattice structures. This aspect becomes particularly important when such coatings are applied to three dimensional objects [224]. In both types of materials, high density of boundaries between layers (superlattices) and

between the grains and the matrix (nanocomposites) leads to an increased mechanical resistance.

The $TiN/SiN_{1.3}$ nanocomposite system (nc-$TiN/SiN_{1.3}$) became very attractive due to its excellent mechanical properties, thermal stability [73, 111-113, 120, 149, 179], and appealing colors [225]. Our previous work dealt with the methodology of mechanical testing, comparing static and dynamic indentation methods. We evaluated the optical properties and structure-property relationships in hard and superhard (> 40 GPa) nc-$TiN/SiN_{1.3}$ coatings fabricated by radio frequency plasma enhanced chemical vapor deposition (RF-PECVD) [179, 225]. We pointed out that the PECVD technique offers numerous advantages with respect to traditional PVD and CVD, by benefitting from the ion bombardment effects combined with a chemically active environment. This allows one to employ low substrate temperatures, T_s. Films deposited at optimum conditions yielded high hardness (H ~ 40 GPa) and high reduced Young's modulus (E_r ~ 350 GPa). The corresponding size of the nanoparticles was in the range of 8 nm, and the coatings exhibited a metallic character and attractive colors suitable for decorative applications. In this context, we also studied SiCN as a potential hard matrix material, for which we obtained H and E_r values of 33 and 200 GPa, respectively [226].

In the present work we investigate a new possibility to enhance the materials performance by embedding TiN nanoparticles into a hard matrix of SiCN. By systematically studying the effect of carbon addition to the $TiCl_4/SiH_4/N_2$ precursor mixtures, we show that the resulting microstructure is represented by a nanocomposite system (nc-TiC_xN_y/SiCN) with H and E_r of 55 and 306 GPa, respectively.

7.3. Experimental methodology

7.3.1. Film deposition

The nc-TiC_xN_y/SiCN films were deposited in a radiofrequency (RF, 13.56 MHz) PECVD system in which the substrates were placed on the RF powered substrate holder (10 cm in diameter), where a self-induced DC bias voltage, V_b, develops. The electrode was heated from the front side up to T_s = 500 °C using an infrared heating element. The working gas mixture consisted of $TiCl_4$, SiH_4, CH_4, N_2, H_2, and Ar. Gas flows were adjusted by MKS mass flow controllers in each line. The operating pressure, p, was controlled by a capacitance gauge (MKS Baratron) and a butterfly valve. Before deposition the system was pumped down to 10^{-5} Torr ($1.33*10^{-3}$ Pa) using a turbomolecular pump backed by a rotary pump.

The deposition conditions were based on our previous studies [179, 225], wherein nc-$TiN/SiN_{1.3}$ films with optimum mechanical properties were obtained. The fabrication process consisted of a short, 15 min. surface pretreatment in Ar at V_b = - 600 V and p = 50 mTorr (6.66 Pa). This was followed by a 3 h main deposition process performed at V_b = - 600 V and p = 200 mTorr (26.66 Pa), using a gas mixture of $TiCl_4/N_2/SiH_4$ with a flow ratio of 9 sccm / 15 sccm / 1 sccm. The concentration of C was varied by adjusting the CH_4 gas flow from 0 (Sample 1, nc-$TiN/SiN_{1.3}$) to 20 sccm (Sample 6) as presented in Table I. The film thickness, d, was in the range between 2.7 and 3.3 μm, as determined by profilometry, indicating a deposition rate between 1 and 1.5 μm/h. From our earlier studies of ion fluxes and ion energy distribution functions [36] we estimate that the ion current density during the film growth was about 100 $\mu A/cm^2$ and the average ion bombardment energy was in the range of 100 eV. High resistivity crystalline silicon (c-Si) (100) wafers were used as substrates.

7.3.2. Chemical composition and microstructure

The microstructure and chemical composition of the films was investigated using a multitechnique characterization approach. Chemical composition was assessed by X-ray photoelectron spectroscopy (XPS) using a VG Escalab 3 Mark II instrument with a non-monochromated MgK_α source (1253.6 eV) and a 0.8 eV resolution. Low energy Ar sputtering was used to partially eliminate surface contaminants, especially oxygen. Very mild bombardment conditions were chosen (1.5 keV, 2 $\mu A/cm^2$ for 5 min.) in order to avoid preferential sputtering. Following this treatment, the surface still contained adventitious carbon and about 8 at. % of oxygen. The C1s peak with a binding energy (BE) of 285.0 eV and the Au $4f_{1/2}$ peak at 84.0 eV were used as reference. Complementary compositional depth profiles were obtained by elastic recoil detection in the time-of-flight (ERD-TOF) regime [142]. Transmission electron microscopy (TEM) was performed in a Philips CM 30 instrument, using samples prepared by focused ion beam (FIB). X-ray diffraction (XRD, Philips X'pert) was performed in the grazing angle (0.5^o) geometry using a Cu K_α radiation source.

7.3.3. Mechanical properties

Due to many controversies regarding the evaluation of the micro- and nano-mechanical properties of superhard materials, special attention was devoted to the methodology of measurements of H and E_r. They were assessed by depth-sensing indentation using a Triboindenter (Hysitron Inc.) instrument equipped with a Berkovich pyramidal tip. The experimental data were derived from the load displacement curves using the Oliver and Pharr method [130]. We carefully followed the approach described in the international standard [227], while evaluating the indenter's area function, the effect of penetration depth, and the elastic response of the "superhard" films. The results presented here were obtained from indentations with loads varying from 3 to 10 mN. This range of loads was

chosen to obtain pronounced plastic deformation, and in order to avoid the influence of surface inhomogeneities at small loads. The penetration depth was kept below 0.1 *d*.

Toughness, *T*, was estimated using the static indentation method [2-3] with loads ranging from 2 to 4 N. The length of the resulting cracks, made by the Vickers indenter, was measured using an optical microscope. Total mechanical stress, σ, was obtained from the Stoney formula [3] using the curvature of the substrates before and after deposition. We used silicon strips that were 30 mm long, 5 mm wide and 0.5 mm thick.

The wear rate, *K*, was assessed by the Triboindenter, using a piezoelectric scanner attached to the electrodynamic transducer with the diamond Berkovich tip. The piezoelectric element allowed for planar scanning of the sample surface in a similar way as in a friction force microscopy (FFM) [2]. The wear tests were performed with a load of 100 μN over a 3 x 3 μm^2 scanned surface. In each test 150 passes were carried out. Imaging of the test area was performed with a load of 2 μN over a 10 x 10 μm^2 region. The wear volume was calculated from the profile image of the wear track. The friction coefficient, μ, was measured using the micro scratch tester (MST, CSEM) with a Rockwell C diamond stylus with 200 μm radius that was pulled over a distance of 10 mm at an applied constant load of 1 N [228]. The tests were performed at room temperature and at about 50 % humidity.

7.4. Results and discussion

7.4.1. Chemical composition and microstructure

In the first set of experiments, we performed a detailed study of the chemical composition. The effect of the addition of CH_4 on the overall elemental concentration evaluated by XPS and ERD shown in Table 7.1 and Fig. 7.1. Increasing the flow of CH_4 from 0 sccm (Sample 1) to 20 sccm (Sample 6) caused an increase of [C] from 7 to about

30 at. %, while [N] decreased from about 39 at. % to 18 at. %. At the same time [Ti] and [Si] remained approximately constant, at about 38 - 41 at. % and 4 - 6 at. %, respectively.

Examples of ERD compositional depth profiles (Samples 1 and 3 in Fig. 7.1) confirm a good compositional uniformity. Sample 1 is stoichiometric in TiN, with about 2 at. % of Si that accounts for the amorphous $SiN_{1.3}$ matrix. The hardest film, Sample 3 (as it will be shown below), contains a [Ti] of ~50 at. %, [N] of ~38 at. %, [C] of ~ 9 at. % and [Si] of ~ 2 at. %. These results clearly indicate that addition of carbon mainly contributes to the replacement of nitrogen, as also confirmed by the XPS analysis.

Table 7.1. Surface composition of nc-TiC_xN_y/SiCN films determined by XPS

Sample No.	CH_4 gas flow [sccm]	Ti [at. %]	N [at. %]	Si [at. %]	C [at. %]	O [at. %]	C_{bulk} [at. %]
1	0	40.4	38.6	6.3	6.9	7.8	0.0
2	2	41.8	35.1	4.0	11.2	7.9	3.3
3	5	43.0	28.2	4.2	16.0	8.6	9.1
4	7	40.8	22.9	5.8	21.6	8.9	14.7
5	10	41.2	22.3	5.4	23.0	8.1	16.1
6	20	38.8	17.6	5.2	29.8	8.6	22.9

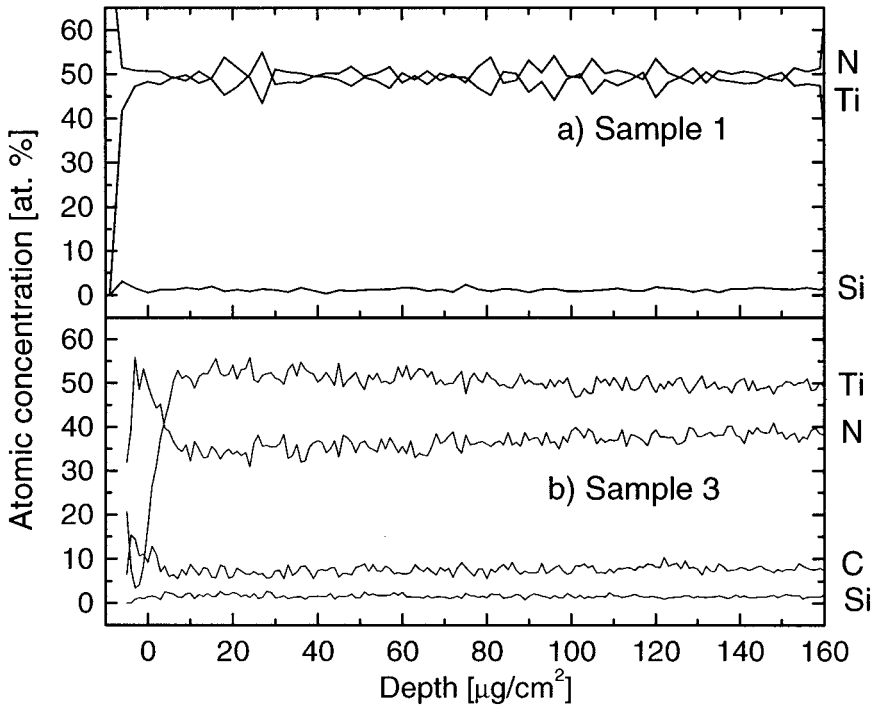

Figure 7.1. *ERD-TOF compositional depth-profiles for Sample 1 (a) and Sample 3 (b) with the highest hardness.*

Both XPS and ERD measurements indicate similar levels of surface contamination due to C and O. For example, the surface [C] in Fig. 7.1 is identical to that cited in Table 7.1 for the same Samples prepared with 0 and 5 sccm of CH_4. We, therefore, assume that about 7 at. % of C in the XPS spectra is due to surface contamination (adventitious carbon). By subtracting this value, we indicate by $[C_{bulk}]$ the carbon concentration in the film bulk, to which we refer in the rest of our article. In addition, we determined about 2 at. % of Cl in the bulk of the films, while [Cl] was very low (~ 0.3 at. %) on the surface as found by XPS.

Additional information of the evolution of the film chemical structure has been obtained from the analysis of high resolution XPS spectra of samples with different $[C_{bulk}]$ values

(see Fig. 7.2) using peak assignments based on literature data [216, 229-232]. The key information can be derived from Si 2p spectra (Fig. 7.2a). For the nc-TiN/$SiN_{1.3}$ film (Sample 1) the main peak at 101.8 eV is due to Si-N bonds. When C is added, Samples 3 and 6 (Fig. 7.2a) also contain Si-C bonds indicated by the features at 100.2 – 100.4 eV. No Si-Ti bonds have been observed for these samples, suggesting phase separation between the TiC_xN_y and SiCN materials. Further increase of C leads to a more complex structure. For $[C_{bulk}] > 15$ at.%, the peak at 98.6 eV indicates formation of Si-Ti bonds [229]. At this moment, the material starts loosing its nanocomposite character. All spectra exhibit a small shoulder at 103.6 eV due to surface oxygen contamination.

The C ls spectrum (Fig. 7.2b) of Sample 1 exhibits of single peak at 285.0 eV due to adventitious carbon. For Samples 3 and 6 the spectrum becomes more complex. We observe broadening on the high energy side due to C-N bonds at ~ 286.0 eV, and a new peak appears at the low energy side. The new peak can be assigned to C-Si (283.0 eV) and C-Ti (281.6 eV) bonds [216, 230]. In Sample 3, the peak position at 282.2 eV suggests a higher concentration of C-Ti bonds than in Sample 6, while the peak position at 282.6 eV indicates a higher amount of C-Si bonds.

The Ti $2p_{3/2}$ peak at 455.1 eV (Fig. 7.2c) agrees well with the published data for pure TiN [231-233]. Addition of C leads to a shift to 454.9 eV for Sample 3, and to 454.6 eV for Sample 6. This shift suggests a presence of Ti-C bonds, while Ti-Si bonds can also contribute for Sample 6 as confirmed by the Si 2p spectrum in Fig. 7.2a.

The N 1s peak is situated between 396.9 eV for Sample 1 and 397.4 eV for Sample 6 (Fig. 7.1d). The shape of the peak is slightly asymmetric with a weak feature on the high energy side presumably due to oxygen contamination. For comparison, the N 1s peak has been reported between 396.5 eV and 397.0 eV for TiN, and between 397.4 eV and 397.8 eV for SiN [216, 231-232].

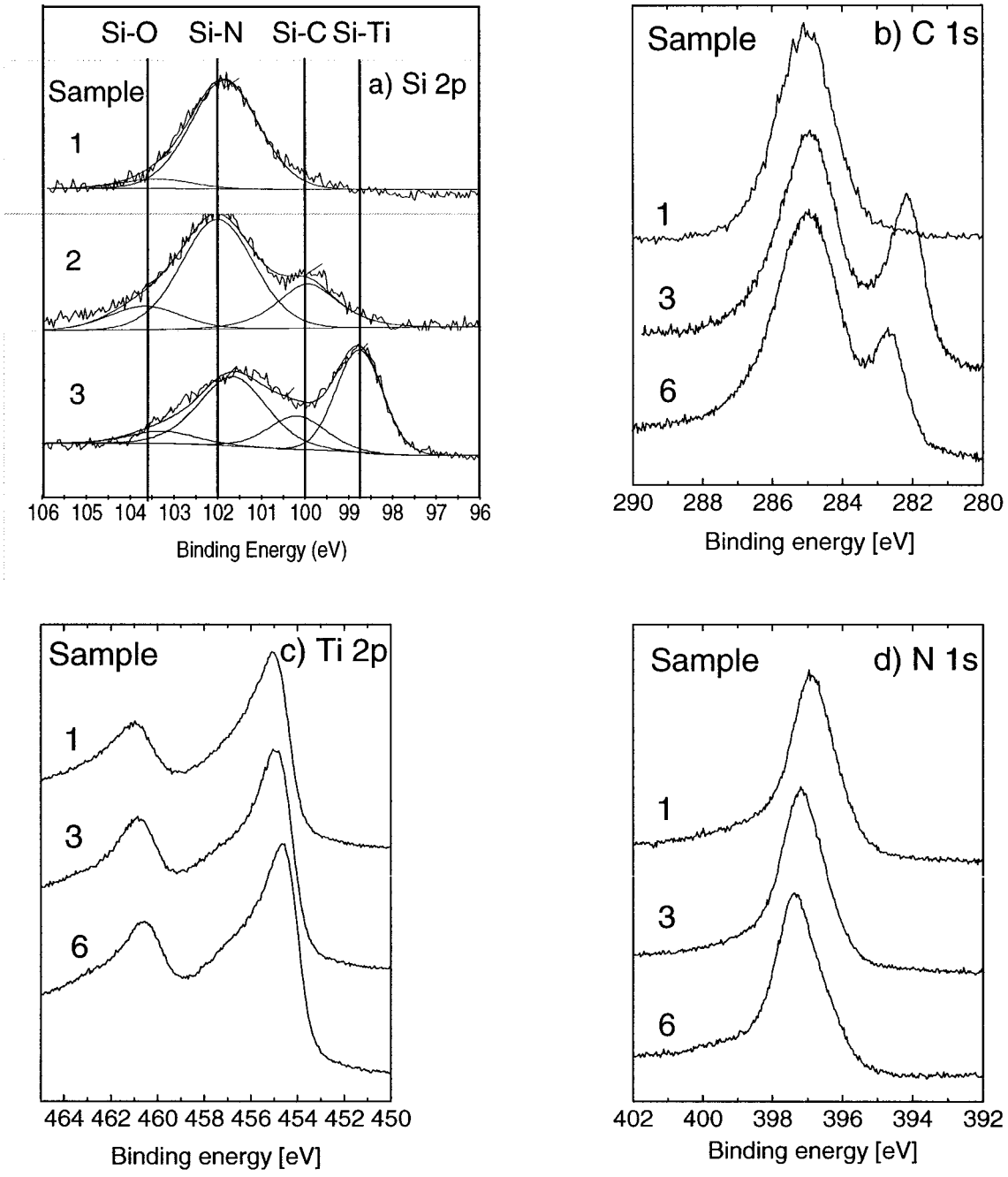

Figure 7.2. *High resolution XPS spectra of the Si 2p (a), C 1s (b), Ti 2p (c), and N 1s (d) peaks for Samples 1, 3 and 6.*

The film microstructure was primarily studied by XRD and TEM. XRD spectra (Fig. 7.3) confirm a crystalline structure of the materials. The vertical lines indicate the strain-free peak positions from the JCPDS powder diffraction database for TiN (full lines) and TiC (dashed lines). Sample 1 (Fig. 7.3a) shows a diffraction pattern characteristic of pure TiN, with [111] and [200] principal orientations, and small peaks due to [220], [311], and [222] orientations. All TiN peaks appear on the low angle side of the strain-free reference material, indicating presence of the compressive stress in the coating. In Samples 2 to 6 we observed the same crystalline orientations, with a systematic shift of the peaks towards lower Θ values. This shift can be attributed to a formation of the TiC crystalline phase which also exhibits very similar lattice parameters.

Sample 3 possesses the highest value of H ($[C_{bulk}]$ = 9.1 at. %), and shows peak positions between those for pure TiC and TiN (Fig. 7.3b), thus pointing to the formation of a complex TiC_xN_y phase. This spectrum is also characterized by an increased ratio of the peaks due to [200] and [111] orientations. The [200] orientation indicates a high density material with a higher H value compared to other crystalline orientations [168]. Using the Scherrer's formula [234] we estimated the grain size to be between 5 and 8 nm.

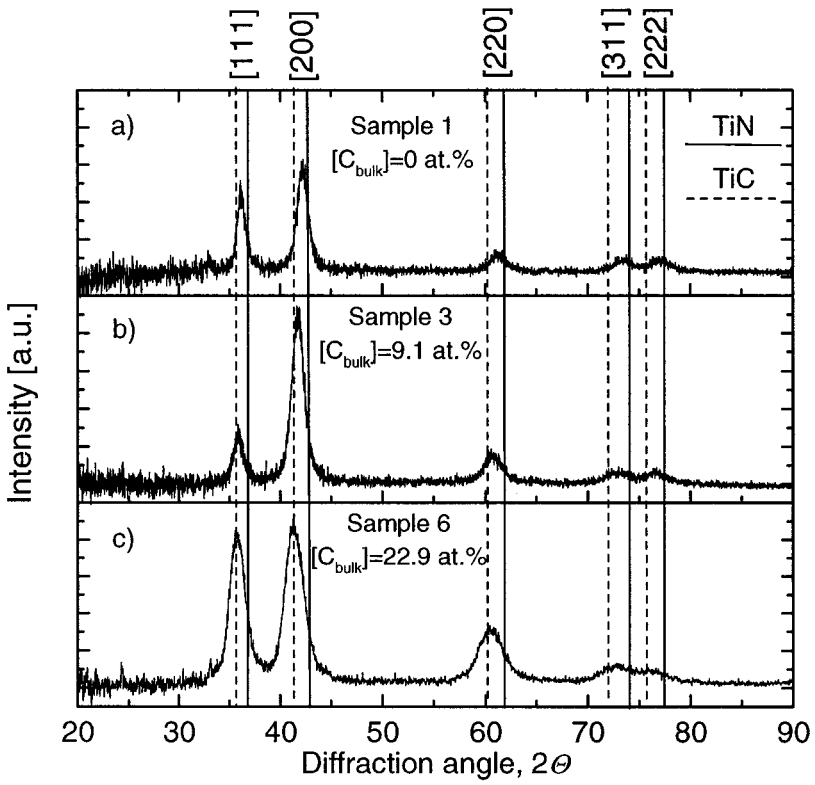

Figure 7.3. *XRD spectra for Sample 1 (a), Sample 3 (b), and for Sample 6 with high carbon concentration (c).*

Sample 6, possessing the highest [C_{bulk}] value of 22.9 at. % (Fig. 7.3c), is characterized in the XRD spectra by a peak position corresponding to TiC, and by a slightly higher FWHM, indicating a smaller grain size (about 4 nm). In this respect, the XRD measurements confirm the effect of C that substitutes N atoms in the NaCl cubic structure of TiN. With the increase of [C_{bulk}], the crystal lattice dimension progressively increases by adding carbon atoms, which possess a larger radius than N, as they are incorporated in the TiN crystal structure.

TEM diffraction patterns also illustrate the presence of the same preferential crystal orientations for both Samples 1 and 3, namely: [111], [200] and [220] (Figs. 7.4a and

7.4b, respectively). Detailed bright and dark field image analyses revealed an average grain size in the range of 10 nm. We therefore conclude that the nc-TiC_xN_y/SiCN material obtained under optimized conditions contains TiC_xN_y nanoparticles incorporated in the SiCN amorphous matrix. Due to small differences between TiC and TiN it is impossible to exclude presence of the latter in this nc material.

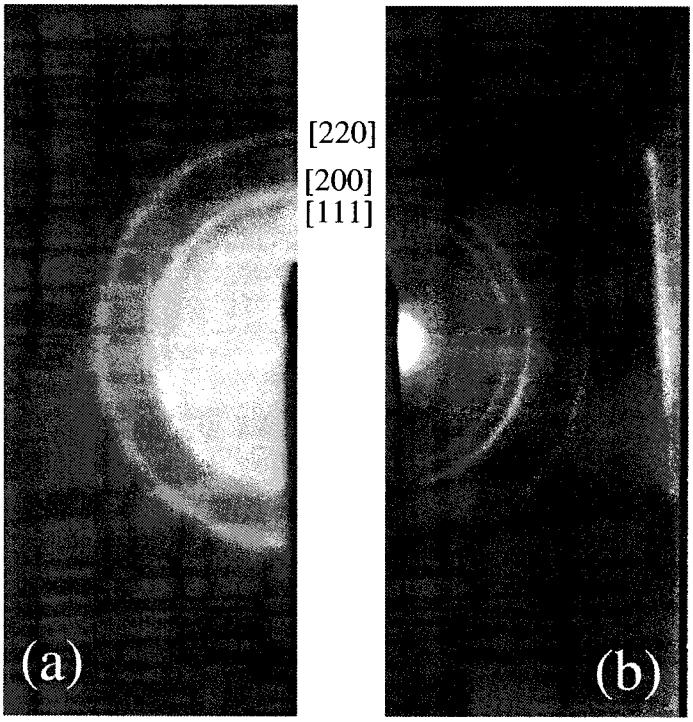

Figure 7.4. *TEM analysis of nanocomposite films: diffraction pattern of Sample 1 (a) and Sample 3 (b).*

TiN and $SiN_{1.3}$ phases are immiscible, as determined by Li Shizhi (up to 40 at. % of Si) [73], and later discussed by Veprek [111, 149]. Therefore, simultaneous deposition of these two materials leads to spontaneous phase separation and formation of a nanocomposite structure, characterized by TiN particles embedded in the matrix of $SiN_{1.3}$. The structure of nc-TiC_xN_y/SiCN containing C is distinct from the previously studied nc-TiN/$SiN_{1.3}$ material prepared under similar conditions. Adding larger amounts of C ($[C_{bulk}] > 15$ at. %) can lead to a mixing the TiC_xN_y and SiCN phases. However, for small amounts of C ($[C_{bulk}] < 15$ at. %) the nanocomposite structure is preserved as

observed by TEM and suggested by XPS, and also confirmed by the mechanical behavior described below.

7.4.2. Mechanical properties

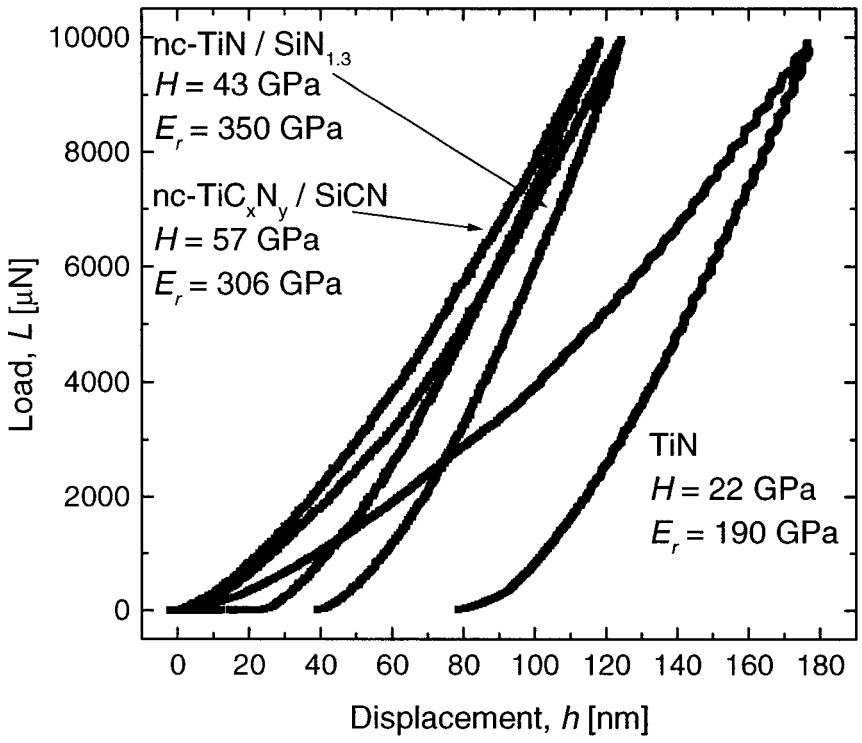

Figure 7.5. *Comparison of load-displacement curves for pure TiN, nc-TiN/SiN$_{1.3}$ (Sample 1) and nc-TiC$_x$N$_y$/SiCN with optimum [C$_{bulk}$] = 9.1 at. % (Sample 3).*

In this part of the work we systematically study the elasto-plastic properties and the tribological behavior of the nc-TiC$_x$N$_y$/SiCN films. Examples of the load-displacement curves for nc-TiC$_x$N$_y$/SiCN are compared in Fig. 7.5 with those for pure TiN and nc-TiN/SiN$_{1.3}$. The former material was found to possess a high H (up to 57 GPa) and a high elastic rebound, R. R represents a ratio of the work of elastic deformation, W_e, and of the total work of indentation, W_{tot}. W_e is defined as the area under the unloading curve, while

W_{tot} corresponds to the area under the loading curve. For the materials presented in Fig. 7.5, R increases from 56 % for pure TiN, to 69% for nc-TiN/$SiN_{1.3}$ (Sample 1), and to 81 % for nc-TiC_xN_y/SiCN (Sample 3). The respective H and E_r values are 22, 43 and 57 GPa, and 190, 350 and 306 GPa. In our earlier work on SiCN films we found that introducing C to the $SiN_{1.3}$ matrix increased R from 80 % to 85 %, H from 18 to 33 GPa, and E_r from 120 to 200 GPa [226].

The H and E_r values for the nc-TiC_xN_y/SiCN films are shown plotted as a function of [C_{bulk}] in Fig. 6. The average value of H increases from 45 GPa for nc-TiN/$SiN_{1.3}$ to about 55 GPa at an optimum value of [C_{bulk}] ~ 9 at. %. For higher concentrations, H is seen to drop rapidly to 29 GPa, a value close to that of pure TiC [3]. At the same time, E_r was found to decrease monotically from about 350 GPa to 200 GPa.

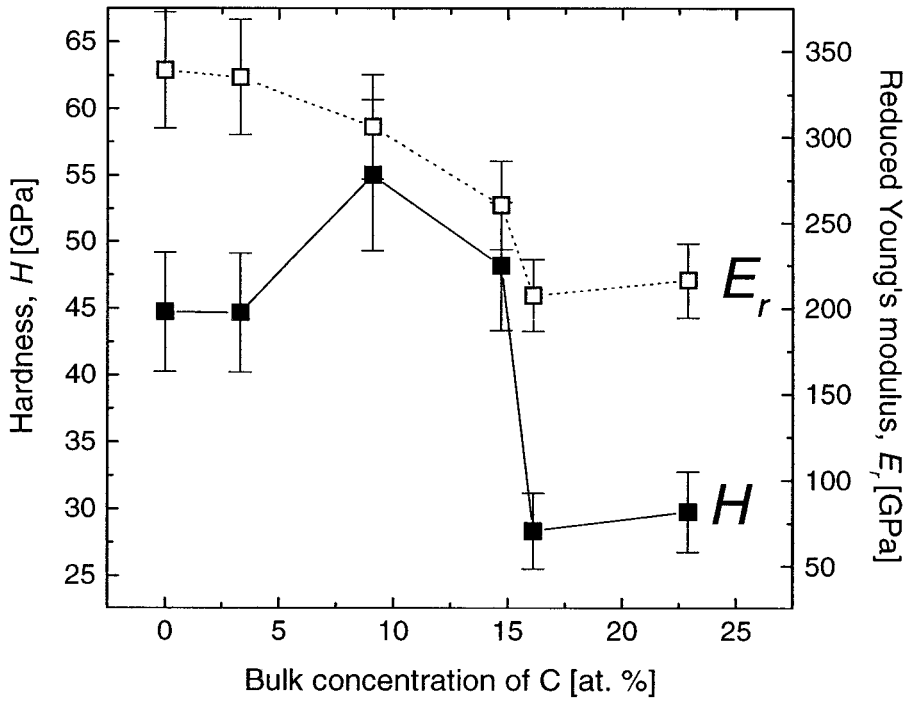

Figure 7.6. *Hardness and reduced Young's modulus of nc-TiC_xN_y/SiCN films as a function of [C_{bulk}].*

The relatively fast decrease of H for [C_{bulk}] above ~ 15 at. % and an overall decrease of E_r can be related to the microstructural evolution described in Section 3.1. For [C_{bulk}] > 15 at. %, the TiC_xN_y and SiCN phases start to mix as documented by the formation of Ti – Si bonds. As a consequence, the boundaries between the nanoparticles and the matrix are probably no longer "abrupt" (or sharp), and the nanocomposite effect is less pronounced.

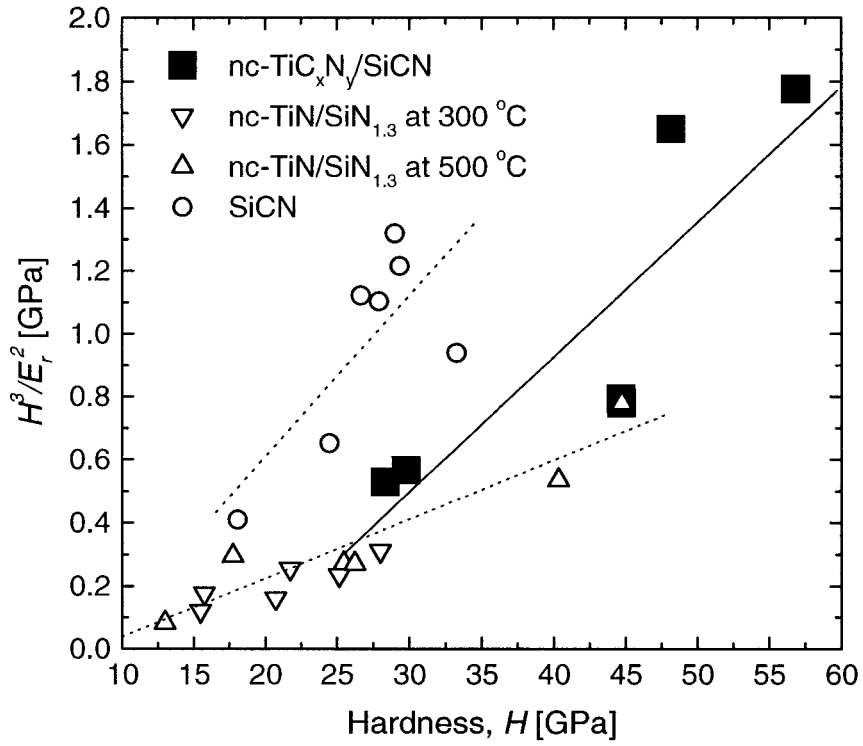

Figure 7.7. *H^3/E_r^2 parameter vs hardness for nc-TiC_xN_y/SiCN, nc-TiN/$SiN_{1.3}$ and SiCN materials.*

In order to increase the resistance to plastic deformation, it is desirable to obtain materials that possess high H but lower E_r values. This behavior is then well expressed by the H^3/E_r^2 ratio [114, 132, 153]. With higher H and lower E_r the plastic deformation is lower, since the external load is distributed over a larger area and the stress distribution is more

uniform. The H^3/E_r^2 ratio for our films is plotted as a function of H in Fig. 7.7. For comparison, our earlier data [179, 226] pertaining to nc-TiN/$SiN_{1.3}$, fabricated at T_s = 300 and 500 °C, and to SiCN are also shown.

nc-TiN/$SiN_{1.3}$ coatings are characterized by a variation of the H^3/E_r^2 parameter from 0.1 to 0.8 GPa. The same range of H^3/E_r^2 was also reported in the literature for the Ti-N-Si nanocomposites, fabricated by PVD [153]. Introducing C and forming nc-TiC_xN_y/SiCN coatings, substantially increases this parameter. In fact, by changing the deposition conditions, H^3/E_r^2 can be varied over a wide range from 0.5 up to 1.8 GPa. As a consequence, this gives one a possibility to design hard coatings with different resistance to plastic deformation. High values of H^3/E_r^2, up to 1.3 GPa, were also found for SiCN [226]. This effect can be related to a lower value of E_r with respect to nanocomposite materials. For comparison values of H^3/E_r^2 for diamond is 0.91 GPa [114].

Toughness, T, describes the material's resistance to crack formation and propagation due to stress concentration in the vicinity of structural imperfections. The average value of T for our nc-TiC_xN_y/SiCN films exhibiting the highest H was estimated to be around 1.0 MPa $m^{0.5}$. Due to the relatively high loads applied to the indenter, this value may be influenced by the substrate. For comparison, our previously investigated TiN and nc-TiN/$SiN_{1.3}$ films, prepared at T_s = 300 °C, were characterized by 1.3 and 1.8 MPa $m^{0.5}$, respectively.

Numerical values of T given in the literature may significantly vary, even for the same material, depending on its structure and measurement method. Generally, materials with high H possess lower T. For example for high speed steel substrate material with H = 9 GPa T varies from 30 to 170 MPa $m^{0.5}$. For Si_3N_4 coating that is characterized by H = 17 GPa, T ~ 4 MPa $m^{0.5}$ [1]. For TiN coating with H = 21 GPa, the reported values of T vary from 4 to 9 MPa $m^{0.5}$ [235]. However, for TiC coating with reported H = 30 GPa, T was found to possess a significantly lower value of 0.46 MPa $m^{0.5}$ [1].

The σ of our nc-TiC_xN_y/SiCN films was found to vary from 2.0 GPa up to 2.5 GPa in compression. The thermal stress, σ_{th}, was estimated in a similar way as described in previous papers [179, 226], and it was found to yield about 0.9 GPa in tension.

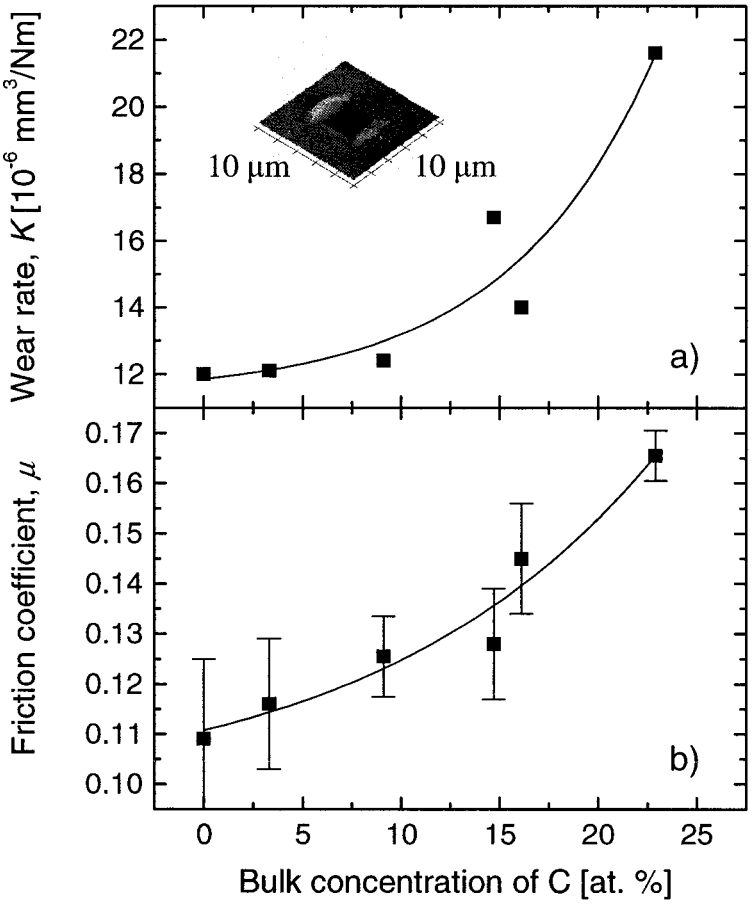

Figure 7.8. *The effect of [C_{bulk}] on the wear rate (a) and the friction coefficient (b) for nc-TiC_xN_y/SiCN films.*

From a practical point of view, the tribological properties of the materials can be well described by the wear rate, K, and the friction coefficient, μ. The evolution of K and μ as a function of [C_{bulk}] is shown in Fig. 7.8. We found that K significantly increased from

about $12*10^{-6}$ mm^3/Nm for the nanocomposite material, and to about $22*10^{-6}$ mm^3/Nm for a single phase material, for which $[C_{bulk}] > 15$ at. % (Fig. 7.8a). This trend can be related to the change of wear mechanism due to the effect of incorporating C in the TiN nanoparticles, and to the formation of less abrupt boundaries as explained in section 7.4.1. Increase of K was found to be correlated with μ that increased from 0.11 to 0.17 (Fig. 7.8b), for the range of $[C_{bulk}]$ investigated in this work.

For comparison, smaller wear rate values were reported for TiN than for TiC [4, 236], similar to the effect of carbon concentration described above. However, the absolute values of K in our measurements are about one order of magnitude higher than those shown elsewhere. The main reason is that different test conditions have been applied: in particular, the Hertzian pressure in our experiments (using a diamond Berkovich indenter) is estimated to be about 30 GPa. This is almost 40 times higher than used in standard pin-on-disk measurements using a steel ball. For the materials used as engineering substrates, such as fused silica, stainless steel and cemented carbides we obtained K values of $13*10^{-6}$, $67*10^{-6}$ and $54*10^{-6}$ mm^3/Nm, respectively.

7.5. Conclusions

In this work, nc-TiC_xN_y/SiCN films were deposited in a RF-PECVD system under ion bombardment. Using a multitechnique characterization approach, we determined that the films present a nanocomposite structure formed by TiC_xN_y particles (about 5 to 10 nm in diameter) incorporated in the SiCN matrix. For $[C_{bulk}]$ above ~ 15 at. %, phase segregation is suppressed, and the individual phases can intermix as documented by the formation of Si-Ti bonds. Such microstructural evolution is closely related to the mechanical behavior of the films. For an optimum carbon concentration ($[C_{bulk}]$ ~ 9.1 at. %) we observed a high hardness of 55 GPa, compared to about 45 GPa for the nc-$TiN/SiN_{1.3}$ films studied earlier. At $[C_{bulk}] > 15$ at. % the H values drop to those comparable with TiC and SiCN (H ~ 25 - 30 GPa).

Nanocomposite films possess high resistance to plastic deformation as documented by a high H^3/E_r^2 parameter. H^3/E_r^2 was found to yield ~ 1.8 GPa for the nc-TiC_xN_y/SiCN system compared to ~ 0.8 GPa for nc-TiN/$SiN_{1.3}$. In addition, the nc-TiC_xN_y/SiCN films are characterized by a reduced Young's modulus of 306 GPa, high elastic rebound (~ 80 %), a toughness of about 1.0 MPa $m^{0.5}$, and a compressive stress of about 2.0 GPa. The corresponding coefficient of friction and wear rate against diamond were found to be 0.13 and $12*10^{-6}$ mm^3/Nm, respectively.

Acknowledgements

The authors would like to acknowledge the technical assistance of Mr. Francis Turcot. We also wish to thank Mr. J.-P. Masse, Dr. Oleg Zabeida and other members of the RQMP for useful discussions, and Mr. Eric Duchesne for FIB experiments. This work was supported by the Natural Sciences and Engineering Research Council (NSERC) of Canada.

7.6. Optical Properties of Quaternary Hard Nanocomposite TiC_xN_y/SiCN Coatings Prepared by PECVD

In this Section we present the results of optical characterization studies of the nc-TiC_xN_y/SiCN coatings described above. Particular emphasis is on the optical constants and color. This subject represents the main part of an oral presentation and of a refereed article being prepared for the International Conference on Metallurgical Coatings and Thin Films (ICMCTF, San Diego, 2004).

7.7. Experimental methodology of optical testing

Optical constants, namely the index of refraction, n, and the extinction coefficient, k, were evaluated using variable angle spectroscopic ellipsometry (VASE, J.A. Woollam Co.) in the photon energy range from E_{photon} = 1.23 to 4.41 eV (1000 – 280 nm) and five incident angles varying from 55° to 75° with an increment of 5°. The optical response of each film was modeled using a free-carrier Drude approach combined with Lorentz interband absorptions. The color and the electronic properties of the coatings were determined from the specular reflectance, R_s, measured at near-normal incidence using a spectrophotometer (Perkin-Elmer Lambda 19). Quantitative results of color measurements are presented here in the xyY color space. A more detailed description of the methodology applied to the ellipsometric model and to color evaluation is given in our previous work on nc-TiN/$SiN_{1.3}$ coatings [225] presented in Chapter 5. Since the nc-TiCN/SiCN films investigated in this work exhibit a similar metal-like behavior, the same approach has been adopted.

The metallic properties of the films were confirmed by the measurements of the resistivity, ρ, using a direct four-point probe method. The results are then compared with the ellipsometric measurements in which ρ was extracted from the Drude component of the film's optical model [138, 237].

7.8. Results and discussion

The sample identification and the chemical composition to which we refer below are shown in Table 7.1 in the first Section of this Chapter.

The dispersion curves $n(E_{photon})$ and $k(E_{photon})$ were obtained from the VASE measurement. They are shown plotted as a function of E_{photon} in Fig. 7.9 for Samples 1, 3 and 6.

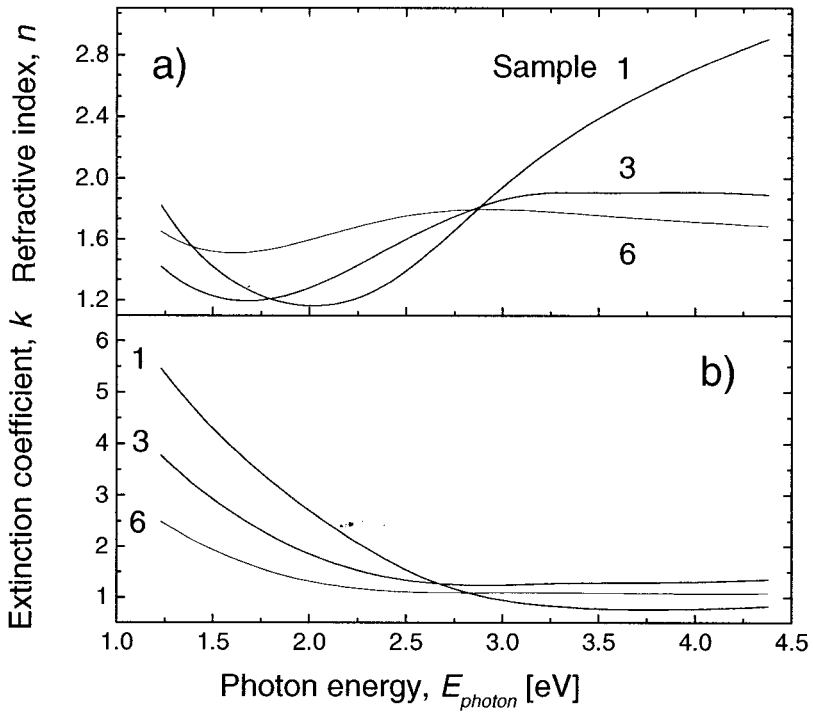

Figure 7.9. *The effect of [C_{bulk}] on the dispersion curves of Samples 1, 3 and 6: (a) refractive index, and (b) extinction coefficient.*

When [C_{bulk}] is increased, n systematically increases (Fig. 7.9a) and k decreases (Fig. 7.9b) in the visible range. This trend is symptomatic of a transition from the metallic

character of the material to a dielectric one. nc-TiN/$SiN_{1.3}$ exhibits a typical Drude behavior up to about 2.6 eV, at which point an interband transition appears. At this energy one can observe a characteristic inflection point in the $n(E_{photon})$ dependence, due to an increase of the real part of the dielectric constant, $\bar{\varepsilon}$, and a decrease of the imaginary part [138]. As [C_{bulk}] rises, the number of free electrons decreases and interband transitions occur. This is accompanied by a decrease of k in the visible region. The values of n and k at 2.24 eV (550 nm) are plotted as a function of [C_{bulk}] in Fig. 7.10. As [C_{bulk}] increases, n increases from about 1.2 to 2.0, and k decreases from 1.7 to 1.2.

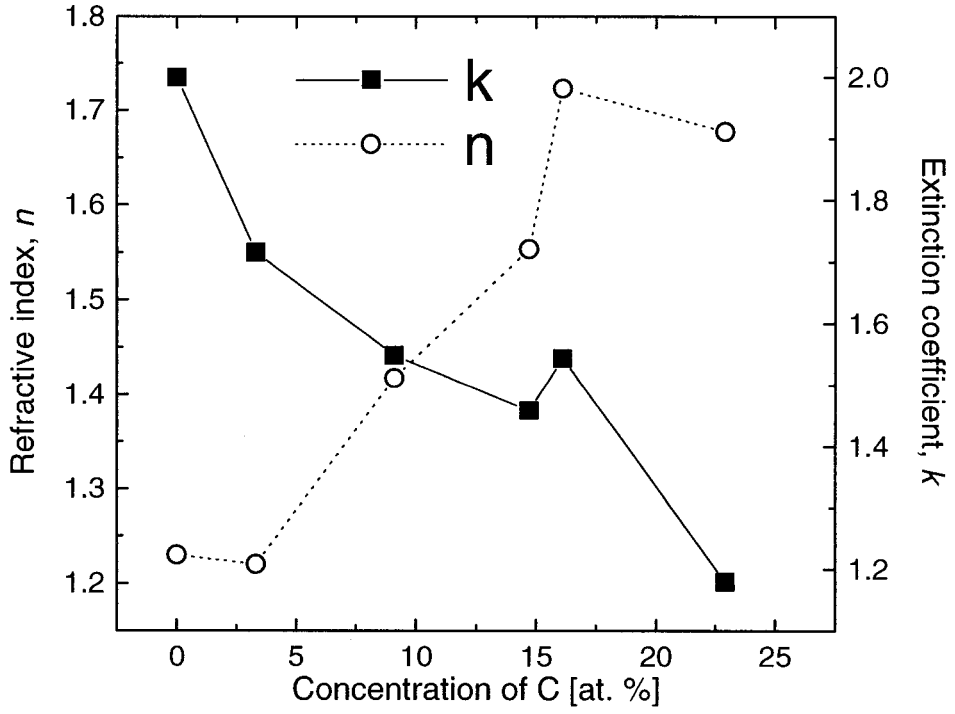

Figure 7.10. *The effect of [C_{bulk}] on the refractive index and extinction coefficient at 2.24 eV (550 nm).*

The transition from a metallic behavior to a dielectric one was confirmed by an increase of ρ. The evolution of ρ determined from both the four-point as well as VASE measurements is presented in Fig. 7.11 as function of [C_{bulk}]. Both techniques show the

same trend. As [C_{bulk}] rises, ρ increases from about 75 μΩcm, characteristic for nc-TiN/$SiN_{1.3}$ and pure TiN [225], to 240 μΩcm, measured by the four-point probe, or 330 μΩcm, measured by ellipsometry. Similar trends were reported in the literature for TiN and TiC. For comparison, different numerical values of ρ have been reported, varying from 20 to 133 μΩcm for TiN and from 120 to 200 μΩcm for TiC [237-238]. These differences are due to impurities, crystal defects or other microstructural imperfections.

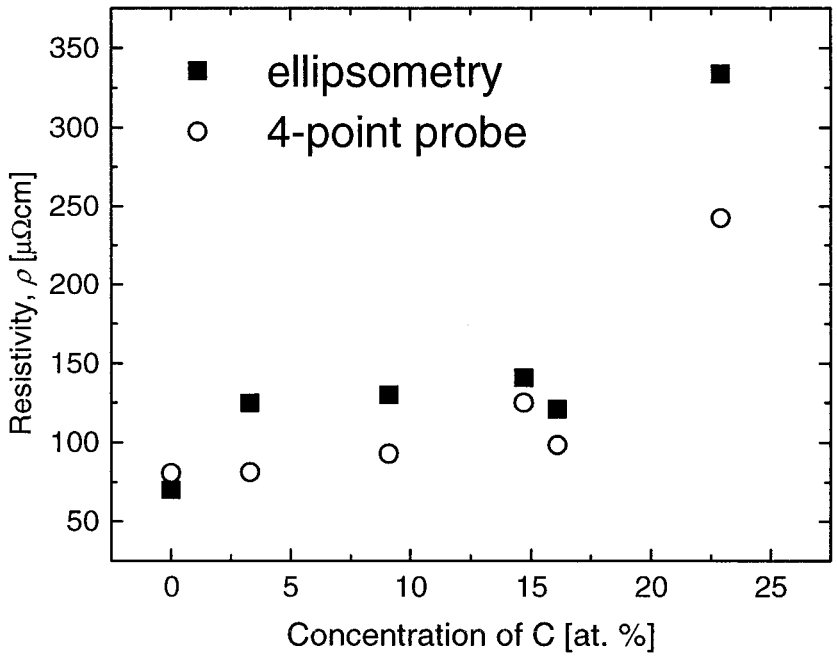

Figure 7.11. *The effect of [C_{bulk}] on the resistivity of nc-TiC_xN_y/SiCN films measured by ellipsometry and by the four-point probe.*

Films investigated in this work possess a dielectric a-SiCN matrix, the presence of which increases the value of ρ compared to pure polycrystalline TiN and TiC materials. N is more electronegative than C; therefore, the Ti-N chemical bond possesses a more ionic character than the Ti-C bond, that is more covalent. This results in a higher free electron density, n_e, in TiN than in TiC, and consequently to a lower value of ρ.

Behavior similar to the one described above was confirmed by detailed R_s measurements. Examples of R_s spectra for Samples 1, 3 and 6 are presented in Fig. 7.12.

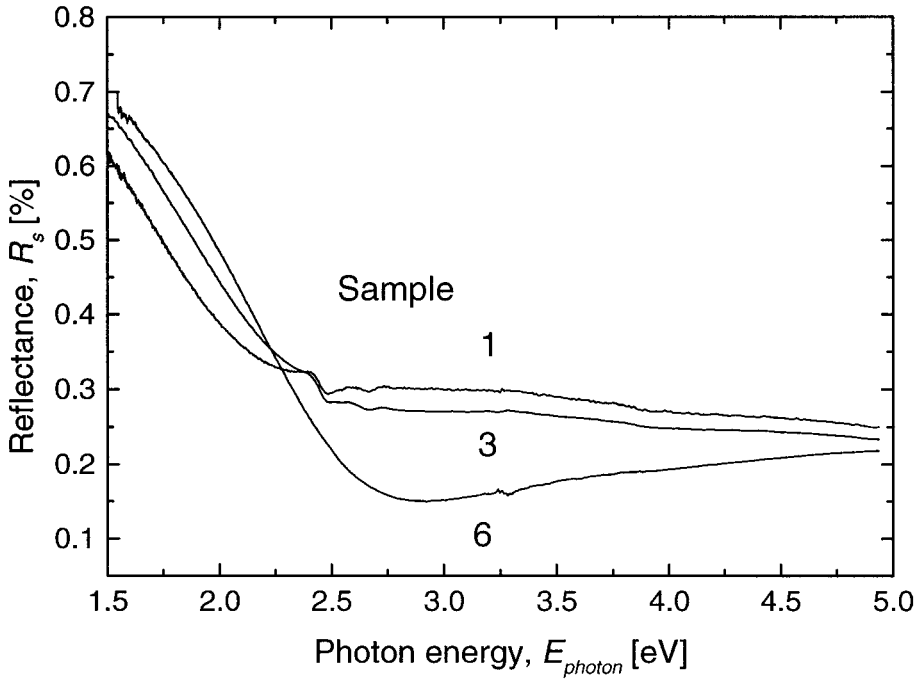

Figure 7.12. *Reflectance of Samples 1, 3 and 6 as a function of [E_{photon}].*

Sample 1 presents a rapid decrease of R_s up to about 2.6 eV, where a minimum in the $R_s(E_{photon})$ dependence occurs. This energy represents the so-called plasma energy, E_{plasma} and is defined as E_{photon} for which $\varepsilon_1 = 0$. It is expressed as:

$$E_{plasma} = \hbar\omega_p = \hbar\sqrt{\frac{n_e e^2}{\varepsilon_0 m^*}}, \tag{7.1}$$

where ω_p is the plasma frequency, e is the charge of an electron and m^* is the effective mass of an electron. The steep slope of the R_s curve and the large value of E_{plasma} are the result of high n_e and, therefore, are characteristic of metallic materials. As [C_{bulk}] rises, the slope of $R_s(E_{photon})$ decreases and E_{plasma} shifts to lower photon energies from 2.53 to

1.78 eV (Fig. 7.13). This is related to both a decrease of n_e and an increase of m^* (see Eq. 7.1) due to a larger curvature of the conduction band in TiC than in TiN, as calculated from the electronic valence band structures [239-242]. For pure TiN, values of m^* were found to be between 1 and 1.6 higher than the mass of the free electron, m_e [185].

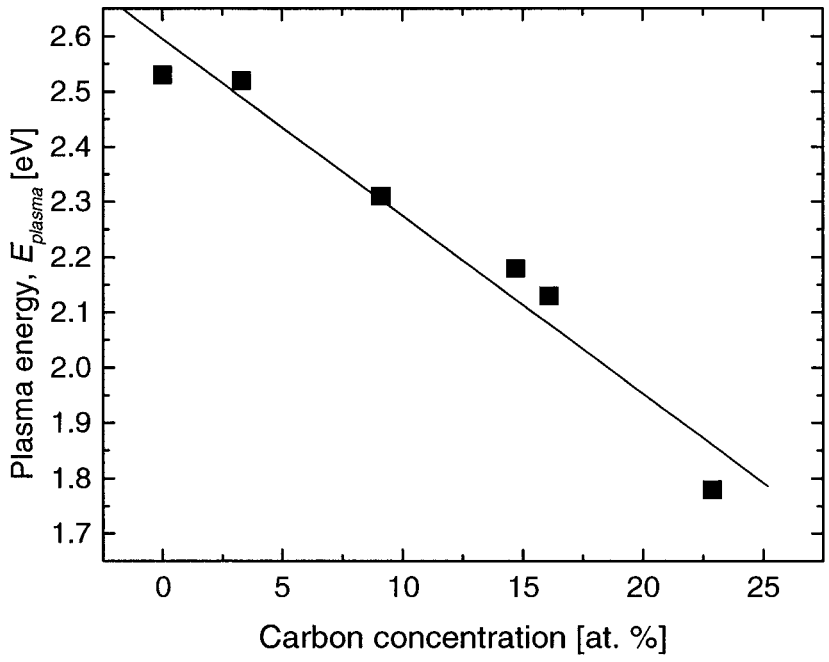

Figure 7.13. *Plasma energy of nc-TiC_xN_y/SiCN films as a function of [C_{bulk}].*

The R_s measurements were used to evaluate the luminosity and the colors [225]. As R_s decreases with the increase of [C_{bulk}], the material becomes opaque and the luminosity decreases as well (from about 70 % for Sample 1 to 60 % for Sample 6, see Fig. 7.14).

The coatings also lose their characteristic metallic luster. This is accompanied by a change in color. Sample 1 possesses a color that is close to that of gold as shown in Fig. 7.15 in the xyY color space. This is due to a similar value of the interband electronic transition threshold of TiN and Au [186]. As [C_{bulk}] rises the color changes from gold to brown red that is close to the color of TiC.

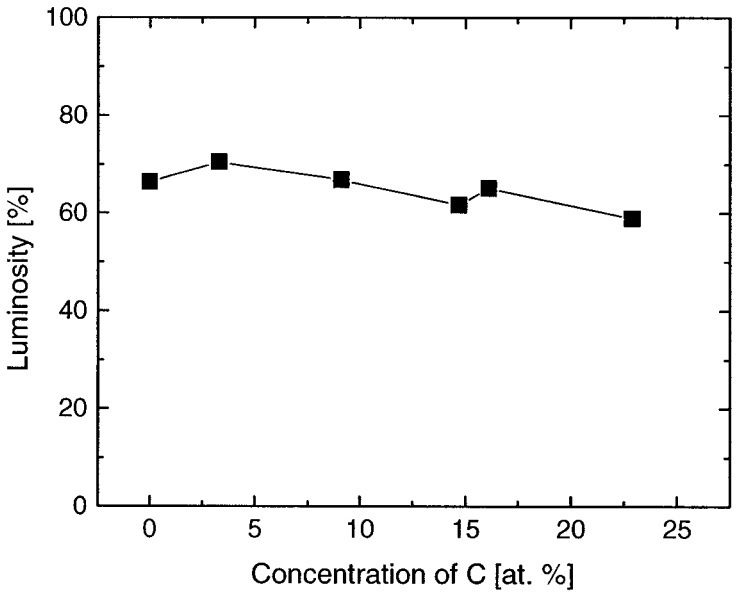

Figure 7.14. *Luminosity of nc-TiC_xN_y/SiCN films as a function of [C_{bulk}].*

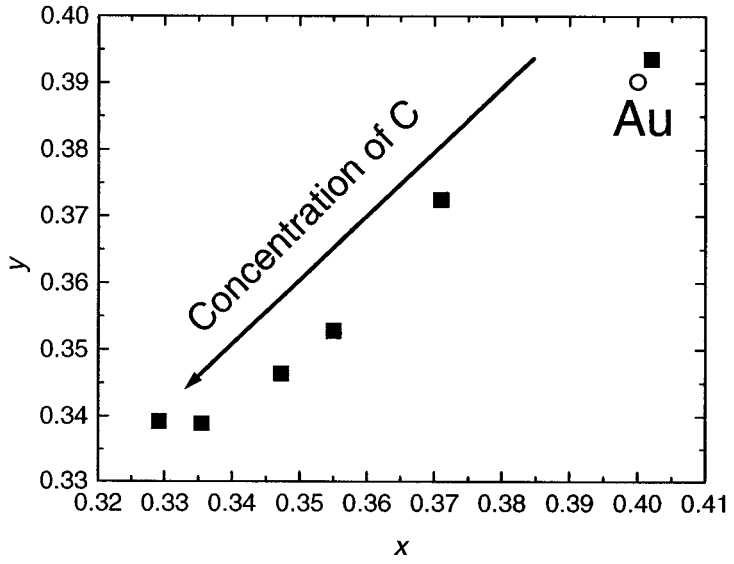

Figure 7.15. *Color changes of nc-TiC_xN_y/SiCN films as a function of [C_{bulk}]. For comparison the value for Au is also shown.*

Changes of color and luminosity reflect a complex transformation of the composition and structure of the material [145, 170]. This may be attributed to the changes of R_s, and to the decrease of the free electron density. This results in a change of E_{plasma}, when material properties change from a metallic (such as nc-TiN/$SiN_{1.3}$) to a more dielectric character (nc-TiC_xN_y/SiCN) due to higher [C_{bulk}].

7.9. Conclusions

In this work the optical properties of nc-TiC_xN_y/SiCN coatings were investigated. The presented results are complementary to those presented in the first part of this Chapter, where the influence of [C_{bulk}] on the microstructural evolution and on the mechanical properties of nc-TiC_xN_y/SiCN was evaluated. The change of optical and electronic properties from metallic-like to dielectric-like supports the proposed microstructural model of nc-TiC_xN_y/SiCN. In this model, for [C_{bulk}] < 15 at. %, C substitutes N in the nc-TiN/$SiN_{1.3}$, enhancing its mechanical properties. For [C_{bulk}] > 15 at. % an alloying effect was observed. The optical properties and colors were quantitatively assessed by combined ellipsometric measurements and spectrophotometry. Through the control of the microstructure we varied the refractive index from 1.2 to 2.0 and the extinction coefficient from 1.7 to 1.2. With the increase of [C_{bulk}] the resistivity increased from 75 to 330 μΩcm. This trend was accompanied by a shift of the plasma energy from 2.53 to 1.78 eV, followed by a decrease of luminosity and a change of color from gold-like to reddish.

Chapter 8. General discussion and conclusions

The qualitative and quantitative evaluation of the structure-property relations and research on new materials and structures are key to progress in the field of hard coatings and to their future practical applications. Specifically, the results of this work contributed to the development of novel superhard nanocomposite coatings. We demonstrated a possibility to fabricate nanocomposite materials by low temperature PECVD. In particular, the structure, consisting of TiN and TiCN nanoparticles in the amorphous matrices of $SiN_{1.3}$ and SiCN, was characterized using a multitechnique approach which was optimized with respect to the mechanical and tribological behavior. In addition, evaluation of the optical properties and colors is also new and original.

The main results of this work can be summarized as follows:

1. A low temperature PECVD process, suitable for the fabrication of nc-TiN/$SiN_{1.3}$ coatings, was developed and optimized. These coatings were systematically compared to the materials fabricated at high temperature.
2. The methodology of the measurement and interpretation of the mechanical properties of hard and superhard coatings was established. Special attention was paid to the measurements of hardness and Young's modulus. The former was evaluated using dynamic and static indentations. To account for the influence of the substrate and the indentation size effect, the hardness of each coating was related to the composite hardness of the coating-substrate system by applying different mathematical models. The influence of the substrate was estimated by geometrical considerations taking into account the coating's thickness, the load applied to the indenter, and the geometry of the indentation. Both techniques yielded similar values, to within approximately 10 %.
3. The influence of C on SiCN films constituting the amorphous matrix of the nc-TiC_xN_y/SiCN was evaluated. Introducing C to $SiN_{1.3}$ caused a substantial enhancement of the mechanical and tribological performance in terms of hardness,

reduced Young's modulus and elastic rebound that reached 33 GPa, 200 GPa and 85 %, respectively. Therefore, the optimized SiCN material was chosen as an amorphous matrix for the new quaternary nc-TiC_xN_y/SiCN system.

4. A novel superhard nc-TiC_xN_y/SiCN material was synthesized. The nc-TiC_xN_y/SiCN films are characterized by a high hardness above 55 GPa, reduced Young's modulus of 306 GPa, and high elastic rebound of more than 80 %. These values contribute to a high resistance to plastic deformation, expressed in terms of the H^3/E_r^2 ratio that reached a value of 1.8 GPa. This value appears higher than the ones reported in the literature, and makes these films very promising candidates for erosion and impact resistant coatings. Relatively low compressive stress between 2.0 and 2.5 GPa, a toughness of about 1.0 MPa $m^{0.5}$ and friction coefficient and wear rate of 0.13 and $12*10^{-6}$ mm^3/Nm were also measured. The improved mechanical properties are due to the effect of substitution of N by C atoms possessing stronger covalent bonds. However, above an optimum concentration of C, the phase segregation was suppressed and an alloying effect caused a decrease of the coatings' performance.

This thesis represents the first systematic work in the area of superhard nanocomposite coatings in our laboratory. Due to their excellent mechanical properties these materials are very attractive for various applications in the aerospace, automobile, microsystems and other areas. Moreover, the PECVD fabrication technique allows one to fabricate coatings on three-dimensional substrates with a complex geometry. This work established the background for other directions of research:

1. Systematic investigation of the tribological properties; this includes improvement of adhesion to engineering substrates, such as stainless steel, HSS, titanium and aluminium alloys, and cemented carbides. The behavior of nanocomposite coatings on cutting tools, drills, turbine blades or other components in the real working environment should be investigated. An appropriate testing methodology must, of course, also be advanced.

2. Our laboratory possesses the expertise and many years of experience in the area of monitoring plasma deposition processes. This includes *in situ* ellipsometry, mass spectrometry, optical emission spectroscopy and others. These techniques should be employed to investigate in particular detail the growth dynamics of the nanocomposite films and the mechanisms of phase segregation, in order to better understand and to further optimize the deposition process.
3. There still remain numerous open questions related to the evaluation of nanocomposite microstructure. Of particular importance is the analysis of the interface between the crystalline nanoparticles and the amorphous matrix, and the dislocation density in the nanocrystalline phase. High resolution TEM can help to answer these questions.
4. The synthesis and characterization of ionic oxides and covalently bonded systems has already a long tradition in our laboratory. Therefore, an extension of this research towards incorporating these materials in nanocomposite superhard and protective coatings would be very logical. This can contribute to further enhancement of tribo-mechanical performance of nanostructured coatings.

References

1. Ohring M., *Materials Science of Thin Films*, Academic Press, 1992.
2. Bhushan B. (Ed.), *Handbook of Micro/Nano Tribology*, CRC Press, New York, 1995.
3. Bunshah R.F. (ed.), *Handbook of Hard Coatings; Deposition Technologies, Properties and Applications*, Noyes Publications, Park Ridge, New Jersey, USA, 2001.
4. Holmberg K., Matthews A., Coatings *Tribology; Properties, Techniques and Applications in Surface Engineering*, Elsevier 1998.
5. Willey R.R., *Practical Design and Production of Optical Thin Films*, Dekkar, 1996.
6. Schweitzer K.K., Johner G., "Performance evaluation of coatings for jet engine turbine blades by servicelike tests", J. Vac. Sci. Technol. **A 3** (1985) 2525.
7. Reinhold E., Botzler P., Deus C., "EB-PVD process management for highly productive zirconia thermal barrier coating of turbine blades", Surf. Coat. Technol. **120-121** (1999) 77-83.
8. Arps J.H., Page R.A., Dearnaley G., "Reduction of wear in critical engine components using ion-beam-assisted deposition and ion implantation", Surf. Coat. Technol. **84** (1996) 579-583.
9. Bonss S., Brenner B., Scheibe H.-J., Ziegele H., "Laser gas alloying-manufacturing process for wear resistant layers on titanium alloys", Materialwissenschaft und Werkstofftechnik **28** (1997) 524-528.
10. Porat R., "CVD coating of ceramic layers on ceramic cutting tool materials", J. Phys IV (Colloque) **1** (1991) 549-556.
11. Karagoez S., Fischmeister H.F., "Metallographic observations on the wear process of TiN-coated cutting tools", Surf. Coat. Technol. **81** (1996) 190-200.
12. Moore D.F., Bostock R.M., Boyle P., Conradie E.H., "Materials issues in the application of silicon nitride films in silicon MEMS", Materials Science of

Microelectromechanical Systems (MEMS) Devices IV. Symposium, **687** (2002) 257-264.

13. Staedler T., Schiffmann K.I., "Micromechanical and microtribological properties of thin CN_x and DLC coatings", Adv. Eng. Mater. **3** (2001) 333-337.
14. Schlatter M., "DLC-based wear protection on magnetic storage media", Diam. Relat. Mater. **11** (2002) 1781-1787.
15. Boguslawski G., Couvrat P., Jozwik K., Niedzielski P., Moll J., Nawrat Z., Walkowiak B., Niedzielska A., Szmidt J., Sokolowska A., Mitura S., 3rd Intenatioanl Conference "Novel Applications of Wide Bandgap Layers" (2001) 174-175.
16. Rats D., Poitras D., Soro J.M., Martinu L., von Stebut J., "Mechanical properties of plasma-deposited silicon-based inhomogeneous optical coatings", Surf. Coat. Technol. **111** (1999) 220-228.
17. Aitchison L., *A History of metals*, Interscience Publishers, 1960.
18. Ohring M., *Engineering Materials Science*, Academic Press, 1995.
19. Raveh A., Rubinshtein A., Weiss M., Mintz M.H., Klemberg Sapieha J.-E., Martinu L., "Ta-C micro-composite material formed by heat treatment of plasma carburized layer", Thin Solid Films, submitted September 2003.
20. Bunshah R.F. (ed.), *Handbook on Deposition Technologies for Films and Coatings*, Noyes Publications, Park Ridge, N. J., USA, 1994.
21. Pierson H.O., *Handbook of Chemical Vapor Deposition*, Noyes Publications, Park Ridge, N. J., USA, 1994.
22. Smurkowski D.J., *Environmental Regulation of Surface Engineering*, in C.M. Cotell, J.A. Sprague, F.A. Smith Jr. (Eds.), Surface Engineering, ASM Handbook, Vol. 5, ASM International, Materials Park, OH, 1994, pp. 911-917.
23. Commision of the European Communities, Proposal for a Council Directive Establishing the Framework for Community Action in the Field of Water Policy, Official Journal of the European Communities C series 184/97, Strasbourg, 1997, pp. 20-90.

24. Jehn H.A, "Multicomponent and multiphase hard coatings for tribological applications", Surf. Coat. Technol. **131** (2000) 433-440
25. Movchan B.A., Demchishin A.V., "Investigation of the structure and properties of thick vacuum- deposited films of nickel, titanium, tungsten, alumina and zirconium dioxide", Fizika Metallov i Metallovedenie **28** (1969) 653-660.
26. Thornton J.A., "Influence of apparatus geometry and deposition conditions on the structure and topography of thick sputtered coatings", J. Vac. Sci. Technol. **11** (1974) 666–670.
27. Messier R., Giri A.P., Roy R.A, "Revised structure zone model for thin film physical structure", J. Vac. Sci. Technol. **A 2** (1984) 500–503.
28. Kelly P.J., Arnell R.D., "Development of a novel structure zone model relating to the closed-field unbalanced magnetron sputtering system", J. Vac. Sci. Technol. **A 16** (1998) 2858-2869.
29. Lieberman M.A., Lichtenberg A.J., *Principles of Plasma Discharges and Materials Processing*, John Wiley and Sons, New York, 1994.
30. Martinu L., Klemberg-Sapieha J.E, Wertheimer M.R., "Dual-mode microwave/radio frequency plasma deposition of dielectric thin films", Appl. Phys. Lett. **54** (1989) 2645-2647.
31. Klemberg-Sapieha J.E., Küttel O.M., Martinu L., Wertheimer M.R., "Dual microwave/radio frequency plasma deposition of functional coatings", Thin Solid Films **193-194** (1990) 965-972.
32. Martinu L., Raveh A., Domingue A., Bertrand L., Klemberg-Sapieha J.E, Gujrathi S.C., Wertheimer M.R., "Hard Carbon Films Deposited under High Ion Flux", Thin Solid Films **208** (1992) 42-47.
33. Martinu L., Klemberg-Sapieha J.E., Küttel O.M., Raveh A., Wertheimer M.R., "Critical ion energy and ion flux in the growth of films by PECVD", J. Vac. Sci. Technol. **A 12** (1994) 1360-1364.

34. Wertheimer M.R., Martinu L., Moisan M., "Microwave and Dual-Frequency Plasma Processing", in "Plasma Treatments and Deposition of Polymers", R. d'Agostino, ed., Kluwer Academic Publishers, Dordrecht, 1997 pp. 101-127.
35. Zabeida O., Martinu L., "Ion Energy Distributions in Pulsed Large Area Microwave Plasma", J. Appl. Phys., **85** (1999) 6366-6372.
36. Hallil A., Zabeida O., Wertheimer M.R., Martinu L., "Mass-resolved ion energy distributions in continuous dual mode microwave/radio frequency plasmas in argon and nitrogen", J. Vac. Sci. Technol. **A 18** (2000) 882-890.
37. Borges C.F.M., Schelz S., St-Onge L., Moisan M., Martinu L., "Silicon Contamination of Diamond Films Deposited on Si Substrates in Fused Silica-based Reactors", J. Appl. Phys., **79** (1996) 3290-3298.
38. Schneider J.M., Voevodin A.A., Rebholz C., Matthews, A., "Microstructural and morphological effects on the tribological properties of electron enhanced magnetron sputtered hard coatings", J. Vac. Sci. Technol. **13** (1995) 2189-2193.
39. Holleck H., "Material selection for hard coatings", J. Vac. Sci. Technol. **A 4** (1986) 2661-2669.
40. Hibbs M.K., Sundgren J.-E., Jacobson B.E., Johansson B.-O., "The microstructure of reactively sputtered Ti-N films", Thin Solid Films **107** (1983) 149-157.
41. Sproul W.D., Rudnik P.J., Graham M.E., "The effect of N_2 partial pressure, deposition rate and substrate bias potential on the hardness and texture of reactively sputtered TiN coatings", Surf. Coat. Technol. **39-40** (1989) 355-363.
42. Muller D., Cho Y.R., Berg S., Fromm E., "Fracture mechanics tests for measuring the adhesion of magnetron sputtered TiN coatings", Surf. Coat. Technol. **60** (1993) 401-404.
43. Thomsen N.B., Horsewell A., Mogensen K.S., Eskildsen S.S., Mathiasen C., Bottiger J., "Residual stress determination in PECVD TiN coatings by X-ray diffraction: a parametric study", Thin Solid Films **333** (1998) 50–59.

44. Mogensen K.S., Thomsen N.B., Eskildsen S.S., Mathiasen C., Bottiger J., "A parametric study of the microstructural, mechanical and tribological properties of PACVD TiN coatings", Surf. Coat. Technol. **99** (1998) 140–146.

45. Roquiny P., Poulet A., Leys Y., Descamps J.-C., Bodart F., VandenBrande P., "Comparative study of thin film physical properties for TiN_x deposited by DC magnetron sputtering under temperatures less than 100 degrees C on monocrystalline silicon and polycrystalline iron substrates", Thin Solid Films **355–356** (1999) 357-362.

46. Schonjahn C., Donohue L.A., Lewis D.B., Munz W.-D., Twesten R.D., Petrov I., "Enhanced adhesion through local epitaxy of transition-metal nitride coatings on ferritic steel promoted by metal ion etching in a combined cathodic arc/unbalanced magnetron deposition system", J. Vac. Sci. Technol. **A 18** (2000) 1718–1723.

47. Ma S., Xu K., He J., "Parametric effects of residual stress in pulsed d.c. plasma enhanced CVD TiN coatings", Surf. Coat. Technol. **142–144** (2001) 1023–1027.

48. Benayoun S., Hantzpergue J.J., Bouteville A., "Micro-scratch test study of TiN films grown on silicon by chemical vapor deposition", Thin Solid Films **389** (2001) 187–193.

49. Chu X., Barnett S.A., Wong M.S., Sproul W.D., "Reactive magnetron sputter deposition of polycrystalline vanadium nitride films", J. Vac. Sci. Technol. **A 14** (1996) 3124-3129.

50. Sproul W.D., "Very high rate reactive sputtering of TiN, ZrN and HfN", Thin Solid Films **107** (1983) 141-147.

51. Sproul W.D., Richman M.H., "Reactive sputtering of TiC with oxygen", Thin Solid Films **28** (1975) L 39-40.

52. Sharma N.K., Williams W.S., Gottschall R.J., "Investigation of the interlayers between cemented carbides and titanium carbide coatings obtained by chemical vapor deposition", Thin Solid Films **45** (1977) 265-273.

53. Perry A.J., Horvath E., "Titanium carbide-coated steel exploits chemical vapour deposition", Metals and Materials (1978) 37-40.

54. Lee C.W., Nam S.W., Chun J.S., "A phenomenological study of the nucleation and growth of chemically vapour-deposited TiC coatings on cemented carbide", Thin Solid Films **86** (1981) 63-71.

55. Sundgren J.-E., Johansson B.-O., Karlsson S.-E., "Mechanisms of reactive sputtering of titanium nitride and titanium carbide. I. Influence of process parameters on film composition", Thin Solid Films **105** (1983) 353-366.

56. Sundgren J.-E., Johansson B.-O., Karlsson S.-E., Hentzell H.T.G., "Mechanisms of reactive sputtering of titanium nitride and titanium carbide. II. Morphology and structure", Thin Solid Films **105** (1983) 467-384.

57. Sundgren J.-E., Johansson B.-O., Hentzell H.T.G., Karlsson S.-E., "Mechanisms of reactive sputtering of titanium nitride and titanium carbide. III. Influence of substrate bias on composition and structure", Thin Solid Films **105** (1983) 385-393.

58. Gabriel H.M., Kloos K.H., "Morphology and structure of ion-plated TiN, TiC and Ti(C,N) coatings", Thin Solid Films **118** (1984) 243-254.

59. Beensh-Marchwicka G., Krol-Stepniewska L., Posadowski, W., "The possibility of thin film structural modification during reactive cosputtering of Ti-Si and Ti-Al in nitrogen", Thin Solid Films **85** (1981) 299.

60. Schonjahn C., Donohue L.A., Lewis D.B., Munz W.-D., Twesten R.D., Petrov I., "Enhanced adhesion through local epitaxy of transition-metal nitride coatings on ferritic steel promoted by metal ion etching in a combined cathodic arc/unbalanced magnetron deposition system", Vac. Sci. Technol. **A 18** (2000) 1718-1723.

61. Taschner Ch., Ljungberg B., Hoffmann V., Vogt C., Leonhardt A., "Deposition of TiN, TiC and $Ti_{1-x}Al_xN$ coatings by pulsed d.c. plasma enhanced chemical vapour deposition methods", Surf. Coat. Technol. **142–144** (2001) 823–828.

62. Donohue L.A., Smith I.J., Muenz W.-D., Petrov I., Greene J.E., "Microstructure and oxidation-resistance of $Ti_{1-x-y-z}Al_xCr_yY_zN$ layers grown by combined steered-arc/unbalanced-magnetron-sputter deposition", Surf. Coat. Technol. **94-95** (1997) 226-231.

63. Feng Huang, Guohua Wei, Barnard J.A., Weaver M.L., "Microstructure and stress development in magnetron sputtered TiAlCr(N) films", Surf. Coat. Technol. **146-147** (2001) 391-397.

64. Goller R., Torri P., Baker M.A., Gilmore R., Gissler W., "The deposition of low-friction TiN-MoS_x hard coatings by a combined arc evaporation and magnetron sputter process", Surf. Coat. Technol. **120–121** (1999) 453-457.

65. Badzian A.R., Badzian T., Roy R., Messier R., Spear K.E., "Crystallization of diamond crystals and films by microwave assisted CVD (Part II)", Materials Research Bulletin, **23** (1988) 531-548.

66. Messier R., Badzian A.R., Badzian T., Spear K.E., Bachmann P., Roy R., "From diamond-like carbon to diamond coatings", Thin Solid Films **153** (1987) 1-9.

67. Sjostrom H., Hultman L., Sundgren J.-E., Hainsworth S.V., Page T.F., Theunissen G.S.A.M., "Structural and mechanical properties of carbon nitride CN_x", J. Vac. Sci. Technol. **A 14** (1996) 56-62.

68. Hajek V. Rusnak K., Vicek J., Martinu L., Gujrathi S.C., "Influence of substrate bias voltage on the properties of CN_x films prepared by reactive magnetron sputtering", J. Vac. Sci. Technol. **A 17** (1999) 899-908.

69. Zhou Z.F., Bello I., Lei M.K., Li K.Y., Lee C.S., Lee S.T., "Synthesis and characterization of boron carbon nitride films by radio frequency magnetron sputtering", Surf. Coat. Technol. **128-129** (2000) 334-340.

70. He Zhigang, Carter G., Colligon J.S., "Ion-assisted deposition of C-N and Si-C-N films", Thin Solid Films **283** (1996) 90-96.

71. Koehler J.S., "Attempt to design a strong solid", Phys. Rev. **B 2** (1970) 547-551.

72. Clemens B.M., Kung H., Barnett S.A., "Structure and strength of multilayers", MRS Bulletin **24** (1999) 20-26.

73. Li Shizhi, Shi Yulong, Peng Hongrui, "Ti-Si-N films prepared by plasma-enhanced chemical vapor deposition", Plasma Chem. Plasma Process. **12** (1992) 287-297.

74. Veprek S., Reiprich S., Li Shizhi, "Superhard nanocrystalline composite materials: the TiN/Si_3N_4 system", Appl. Phys. Lett. **66** (1995) 2640-2642.

75. C. Koch (ed.), *Nanostructured Materials, Processing, Properties and Potential Applications*, Noyes Publications 2002.

76. Voevodin A.A., Fitz T.A., Hu J.J., Zabinski J.S., "Nanocomposite tribological coatings with "chameleon" surface adaptation", J. Vac. Sci. Technol. **A 20** (2002) 1434-1444.

77. Reinke P., Klemberg-Sapieha J.E., Martinu L., "Effect of amorphous carbon layers on the growth of diamond in dual-frequency plasma", J. Appl. Phys. **76** (1994) 5754-5759.

78. Raveh A., Klemberg-Sapieha J.E., Martinu L., Wertheimer M.R., "Deposition and properties of diamondlike carbon films produced in microwave and radio-frequency plasma", J. Vac. Sci. Technol. **A 10** (1992) 1723-1727.

79. Dahl S., Rats D., von Stebut J., Martinu L., Klemberg-Sapieha J.E., "Micromechanical characterisation of plasma treated polymer surfaces", Thin Solid Films **355-356** (1999) 290-294.

80. Solecki R., Conant R.J., *Advanced Mechanics of Materials*, Oxford University Press, 2003.

81. Boresi A.P., Schmidt R.J., Sidebottom O.M., *Advanced Mechanics of Materials*, John Wiley and Sons, 1993.

82. Soboyejo W., *Mechanical Properties of Engineered Materials*, Marcel Dekker, 2003.

83. Kelly A., *Strong Solids*, Clarendon Press, Oxford, 1966.

84. Dorlot J.-M., Bailon J.-P., Masounave J., *Des Materiaux*, Editions de L'Ecole Polytechnique de Montreal, Montreal, 1986.

85. Orowan E., "Fracture and strength of solids", Rep. Prog. Phys. **12** (1949) 185-232.

86. Zwicky F. "Die Reissfestigkeit von Steinsalz", Phys. Z. **24** (1923) 131-137.

87. Born M., Furth R., Proc. Camb. Phil. Soc. Math. Phys. Sci. **36** (1940) 454.

88. Tyson W.R., "Theoretical strength of perfect crystals", Phil. Mag. **14** (1966) 925-936.

89. Frenkel J., "Zur theorie de elastizitatsgrenze und der festigkeit Kristallinischer Korper", Z. Phys. **37** (1926) 572.
90. Mackenzie J.K., Ph. D. Thesis, Bristol, 1949.
91. Tyson, W.R., "Atomistic models for elastic constants of B.C.C. crystals", Phil. Mag., **21** (1970) 1093-1097.
92. Cohen, M.L., "Calculation of bulk moduli of diamond and zinc-blende solids", Phys. Rev. **B 32** (1985) 7988-7991.
93. Liu A.Y., Cohen M.L., "Prediction of new low compressibility solids", Science **245** (1989) 841-842.
94. Liu A.Y., Cohen M.L., "Theoretical study of a hypothetical metallic phase of carbon", Phys. Rev. **B 45** (1992) 4579-4581.
95. Riedel R. (Ed.), *Handbook of Ceramic Materials*, Wiley – VCH, Weinheim, Germany, 2000.
96. Mendez J.M., Muhl S., Farias M., Soto G., Cota-Araiza L., Preparation of cubic boron nitride films by plasma-enhanced chemical vapour deposition of BF_3, N_2 and H_2 gas mixtures, Surf. Coat. Technol. **49** (1991) 422-426.
97. Hall E.O., "The deformation and ageing of mild steel: III Discussion of results", Proc. Roy. Soc. London **B 64** (1951) 747-753.
98. Petch N.J, "The cleavage of polycrystals", J. Iron Steel Inst. **174** (1953) 25-28.
99. Cottrell A.H., *Dislocations and Plastic Flow in Crystals*, Oxford Clarendon Press, 1953
100. Helmersson U., Todorova S., Barnett S.A., Sundgren J.-E., Markert L.C., Greene J.E, "Growth of single-crystal TiN/VN strained-layer superlattices with extremely high mechanical hardness", J. Appl. Phys. **62** (1987) 481-484.
101. Holleck H., Lahres M., Woll P., "Multilayer coatings-influence of fabrication parameters on constitution and properties", Surf. Coat. Technol. **41** (1990) 179-190.
102. Barnett S.A., *Physics of Thin Films*, Academic Press, London, 1993.

103. Sproul W.D., "Multilayer, multicomponent, and multiphase physical vapor deposition coatings for enhanced performance", J. Vac. Sci. Technol. **12** (1994) 1595-1601.

104. Bull S.J., Jones A.M., "Multilayer coatings for improved performance", Surf. Coat. Technol. **78** (1996) 173-184.

105. Kung H., Lu Y.-C., Griffin A.J. Jr., Nastasi M., Mitchell T.E., Embury J.D., "Observation of body centered cubic Cu in Cu/Nb nanolayered composites", Appl. Phys. Lett. **71** (1997) 2103-2105.

106. Kim D.-J., Cho Y.-R., Lee M.-J., Hong J.-M., Kim Y.-K., Lee K.-H., "Properties of TiN-TiC multilayer coatings using plasma-assisted chemical vapor deposition" Surf. Coat. Technol. **116-119** (1999) 906-910.

107. Duck A., Gamer N., Gesatzke W., Griepentrog M., Osterle W., Sahre M., Urban I., "Ti/TiN multilayer coatings: deposition technique, characterization and mechanical properties", Surf. Coat. Technol. **142-144** (2001) 579-584.

108. Cameron D.C., Aimo R., Wang Z.H., Pischow K.A., "Ti/TiN multilayer coatings: deposition technique, characterization and mechanical properties", Surf. Coat. Technol. **142-144** (2001) 567-572.

109. Ming-Show Wong, Gwo-Yih Hsiao, Sheng-Yu Yang, "Preparation and characterization of AlN/ZrN and AlN/TiN nanolaminate coatings", Surf. Coat. Technol. **133-134** (2000) 160-165.

110. Nordin M., Larsson M., Hogmark S., "Mechanical and tribological properties of multilayered PVD TiN/CrN, TiN/MoN, TiN/NbN and TiN/TaN coatings on cemented carbide", Surf. Coat. Technol. **106** (1998) 234-241.

111. Veprek S., "The search for novel, superhard materials", J. Vac. Sci. Technol. **A 17** (1999) 2401-2420.

112. Veprek S., Argon A.S., "Mechanical properties of superhard nanocomposites", Surf. Coat. Technol. **146-147** (2001) 175-182.

113. Veprek S., Argon A.S., "Towards the understanding of mechanical properties of super- and ultrahard nanocomposites", J. Vac. Sci. Technol. **B 20** (2002) 650-664.

114. Musil J., "Hard and superhard nanocomposite coatings", Surf. Coat. Technol. **125** (2000) 322-330.

115. Veprek S., Mukherjee S., Karvankova P., Mannling H.D., He J.L., Moto K., Prochazka J., Argon A.S., "Hertzian analysis of the self-consistency and reliability of the indentation hardness measurements on superhard nanocomposite coatings", Thin Solid Films **436** (2003) 220-231.

116. Musil J., Zeman H., Kunc F., Vlcek J., "Measurement of hardness of superhard films by microindentation", Materials Science & Engineering **A 340** (2003) 281-285.

117. Veprek S., Jilek M., "Super-and ultrahard nanocomposite coatings: generic concept for their preparation, properties and industrial applications", Vacuum **67** (2002) 443-449.

118. Niederhofer A., Nesladek P., Mannling H.-D., Moto K., Veprek S., Jilek M., "Structural properties, internal stress and thermal stability of nc-TiN/a-Si_3N_4, nc-TiN/$TiSi_x$ and nc-$(Ti_{1-y}Al_ySi_x)N$ superhard nanocomposite coatings reaching the hardness of diamond", Surf. Coat. Technol. **120-121** (1999) 173-178.

119. Veprek S., Niederhofer A., Moto K., Bolom T., Mannling H.-D., Nesladek P., Dollinger G., Bergmaier A., "Composition, nanostructure and origin of the ultrahardness in nc-TiN/a-Si_3N_4/a- and nc-$TiSi_2$ nanocomposites with H_V=80 to >or=105 GPa", Surf. Coat. Technol. **133–134** (2000) 152–159.

120. Niederhofer A., Bolom T., Nesladek P., Moto K., Eggs C., Patil D.S., Veprek S., "The role of percolation threshold for the control of the hardness and thermal stability of super- and ultrahard nanocomposites", Surf Coat. Technol. **146–147** (2001) 183–188.

121. Musil J., Zeman P., Hruby H., Mayrhofer P.H., "ZrN/Cu nanocomposite film-a novel superhard material", Surf. Coat. Technol. **120–121** (1999) 179–183.

122. Musil J., Vlcek J., "Magnetron sputtering of hard nanocomposite coatings and their properties", Surf. Coat. Technol. **142–144** (2001) 557–566.

123. Zehnder T., Patscheider J., "Nanocomposite TiC/a-C:H hard coatings deposited by reactive PVD", Surf. Coat. Technol. **133–134** (2000) 138–134.

124. Christiansen S., Albrecht M., Strunk H.P., Veprek S., "Microstructure of novel superhard nanocrystalline-amorphous composites as analyzed by high resolution transmission electron microscopy", J. Vac. Sci. Technol. **B 16** (1998) 19-22.

125. Madou M., *Fundamentals of Microfabrication*, Boca-Raton, London, New York, Washington, 1997.

126. Tabor D., *The Hardness of Metals*, Clarendon, Oxford, 1951.

127. Fisher-Cripps A.C., *Nanoindentation*, Springer, New York, 2002.

128. Bull S.J., Page T.F., Yoffe E.H., "An explanation of the identification size effect in ceramics", Phil. Mag. Lett. **59** (1989) 281-288.

129. Burnett P.J., Rickerby D.S., "The mechanical properties of wear-resistant coatings. I. Modelling of hardness behaviour", Thin Solid Films **148** (1987) 41-50.

130. Oliver W.C., Pharr G.M., "An improved technique for determining hardness and elastic modulus using load and displacement sensing indentation experiments", J. Mater. Res. **7** (1992) 1564-1583.

131. Schneider D., Siemroth P., Schulke T., Berthold J., Schultrich B., Schneider H.-H., Ohr R., Petereit B., Hillgers H., "Quality control of ultra-thin and super-hard coatings by laser-acoustics", Surf. Coat. Technol. **153** (2002) 252–260.

132. Tsui T.Y., Pharr G.M., Oliver W.C., Bhatia C.S., White R.L., Anders S., Anders A., Brown I.G., "Nanoindentation and nanoscratching of hard carbon coatings for magnetic disks", Mater. Res. Soc. Symp. Proc. **383** (1995) 447-452.

133. Leyland A., Matthews A., "On the significance of the H/E ratio in wear control: a nanocomposite coating approach to optimised tribological behaviour", Wear **246** (2000) 1-11.

134. International Standard, *Metallic materials – Instrumented indentation test for hardness and materials parameters, Part 1: Test methods,* ISO 14577-1 (2002).

135. Muller K.-H., "Stress and microstructure of sputter-deposited thin films: molecular dynamics investigations", J. Appl. Phys. **62** (1987) 1796-1799.

136. Petrov I., Hultman L., Sundgren J.-E., Greene J.E., "Polycrystalline TiN films deposited by reactive bias magnetron sputtering: effects of ion bombardment on

resputtering rates, film composition, and microstructure", J.Vac.Sci.Technol **A 10** (1992) 265-272.

137. Bhushan B., *Principles and Applications of Tribology*, John Wiley and Sons, 1999.
138. Wooten F., *Optical Properties of Solids,* Academic Press, 1972.
139. Agoston G.A., *Color Theory and Its application in Art and Design*, Springer Series in Optical Science, Springer 1979.
140. MacAdam D.L., "Color essays", J. Opt. Soc. Am. **65** (1975) 483–492.
141. MacAdam D.L, *Color Measurements, Theme and Variations*, Springer-Verlag, 1985.
142. Gujrathi S.C., in: Sacher E., Pireaux J.J., Kowalczyk S.P. (Eds.), *Metallized Polymers*, Vol. 440, ACS Symposium Series, ACS Washington DC, 1990, p. 88
143. Dawson P.T., Tzatzov K.K., "Quantitative Auger electron analysis of titanium nitrides", Surf. Sci. **149** (1985) 105-118.
144. Hofmann S., "Characterization of nitride coatings by Auger electron spectroscopy and X-ray photoelectron spectroscopy", J. Vac. Sci. Technol. **A 4** (1986) 2789-2796.
145. Beck U., Reiners G., Urban I., Witt K., "Evaluation of optical properties of decorative coatings by spectroscopic ellipsometry", Thin Solid Films **220** (1992) 240.
146. Roquiny P., Bodart F., Terwagne G., "Colour control of titanium nitride coatings produced by reactive magnetron sputtering at temperature less than 100 degrees C", Surf. Coat Technol. **116-119** (1999) 283.
147. Musil J., Vlcek, J., "Magnetron sputtering of films with controlled texture and grain size", Mater. Chem. Phys. **54** (1998) 116-122.
148. Matthews A., Leyland A., Holmberg K., Ronkainen H., "Design aspects for advanced tribological surface coatings", Surf. Coat. Technol. **100-101** (1998) 1-6.
149. Veprek S., Reiprich S., "A concept for the design of novel superhard coatings", Thin Solid Films **268** (1995) 64-71.
150. Weertman J.R., Farkas D., Hemker K., Kung H., Mayo M., Mitra R., van Swygenhoven H., "Structure and mechanical behavior of bulk nanocrystalline materials", MRS Bulletin **24** (1999) 44-50.

151. Diserens M., Patscheider J., Levy F., "Mechanical properties and oxidation resistance of nanocomposite TiN-SiN_x physical-vapor-deposited thin films", Surf. Coat. Technol. **120-121** (1999) 158-165.

152. Musil J., Hruby H., Zeman P., Cerstvy R., Maythofer P.H., Mitterer C., Proc. of the PSE Conf. Garmish-Partenkirchen, Germany (2000) 601.

153. Musil J., Kunc F., Zeman H., Polakova H., "Relationships between hardness, Young's modulus and elastic recovery in hard nanocomposite coatings", Surf. Coat. Technol. **154** (2002) 304-313.

154. Oliver W.C., Hutchings R., Pethica J.B. in *Microindentation Techniques in Materials Science and Engineering,* P.J. Blau and B.R. Lawn (eds.), ASTM STP 889, American Society for Testing and Materials, Philadelphia (1986) 90.

155. Jonsson B., Hogmark S., "Hardness measurements of thin films", Thin Solid Films **114** (1984) 257-269.

156. Burnett P.J., Rickerby D.S., "The mechanical properties of wear-resistant coatings. II. Experimental studies and interpretation of hardness", Thin Solid Films **148** (1987) 51-65.

157. Chicot D., Lesage J., "Absolute hardness of films and coatings", Thin Solid Films **254** (1995) 123-130.

158. Korsunsky A.M., McGurk M.R., Bull S.J., Page T.F., "On the hardness of coated systems" Surf. Coat. Technol. **99** (1998) 171-182.

159. Ichimura H., Rodriguez F.M., Rodrigo A., "The composite and film hardness of TiN coatings prepared by cathodic arc evaporation", Surf. Coat. Technol. **127** (2000) 138-143.

160. Tuck J.R., Korsunsky A.M., Bull S.J., Davidson R.I., "On the application of the work-of-indentation approach to depth-sensing indentation experiments in coated systems", Surf. Coat. Technol. **137** (2001) 217-224.

161. Guiner A., *Théorie et technique de radiocrystallographie,* Dunod, Paris, 1956.

162. Johnson K.L., *Contact Mechanics,* Cambridge University Press, Cambridge, 1985.

163. Johnson K.L., "The correlation of indentation experiments", J. Mech. Phys. Solids **18** (1970) 115-126.

164. Chiang S.S., Marshall D.B., Evans A.G., "The response of solids to elastic/plastic indentation. I. Stresses and residual stresses", J. Appl. Phys. **53** (1982) 298-311.

165. Chiang S.S., Marshall D.B., Evans A.G., "The response of solids to elastic/plastic indentation. II. Fracture initiation", J. Appl. Phys. **53** (1982) 312-317.

166. Berriche R., "Evaluation of advanced aerospace materials by depth sensing indentation and scratch methods", Canadian Aeronautics and Space Journal **40** (1994) 163-170.

167. Bull S.J., "Interface engineering and graded films: Structure and characterization", J. Vac. Sci. Technol. **A 19** (2001) 1404-1414.

168. Greene J.F., Sundgren J.-E., Hultman L., Petrov I., Bergstrom D.B., "Development of preferred orientation in polycrystalline TiN layers grown by ultrahigh vacuum reactive magnetron sputtering", Appl. Phys. Lett. **67** (1995) 2928-2930.

169. Schmalzried H., *Chemical Kinetics of Solids*, VCH Verlag, Weinheim 1995.

170. Perry A.J., "The color of TiN and HfN: aging effects", J. Vac. Sci. Technol. **A 4** (1986) 2670-2673.

171. Perry A.J., Georgson M., Ribbing C.G., "The reflectance and color of titanium nitride", J. Vac. Sci. Technol. **A 4** (1986) 2674-2677.

172. Jae-Woong Nah, Byoung-June Kim, Dong-Kak Lee, Jung-Joong Lee, "Color, structure, and properties of TiN coatings prepared by plasma enhanced chemical vapor deposition", J. Vac. Sci. Technol. **A 17** (1999) 463-469.

173. Valkonen E., Ribbing C.-G., Sundgren J.-E., "Optical constants of thin TiN films: thickness and preparation effects", Appl. Opt. **25** (1986) 3624-3630.

174. Claesson Y., Georgson M., Roos A., Ribbing C.-G., "Optical characterisation of titanium-nitride-based solar control coatings", Sol. Energy Mater. **20** (1990) 455-465.

175. Antonova K., Grigorov G., Martev I., Yakovlev V., Zhizhin G., "Optical properties of selective reflection TiN_x films", Thin Solid Films **219** (1992) 157-161.

176. Levy F., Hones P., Schmid P.E., Sanjines R., Diserens M., Wiemer C., "Electronic states and mechanical properties in transition metal nitrides", Surf. Coat. Technol. **120-121** (1999) 284-290.

177. Humlicek J., Nebojsa A., Hora J., Strasky M., Spousta J., Sikola T., "Ellipsometry and transport studies of thin-film metal nitrides", Thin Solid Films **332** (1998) 25-29.

178. Veprek S., Haussmann M., Reiprich S., Li Shizhi, Dian J., "Novel thermodynamically stable and oxidation resistant superhard coating materials", Surf. Coat. Technol. **86-87** (1996) 394-401.

179. Jedrzejowski P., Klemberg-Sapieha J.E., Martinu L., "Relationship between the mechanical properties and the microstructure of nanocomposite TiN/$SiN_{1.3}$ coatings prepared by low temperature plasma enhanced chemical vapor deposition", Thin Solid Films **426** (2003) 150-159.

180. Hummel R.E., *Electronic Properties of Materials; an Introduction for Engineers*, Springer-Verlag, 1985.

181. *Guide to Using WVASE 32*, J.A. Woollam Co. Inc.

182. Maxwell Garnett J.C. "Colours in metal glasses, in metallic films, and in metallic solutions. II", Phil. Trans. Royal Soc. London, **205** (1906) 237-288.

183. Evans R.M., *The Perception of Color*, John Wiley and Sons, 1974.

184. Smits F.M., "Measurements of sheet resistivities with the four-point probe", The Bell System Technical Journal **37** (1958) 711-718.

185. Karlsson B.K., Sundgren J.-E., Johansson B.-O., "Optical constants and spectral selectivity of titanium carbonitrides", Thin Solid Films **87** (1982) 181-187.

186. Logothetidis S., Alexandrou I., Papadopoulos A., « In situ spectroscopic ellipsometry to monitor the process of TiN_x thin films deposited by reactive sputtering", J. Appl. Phys. **77** (1995) 1043-1047.

187. Jagannadham K., Chowdhury R., Biunno N., Narayan J., "Raman spectroscopy of TiN films deposited on silicon (001) substrate by laser physical vapor deposition", Mat. Res. Soc. Symp. Proc. **317** (1994) 193-198.

188. Spengler W., Kaiser R., Christensen A.N., Muller-Vogt G., "Raman scattering, superconductivity and phonon density of states of stoichiometric and nonstoichiometric TiN. (Comparison with TiC)", Phys. Rev. **B 17** (1978) 1095-1101.

189. Veprek S., Haussmann M., Reiprich S., "Superhard nanocrystalline W_2N/amorphous Si_3N_4 composite materials", J. Vac. Sci. Technol. **A 14** (1996) 46-51.

190. Badzian A., Badzian T., Roy R., Drawl W., "Silicon carbonitride, a new hard material and its relation to the confusion about `harder than diamond' C_3N_4", Thin Solid Films **354** (1999) 148.

191. Bendeddouche A., Berjoan R., Beche E., Hillel R., "Hardness and stiffness of amorphous SiC_xN_y chemical vapor deposited coatings", Surf. Coat. Technol. **111** (1999) 184-193.

192. He Zhigang, Carter G., Colligon J.S, "Ion-assisted deposition of C-N and Si-C-N films", Thin Solid Films **283** (1996) 90-96.

193. Tharigen T., Lippold G., Riede V., Lorenz M., Koivusaari K.J., Lorenz D., Mosch, S., Grau P., Hesse R., Streubel P., Szargan R., "Hard amorphous CSi_xN_y thin films deposited by rf nitrogen plasma assisted pulsed laser ablation of mixed graphite/Si_3N_4-targets", Thin Solid Films **348** (1999) 103-113.

194. Liew L.-A., Yiping Liu, Ruiling Luo, Cross T., Linan An, Bright V.M., Dunn M.L., Daily J.W., Raj R., "Fabrication of SiCN MEMS by photopolymerization of pre-ceramic polymer", Sens. Actuators **A 95** (2002) 120-134.

195. Berlind T., Hellgren N., Johansson M.P., Hultman L., "Microstructure, mechanical properties, and wetting behavior of Si-C-N thin films grown by reactive magnetron sputtering", Surf. Coat. Technol. **141** (2001) 145-155.

196. Bertran E., Martinez E., Viera G., Farjas J., Roura P., "Mechanical properties of nanometric structures of Si/SiC, C/SiC and C/SiN produced by PECVD", Diam. Relat. Mater. **10** (2001) 1115-1120.

197. Riedel R., Kleebe H.-J., Schonfelder H., Aldinger F., "A covalent micro/nanocomposite resistant to high-temperature oxidation", Nature **374** (1995) 526-528.

198. Zhang D.H., Gao Y., Wei J., Mo Z.Q., "Influence of silane partial pressure on the properties of amorphous SiCN films prepared by ECR-CVD", Thin Solid Films **377-378** (2000) 607-610.

199. Chen K.H., Wu J.-J., Wen C.Y., Chen L.C., Fan C.W., Kuo P.F., Chen Y.F., Huang Y.S., "Wide band gap silicon carbon nitride films deposited by electron cyclotron resonance plasma chemical vapor deposition", Thin Solid Films **355-356** (1999) 205-209.

200. Gomez F.J., Prieto P., Elizalde E., Piquerasa J., "SiCN alloys deposited by electron cyclotron resonance plasma chemical vapor deposition", Appl. Phys. Lett. **69** (1996) 773-775.

201. Soto G., Samano E.C., Machorro R., Cota L.," Growth of SiC and SiC_xN_y films by pulsed laser ablation of SiC in Ar and N_2 environments", J. Vac. Sci. Technol. **A 16** (1998) 1311-1315.

202. Chen L.C., Lin H.Y., Wong C.S., Chen K.H., Lin S.T., Yu Y.C., Wang C.W., Lin E.K., Ling K.C., "Ellipsometric study of carbon nitride thin films with and without silicon addition", Diam. Relat. Mater. **8** (1999) 618-622.

203. Seifert H.J., Jianqiang Peng, Lukas H.L., Aldinger F., "Phase equilibria and thermal analysis of Si-C-N ceramics", J. Alloys Compd. **320** (2001) 251-261.

204. Vernhes R., Zabeida O., Klemberg-Sapieha J.E., Martinu L., "Single-material inhomogeneous optical filters based on microstructural gradients in plasma-deposited silicon nitride", Appl. Opt. 2003, submitted.

205. Sundaram K.B., Alizadeh J., "Deposition and optical studies of silicon carbide nitride thin films", Thin Solid Films **370** (2000) 151-154.

206. El Khakani M.A., Chaker M., Jean A., Boily S., Kieffer J.C., O'Hern M.E., Ravet M.F., Rousseaux F., "Hardness and Young's modulus", J. Mater. Res. **9** (1994) 96-103.

207. Gao Y., Wei J., Zhang D.H., Mo Z.Q., Hing P., Shi X., "Effects of nitrogen fraction on the structure of amorphous silicon-carbon-nitrogen alloys", Thin Solid Films **377-378** (2000) 562-566.

208. Gong Zheng, Wang E.G., Xu G.C., Chen Yan, "Influence of deposition condition and hydrogen on amorphous-to-polycrystalline SiCN films", Thin Solid Films **348** (1999) 114-121.

209. Sachdev H., Scheid P., "Formation of silicon carbide and silicon carbonitride by RF-plasma CVD", Diam. Relat. Mater. **10** (2001) 1160-1164.

210. Viera G., Andujar J.L., Sharma S.N., Bertran E., "Si-C-N nanometric powder produced in square-wave modulated RF glow discharges", Diam. Relat. Mater. **7** (1998) 407-411.

211. Chen L.C., Yang C.Y., Bhusari D.M., Chen K.H., Lin M.C., Lin J.C., Chuang T.J., "Formation of crystalline silicon carbon nitride films by microwave plasma-enhanced chemical vapor deposition", Diam. Relat. Mater. **5** (1996) 514-518.

212. Jin-Yu Wu, Cheng-Tzu Kuo, Po-Ju Yang, "Growth competition between crystalline silicon carbon nitrides and silicon nitrides deposited on Si wafer by MPCVD", Mater. Chem. Phys. **72** (2001) 245-250.

213. Wu J.-J., Wu C.-T., Liao Y.-C., Lu T.-R., Chen L.C., Chen K.H., Hwa L.-G., Kuo C.-T., Ling K.-J., "Deposition of silicon carbon nitride films by ion beam sputtering", Thin Solid Films **355-356** (1999) 417-422.

214. Vlcek J., Kormunda M., Cizek J., Perina V., Zemek J., "Influence of nitrogen-argon gas mixtures on reactive magnetron sputtering of hard Si-C-N films", Surf. Coat. Technol. **160** (2002) 74-81.

215. Lutz H., Bruns M., Link F., Baumann H., "Surface- and microanalytical characterization of silicon-carbonitride thin films prepared by means of radio-frequency magnetron co-sputtering", Thin Solid Films **332** (1998) 230-234.

216. Moulder J.F, Stickle W.F., Sobol P.E., Boniber K.D., *Handbook of X-Ray Photoelectron Spectroscopy* (ed. J. Chastain), Perkin-Elmer, Eden Prairie, MN, 1992.

217. Wen-Shiang Liao, Chi-Huei Lin, Si-Chen Lee, "Oxidation of silicon nitride prepared by plasma-enhanced chemical vapor deposition at low temperature", Appl. Phys. Lett. **65** (1994) 2229-2231.

218. Ulrich S., Ehrhardt H., Theel T., Schwan J., Westermeyr S., Scheib M., Becker P., Oechsner H., Dollinger G., Bergmaier A., "Phase separation in magnetron sputtered superhard BCN thin films", Diam. Rel. Mater. **7** (1998) 839-844.

219. Xing-cheng Xiao, Ya-Wen Li, Li-Xin Song, Xiao-Feng Peng, Xing-Fang Hu, "Structural analysis and microstructural observation of SiC_xN_y films prepared by reactive sputtering of SiC in N_2 and Ar", Appl. Surf. Sci. **156** (2000) 155-160.

220. Schuhmacher J., Berger F., Weinmann M., Bill J., Aldinger F., Muller K., "Solid-state NMR and FTIR studies of the preparation of Si-B-C-N ceramics from boron-modified polysilazanes", Appl. Organometal. Chem. **15** (2001) 809-819.

221. Xiaofeng Peng, Lixin Song, Jun Le., Xingfang Hu, "Spectra characterization of silicon carbonitride thin films by reactive radio frequency sputtering", J. Vac Sci. Technol. **B 20** (2002) 159-163.

222. Wrobel A.M., Pietrzykowska-Walkiewicz A., Klemberg-Sapieha J.E., Hatanaka Y., Aoki T., Nakanishi Y., "Remote hydrogen plasma chemical vapor deposition of silicon-carbon thin-film materials from a hexamethyldisilane source: characterization of the process and the deposits", J. Appl. Polym. Sci. **86** (2002) 1448-1458.

223. Lattemann M., Ulrich S., Holleck H., Stuber A., Leiste H., "Characterisation of silicon carbide and silicon nitride thin films and Si_3N_4/SiC multilayers", Diam. Rel. Mater. **11** (2002) 1248-1253.

224. Kubart T., Mala Z., Novak R., Novakova D., "Effect of coated edge geometry on internal stress distribution in multilayered coatings", Surf. Coat. Technol. **142-144** (2001) 610-614.

225. Jedrzejowski P., Baloukas B., Klemberg-Sapieha J.E, Martinu L., "Optical characteristics and color of TiN/$SiN_{1.3}$ nanocomposite coatings", J. Vac. Sci. Technol. (2003), submitted.

226. Jedrzejowski P., Cizek J., Amassian A., Klemberg-Sapieha J.E., Vlcek J., Martinu L., "Mechanical and optical properties of hard SiCN coatings prepared by PECVD", Thin Solid Films (2003), in press.

227. International Standard ISO 14577-1 *Metallic Materials – Instrumented Indentation Test for Hardness and Materials Parameters*, 2002.

228. Consiglio R., Durand N., Badawi K.F., Macquart P., Lerbet F., Assoul M., Von Stebut J., "Mechanical strength assessment of very thin films for optical and electronic applications", Surf. Coat. Technol. **97** (1997) 192.

229. Aboelfotoh M.O., Stolt I., Petersson C.S., "Electrical characteristics of Ti-Si (100) interfaces", 7th Int. Conf. on Thin Films, New Delhi, 1987.

230. Girolami G.S., Jemes J.A., Pollina D.M, "Organometallic route to the chemical vapor deposition of titanium carbide films at exceptionally low temperatures", J. Am. Chem. Soc. **109** (1987) 1579.

231. Vasile M.J., Emerson A.B., Baiocchi F.A., "The characterization of titanium nitride by X-ray photoelectron spectroscopy and Rutherford backscattering", J. Vac. Sci. Technol. **A 8** (1990) 99-105.

232. Saha N.C., Tompkins H.G., "Titanium nitride oxidation chemistry: an X-ray photoelectron spectroscopy study", J. Appl. Phys. **72** (1992) 3072-3079.

233. Kaufherr N., Lichtman, D., "X-ray photoelectron spectroscopy studies of thin films of TiN_x having different annealing histories", J. Vac. Sci. Technol. **A 3** (1985) 1969-1972.

234. B.D. Cully, *Elements of X-ray Diffraction,* Addison-Wesley Publishing Company Inc., 1978.

235. Berriche R., Koul A.K., Au P., Immarigeon J.-P., "Evaluation of hard TiN coatings by depth sensing indentation and scratch testing methods", Advanced Performance Materials **4** (1997) 357.

236. Voevodin A.A., Rebholz C., Schneider J.M., Stevenson P., Matthews A., "Wear resistant composite coatings deposited by electron enhanced closed field unbalanced magnetron sputtering", Surf. Coat. Technol. **73** (1995) 185-197.

237. Didziulis S.V., Lince J.R., Stewart T.B., Eklund E.A, "Photoelectron spectroscopic studies of the electronic structure and bonding in TiC and TiN", Inorg. Chem. **33** (1994) 1979-1991.

238. Fuentes G.G., Elizalde E., Sanz J.M., "Optical and electronic properties of TiC_xN_y films", J. Appl. Phys. **90** (2001) 2737-2747.

239. Seung-Hoon Jhi, Ihm J., "Electronic structure and structural stability of TiC_xN_{1-x} alloys", Phys. Rev. **B 56** (1997) 13826-13829.

240. Paxton A.T., van Schilfgaarde M., MacKenzie M., Craven A.J., "The near-edge structure in energy-loss spectroscopy: many-electron and magnetic effects in transition metal nitrides and carbides", J. Phys.: Condens. Matter **12** (2000) 729-750.

241. Mecabih S., Amrane N., Nabi Z., Abbar B., Aourag H., "Description of structural and electronic properties of TiC and ZrC by generalized gradient approximation", Physica **A 285** (2000) 392-396.

242. Jun-Qian Li, Yong-Fan Zhang, Sheng-Chang Xiang, Ying-Nan Chiu, "A density functional study on the electronic structures of TiX (X=C,N,O). I. The electronic structures and bonding properties of TiN bulk and (001) surface", J. Mol. Struct. (Theochem) **530** (2000) 209-216.